Title
Criticality Safety Study for the Disposal of Spent Nuclear Fuel in Water-Saturated Geologic Repository

Author
Liu, Xudong

Publication Date
2016

Peer reviewed|Thesis/dissertation

Criticality Safety Study for the Disposal of Spent Nuclear Fuel in Water-Saturated Geologic Repository

By

Xudong Liu

A dissertation submitted in partial satisfaction of the

requirements for the degree of

Doctor of Philosophy

in

Engineering – Nuclear Engineering

in the

Graduate Division

of the

University of California, Berkeley

Committee in charge:

Professor Joonhong Ahn, Chair
Professor Massimiliano Fratoni
Professor Karl A. van Bibber
Professor Xin Guo

Summer 2016

Abstract

Criticality Safety Study for the Disposal of Spent Nuclear Fuel in Water-Saturated Geologic Repository

by

Xudong Liu

Doctor of Philosophy in Engineering – Nuclear Engineering

University of California, Berkeley

Professor Joonhong Ahn, Chair

Damaged fuels originated from the accident at the Fukushima-Daiichi Nuclear Power Station, and the spent nuclear fuels from commercial light water reactors (LWRs) in Japan are considered to be disposed of in deep geological repository. For a prospective repository, as part of generic performance assessment, a criticality safety assessment (CSA) should be performed to ensure that the repository system including the engineered barriers and host geological formations remains sub-critical for tens of thousands to millions of years. For various repository concepts, CSA is considered to include three major stages in chronological order: (1) the stage before package failure, (2) the stage after package failure, while fissile nuclides remain within the engineered barrier system (EBS) and in the near-field region, and (3) the stage in which fissile nuclides originated from multiple packages are deposited in far-field host rocks. Defining the model for neutronics calculations plays a central role in CSAs, where conservative assumptions are usually made to cope with various uncertainties and to simplify the model. The aim of this dissertation is to develop neutronics models for different stages in the criticality safety study, and provide basic understandings for the long-term criticality safety for the disposal of spent nuclear fuel in geologic repository.

In the near-field analysis, a neutronics model has been developed for a system consisting of a canister containing fuel debris from Fukushima reactors and the surrounding buffer, in a water-saturated deep geological repository. The fuel debris has been modeled as a hexagonal lattice of spherical fuel particles. Following key observations have been concluded from the numerical results: (a) the calculated neutron multiplicity (k_{eff}) is sensitively dependent on assumptions related to moderation, (b) the carbon steel canister plays an important role in reducing the potential for criticality, (c) the maximum k_{eff} of the canister-buffer system could be achieved after a fraction of fissile nuclides been released from the canister, and (d) under several assumptions, the maximum k_{eff} of the canister-buffer system could be principally determined by the dimension and composition of the canister, not by the initial fuel loading. Based on the preliminary results and findings, a parametric study has been made to identify the optimized lattice parameters for criticality. And the critical mass of damaged fuels for a single canister has been

calculated. If this critical mass is used as the maximum canister mass loadings, roughly a thousand canisters are needed to contain the damaged fuels from the three damaged cores. For the LWR spent fuels, a parametric study has been performed to examine spent fuels with different designs and burnup histories. The numerical results indicate that, under the conditions assumed, for all UO_2 spent fuels and most of the MOX spent fuels, the single canister model will always be subcritical.

The far-field study has been focusing on neutronic analysis to examine the criticality conditions for uranium depositions in geological formations which result from geological disposal of damaged fuels from Fukushima reactors. Neutronics models are used to evaluate the k_{eff} and critical mass for various combinations of host rock and geometries. The present study has revealed that the planar fracture geometry applied in the previous criticality safety assessment for geological disposal would not necessarily yield conservative results against the homogeneous uranium deposition. It has been found that various far-field critical configurations are conceivable for given conditions of materials and geological formations. Prior to knowing the site location, some important points for selecting a site for criticality safety can be suggested. These include: (a) iron existing in the host rock reduces the likelihood of criticality significantly; (b) low host rock porosity is preferred for criticality safety; (c) the conservatism could change when comparing heterogeneous geometries for different fracture apertures; and (d) the importance of the mass of the deposition increases when it is smaller.

As part of the improvement for the models developed in the far-field analysis, preliminary works on uranium depositions in randomly fractured rocks have been presented. The randomly fractured geometry could fundamentally influence the far-field criticality, because the system's k_{eff} value sensitively depends on the fracture aperture and the depositions at fracture intersections. No previous work has been made to study the effect of random geometry in the context of the long-term criticality safety in a geologic repository. Different numerical schemes have been developed and compared for the direct sampling of uranium depositions in randomly fractured rocks using MCNP. A general literature review of existing methods for neutron transport problems with random processes has been made. And the analytical Feinberg-Galanin-Horning (FGH) method has been derived and tested for a numerical example.

Table of Content

List of Figures

List of Tables

Acknowledgement

I would like to express my greatest gratitude to my faculty advisor and dissertation committee chair, Prof. Joonhong Ahn, for his inspiring mentorship in the past five years. This dissertation would not have been possible without his guidance and encouragement. Thanks also to my committee members, Prof. Massimiliano Fratoni, Prof. Karl A. van Bibber, and Prof. Xin Guo, who provided thoughtful questions and suggestions.

I would like to thank all of the graduate students and visiting scholars in the waste management group. The fruitful discussions we shared are truly mind-opening. I would like to express my gratitude to Dr. Fumio Hirano from Japan Atomic Energy Agency, for the careful review of the annual reports.

Thanks to all my friends in Berkeley for the times we enjoyed together. Particularly, to Lei Li, Di Yang, and David Zhu, who helped and encouraged me through difficulties.

I am deeply indebted to my parents, who made extraordinary effort in providing me a chance to pursue higher educations. And finally, special thanks to my wife, Naixi Feng, who has always been supporting me with love and patience.

Chapter 1 Introductions

1.1 Introductions

The accident at the Fukushima-Daiichi Nuclear Power Station in March 2011[1] generated damaged fuel in three crippled reactors, containing nearly 250 metric tons of uranium and plutonium along with fission products, minor actinides, and other materials such as fuel cladding, assemblies, and in-core structural materials. While exact forms and conditions of such damaged fuels are yet to be thoroughly investigated[2], they will be eventually disposed of in a deep geological repository. The spent nuclear fuels from commercial light water reactors in Japan are currently considered in its national policy[3] to be disposed of in the form of vitrified high-level wastes after reprocessing, but after the Fukushima accident, active public discussions exploring alternative nuclear fuel cycles started, in which feasibility study[4] for direct disposal of spent nuclear fuel in a deep geological repository was started by Japan Atomic Energy Agency.

For a prospective repository containing the damaged fuels and spent fuels aforementioned, as part of generic performance assessment, a criticality safety assessment (CSA) should be performed to ensure that the repository system including the engineered barriers and host geological formations remains sub-critical for tens of thousands to millions of years.

For various repository concepts[5], [6], CSA is considered to include three major stages in a chronological order: (1) the stage before package failure, (2) the stage after package failure, while fissile nuclides remain within the engineered barrier system (EBS) and in the near-field region, and (3) the stage in which fissile nuclides originated from multiple packages deposit in far-field host rocks.

For the criticality safety study for stages (1) and (2), a consistent methodology needs to be developed to evaluate the criticality safety performance for a given EBS design, so that the possibility of a criticality event to occur in the near-field could be minimized or eliminated. The neutronics model for the near-field analysis should take into account the changes in geometry due to the degradation and alteration of EBS, including metal canisters, spent fuel assemblies, fuel pins, and buffer materials, and the release and redistribution of fissile nuclides in the system. Study on stages (1) and (2) are referred to as the near-field analysis in later chapters.

In stage (3), the dissolved fissile nuclides from multiple canisters will eventually be transported and deposit in host rocks in the far-field. Assuming that the fissile nuclide deposition locates outside the near-field region, we need to study the critical masses of the fissile depositions (originated from different spent fuels) in various geological formations. After identifying in which conditions critical configurations can be formed in assumed host rock conditions, nuclide transport analysis needs to be performed to determine whether formation of such critical mass deposit could actually be achieved. Study on stage (3) is referred to as the far-field analysis in later chapters.

Although criticality accidents should be prevented by the repository design, consequences of criticality events in a geological repository based on hypothetical configurations have been evaluated by previous studies, such as ref. [7]. Depending on

the reactivity feedback mechanisms, the amount of radioactivity generated from the chain reactions and the dose released to the bio-sphere can be evaluated.

1.2 Literature Survey

Defining the model for neutronics calculations plays a central role in CSAs, where conservative assumptions are usually made to cope with various uncertainties and to simplify the model. To define the present work, neutronic models developed in previous studies for various stages in the CSAs are firstly reviewed, with special focus on their assumptions for the model geometry.

For the near-field analysis, the earliest effort made to model the degraded fuel assembly was the criticality simulations carried out in the defueling completion report[8] after the Three Mile Island accident. To avoid criticality accidents when handling fuel debris, Safe Fuel Mass Limit (SFML) was conservatively defined as the critical mass of a water-reflected spherical system filled with fuel particles in a hexagonal closed packed (HCP) lattice and moderated by water. The pitch distance between fuels particles is chosen to optimize the moderation by maximizing the infinite neutron multiplicity (k_{inf}). Only the depletion of fissile nuclides was taken into account as burnup credit, and no neutron poisons from fission products or structural materials were included. The radius of the spherical fuel particle was calculated to give the same volume of a fuel pellet. In a CSA for spent fuel storage casks[9], various cases of failures for fuel assemblies and fuel pins are constructed and compared. Among all the cases considered, the highest increase in k_{eff} was observed when the storage cask was assumed to be filled with fuel particle lattice and water, or called "Uniform pellet array" by the report. This array configuration of fuel pellets is actually the same as was assumed in the SFML model. In the criticality safety study for United Kingdom's High Level Waste (HLW) disposal project[6], the criticality simulations were coupled with canister corrosion and nuclide release models. After water intrusion, the fissile nuclides are assumed to be either fully separated or homogeneously mixed with water. The model geometry has been assumed differently for vertical or horizontal canister emplacement. The k_{eff} of the canister is significantly decreased when the corroded carbon-steel canister is mixed with fissile materials, which indicates the neutron absorbing materials in the disposal canister, such as iron in carbon steel, could significantly enhance the long-term criticality safety after final disposal.

For the far-field analysis, in previous studies, various neutronics models were developed to represent the repository geological conditions by considering compositions of fissile depositions, groundwater, rocks, and geometries. Fissile depositions in Nevada tuff rock have been studied[10]–[16] for the Yucca Mountain Repository (YMR). In the analysis of rock salt repositories[17], chlorine concentration was considered. In the previous studies for repository criticality safety such as ref. [10]–[15], [18], the planar fracture model was used for representing heterogeneity of TFM deposition in geological formations. Compared with homogeneous systems, it was observed that in heterogeneous geometries, neutron transport and multiplication mechanisms are significantly different from homogeneous systems. However, the conservativeness of the planar fracture model has never been investigated in detail.

1.3 Scope of this Dissertation

The aim of this dissertation is to develop neutronics models for different stages in the criticality safety study and to provide basic understandings of the long-term criticality safety for the disposal of spent nuclear fuel in geologic repository.

The dissertation consists of three parts. In the first part, namely the near-field study, methodology development and parametric study has been performed to study the criticality safety in the vicinity of a single waste-canister and surrounding engineering barriers. The model has been applied for damaged fuels Fukushima reactors[19], [20] and various spent fuels from light water reactors (LWRs)[20]. A parametric study has been performed for the damaged fuel particles in the infinite HCP lattice for three damaged cores at five different time points to determine the mass limit for canister design[21]. The model was also applied[22] to calculate LWR spent fuels with different initial enrichments, burnups, reactor types, and fuel types.

The far-field study has been focusing on neutronic analysis to examine the criticality conditions[23] for uranium depositions in geological formations which result from geological disposal of damaged fuels from Fukushima Daiichi reactors. Neutronics models are used to evaluate the neutron multiplication factor (k_{eff}) and critical masses for various combinations of host rock and geometries. The conservativeness of the planar fracture model has been investigated. Prior to knowing the site location, some important points for selecting a site for criticality safety are suggested.

As part of the improvement for the models developed for the far-field analysis, preliminary works on uranium depositions in randomly fractured rocks have been presented. The randomly fractured geometry could fundamentally influence the far-field criticality, because the system's k_{eff} value sensitively depends on the fracture aperture and the depositions at fracture intersections. No previous work has been made to study the effect of random geometry in the context of the long-term criticality safety in a geologic repository. Different numerical schemes have been developed and compared for the direct sampling of uranium depositions in randomly fractured rocks using MCNP[24]. A general literature review of existing methods for neutron transport problems with random processes has been made. And the Feinberg-Galanin-Horning (FGH) method[25] has been derived and tested for a simple numerical example.

Although the numerical results are only calculated for limited cases, the generic findings in the dissertation can be utilized in determining site-selection criteria and in improving designs of EBS and burnup schemes.

Chapter 2 Near-Field Analysis: Criticality in the Vicinity of Waste-Canister and Engineering Barriers

2.1 Introductions

This chapter focuses on model development and numerical results for the near-field analysis. As has been defined in section 1.1, the major concerns in the near-field analysis include two stages; they are (1) the stage before package failure, and (2) the stage after package failure, while fissile nuclides remain within the engineered barrier system (EBS) and in the near-field region. Methodology development and a parametric study for the two stages are presented in this chapter. The criticality safety in the vicinity of a single waste-canister and surrounding engineering barriers have been studied for damaged fuels Fukushima reactors and various spent fuels from light water reactors (LWRs).

For the damaged fuels from Fukushima reactors, Section 2.2 has focused on neutronics analysis for a system consisting of a canister containing fuel debris from Fukushima Unit 1 reactor and the surrounding buffer, in a water-saturated deep geological repository[19]. Based on the literature review[8] in Section 1.2, the fuel debris has been modeled as a hexagonal lattice of spherical fuel particles. The model developed in Section 2.2 has been applied in Section 2.3, to determine the mass limit for canister design. Based on the findings in the previous section, a parametric study has been performed for the damaged fuel particles in the infinite HCP lattice for three damaged cores at five different time points. Optimized lattice parameters for criticality have been identified and qualitatively explained.

For LWR spent fuels, because the canister designs commonly require the canister being sub-critical in both dry and water filled conditions, the primary concern for the criticality safety is the time period after all assembly structures and claddings fail, until the bare fuel pellets in the canister have completely dissolved. The conditions of the failed spent fuel assemblies during this time period could not be known exactly. In addition, spent fuels with different designs and burnup histories may behave differently. To address these concerns, the analysis for LWR spent fuels (Section 2.4) includes two primary tasks. The first task is to explore under what conditions the neutron multiplicity of a spent fuel canister can be maximized, so that the uncertainty of the result can be bounded. The second task is to perform a parametric study to examine spent fuels with different designs and burnup histories. A neutronic model for a system consisting of a canister containing PWR/BWR spent fuel assemblies and the surrounding buffer has been firstly introduced. The model is applied to calculate to spent fuels with different initial enrichments, burnups, reactor types (BWR/PWR), and fuel types (UO_2/MOX), in Section 2.3 based on the burnup results from[22].

2.2 Model Development and Preliminary Analysis for a Canister Containing Damaged Fuels in the Near-Field

2.2.1 Background and Assumptions

The repository is assumed to be in a water-saturated reducing environment. The neutronics model consists of a canister containing fuel debris from Fukushima reactors and the buffer material surrounding the canister. Because no design has been officially recommended for the disposal system for the damaged fuels, the composition and dimension of the canister and buffer are assumed to be based on the design for spent fuel disposal being developed by JAEA[4]. Because the canister for disposal of damaged fuels might not need to fit the length of an intact fuel assembly, the canister inner height is arbitrarily assumed as 1 meter, and all other parameter values are assumed to be identical to the values in ref. [4]. The present work considers six nominal time points for neutronics analysis: the emplacement time (t=0), the canister failure time ($t=T_f$), and four time points during the dissolution of debris particles ($t=T_f+0.2T_l$, $t=T_f+0.4T_l$, $t= T_f+0.6Tl$ and $t= T_f+0.8T_l$). The failure time (T_f) of the carbon steel canister is assumed to be 1000 years. After canister failure, water fills inside the canister, and the canister itself is modeled as a porous medium with porosity of 0.3.

The damaged fuel is assumed to be disposed of after 50 years of cooling from the time of the accident. The fuel composition after the accident was calculated by burnup code ORIGEN[26], based on results reported in ref. [1]. Source term preparations are discussed in section 2.2.1. The fuel is assumed to be released from the canister at a constant rate during the leach time (T_l). The fission products are assumed to be released congruently with the damaged fuel dissolution, which is conservative (i.e., overestimation of mass loss of neutron absorbers from the canister) because the canister would contain more neutron poison, if the release is limited by solubility. The time scale of the leaching of the damaged fuels (mainly UO_2) in a reducing environment is assumed to be of the order of multi-million years, which is much longer than the half-lives of Pu-239 (24100 years) and Pu-240 (6560 years), and much shorter than the half-lives of U-235 (704 million years) and U-238 (4.5 billion years). Therefore, after a fraction of leach time, almost all Pu-239 and Pu-240 decays to U-235 and U-236. For this reason, we assume that the composition of the damaged fuel at the four time points remains the same as that of the damaged fuels after 200,000 years. The neutronics analysis is hence decoupled from the actual leach time, as long as the assumptions for the time scale are valid.

The geometry of neutronics model at different time points has been built based on our literature review and is discussed in details in the next section. The hexagonal lattice of spherical fuel particles is assumed. The assumption for the fuel particles radius was adopted from the TMI defueling report[8]. According to the TMI defueling report[8], (a) decreasing the radius while keeping the same total fuel mass will decrease the k_{eff}, and (b) larger particles from re-solidified fuels contain significant amount of structural materials and have much lower reactivity. Therefore, the diameters of the spherical fuel particles are assumed to give the same volume of a fuel pellet. More discussions on the particle diameters are given in Section 2.3.

The pitch distance between particles is assumed to be either (1) make particles contact each other or (2) make the particles lattice fully fill the canister. During the leaching time, the released materials from the damaged fuel particles is assumed to be either (a) removed from the canister-buffer system, or (b) be homogeneously mixed with the corroded canister. Combinations of the above variations make four cases: case 1a, case 1b, case 2a, and case 2b. For simplicity, in later discussions, we use phrase "case (1)" to represent both case 1a and case 1b, "case (2)" to represent case 2a and case 2b, "case (a)" to represent case 1a and case 2a, and "case (b)" to represent case 1b and case 2b.

2.2.2 Source Term Preparations

The composition of the damaged fuels at the time of the accident was calculated by the burnup code ORIGEN[26]. Neutron absorbing nuclides generated by fission and activation could co-exist with the damaged fuels after the final disposal. They decay together with other nuclides included in the waste canister, and relocate after canister failure and ground water intrusion. The neutron absorbers reduce the system's k_{eff}, resulting in reduction in the possibility of criticality.

This section aims at recognizing important neutron absorbing elements in fission products and activated materials, based on their yield and microscopic neutron absorption cross sections. These first-round screening is basically done from neutronics point of view, and we need further screen out gaseous and volatile elements and finally determine which element remains within the damaged fuels.

Only for the purpose of comparing the relative importance of different elements, a simple estimation can be made by assuming all neutron absorbing elements in the fission products and activated materials from three damaged cores is homogeneously lumped into volume of V [m^3]. Considering that some of the neutron absorbers are short-lived, we first arbitrarily assume 50 years as a decay time for a crude estimation. Due to radioactive decay, the neutron absorption in the damaged fuels is changing with time. For the analysis after disposal, 50 year is assumed as cooling time. We denote the element species by E and isotopic species for element E by i. For example, $M^{E,i}$ [g] is defined as the total mass of isotope I of element E from three damaged cores, which can be calculated by ORIGEN and we use the data given by ref. [1].

The macroscopic thermal neutron absorption cross section, $\Sigma_{th,a}^{E}$ [cm^{-1}], for element E can be given by the following equation.

$$\Sigma_{th,a}^{E} = \sum_{i} \frac{M^{E,i}}{\mu^{E,i} \times V} \times \sigma_{th,a}^{E,i} \times N_A \times 10^{-24} \left[cm^2 / \text{barn} \right] \times 10^{-6} \left[m^3 / cm^3 \right] \qquad (2\text{-}1)$$

Where $\mu^{E,i}$ [g/mol] is the atomic mass of nuclide (E,i), $N_A = 6.022 \times 10^{23} \left[mol^{-1} \right]$ is the Avogadro constant, and $\sigma_{th,a}^{E,i}$ [barn] is the microscopic thermal neutron absorption cross section of nuclide (E,i), tabulated in ref. [27]. Multiplying equation(2-1) by volume V, we have,

$$\Sigma_{th,a}^{E} \times V = \sum_{i} \frac{M^{E,i}}{\mu^{E,i}} \times \sigma_{th,a}^{E,i} \times N_A \times 10^{-24} \left[cm^2 / \text{barn} \right] \times 10^{-6} \left[m^3 / cm^3 \right]. \qquad (2\text{-}2)$$

The right-hand side of equation(2-2) is determined by nuclide properties (i.e. $\mu^{E,i}$ and $\sigma_{th,a}^{E,i}$), and the composition of the damaged fuels (i.e. $M^{E,i}$). Therefore, we can compare the relative importance for different elements as neutron absorber by the value of $\Sigma_{th,a}^{E} \times V$. For each element, this term is proportional to its macroscopic thermal neutron absorption cross section $\Sigma_{th,a}^{E}$ by the same factor 1/V. After 50 years decay, there are 47 elements in the activation and fission product group with total mass greater than 1 gram in three cores, the calculated result for $\Sigma_{th,a}^{E} \times V$ are tabulated in Table 2-1.

Table 2-1: Important neutron absorbing elements in activated materials and fission products.

#	Element	$\Sigma_a^E \times V \left[cm^{-1} \times m^3 \right]$	#	Element	$\Sigma_a^E \times V \left[cm^{-1} \times m^3 \right]$
1	Gd	3.07E-01	25	Ba	6.80E-04
2	Nd	2.42E-01	26	In	3.57E-04
3	Sm	1.60E-01	27	Dy	2.22E-04
4	Rh	7.12E-02	28	I	2.14E-04
5	Zr*	6.75E-02	29	Rb	1.43E-04
6	Eu	5.44E-02	30	Te	1.25E-04
7	Xe	3.31E-02	31	Se	8.15E-05
8	Cs	2.92E-02	32	Br	6.84E-05
9	Tc	1.77E-02	33	Sb	4.90E-05
10	Mo	1.50E-02	34	Tb	3.17E-05
11	Kr	1.23E-02	35	Mn	5.16E-06
12	Pr	1.00E-02	36	V	3.76E-06
13	La	8.68E-03	37	Sr	3.64E-06
14	Pd	8.63E-03	38	Ho	3.39E-06
15	Ag	6.82E-03	39	Co	2.01E-06
16	Ru	4.50E-03	40	As	1.23E-06
17	Fe	3.86E-03	41	Ge	5.86E-07
18	Cd	3.24E-03	42	Cu	3.73E-07
19	Sn	2.18E-03	43	Er	2.50E-07
20	Cr	1.88E-03	44	H	2.46E-07
21	Ce	1.44E-03	45	C	9.75E-08
22	Ni	1.20E-03	46	Nb	2.51E-08
23	Y	7.70E-04	47	He	0
24	O*	6.89E-04			

The sum of all the 47 elements gives $1.07 \left[cm^{-1} \times m^3 \right]$, the groups of the “top 10” elements contribute to 93.6% of the total and the “top 20” makes about 99.4% of the total

absorption cross section. This observation indicates that, even if we only consider a few most important elements, they cover more than 90% of the neutron absorptions from fission products and activated materials.

From Table 2-1, we can easily recognize the most important neutron absorbers such as gadolinium, neodymium, samarium, and rhodium. And a large fraction of elements in the table are lanthanides. Zirconium is not a strong neutron absorber but because of its large quantity in the cladding, it still is ranked at number 5 in the table.

The elements in Table 2-1 need to be further considered to determine whether or not it could remain within the damaged fuels after the accident []. Only Insoluble and non-volatile elements can be considered. We include the top five elements after screening, including Gd, Nd, Sm, Rh, and Eu isotopes. Zirconium is not counted because it is the cladding material and might not be fully included in the damaged fuel debris. We have further examined the half-lives of these nuclides and found out that they are all stable. Therefore, these neutron poisons could be included in the damaged fuels until they have leached from the canister. The compositions 0, 1000, 10000, 100000, and 200000 years after the emplacement (assuming 50 years cooling before emplacement) have been calculated using ORIGEN[26] code. All actinide isotopes have been included. The actinides and fission product composition for the damaged fuels from Fukushima Unit 1 after different decay times from the accident is shown in Table 2-2. These results are used the near-field in calculations in this section and Section 2.3.

Table 2-2: Composition of damaged fuels from Fukushima-Daiichi Unit 1 reactor.

	Amount of nuclides (mole) for different decay times from the accident (values cut-off at one mole)				
Nuclide	50 (yr)	1050 (yr)	10050 (yr)	100050 (yr)	200050 (yr)
Rh-103	2.39E+02	2.39E+02	2.39E+02	2.39E+02	2.39E+02
Nd-143	3.20E+02	3.20E+02	3.20E+02	3.20E+02	3.20E+02
Nd-145	2.59E+02	2.59E+02	2.59E+02	2.59E+02	2.59E+02
Sm-147	1.11E+02	1.11E+02	1.11E+02	1.11E+02	1.11E+02
Sm-149	1.13E+00	1.13E+00	1.13E+00	1.13E+00	1.13E+00
Sm-150	9.57E+01	9.57E+01	9.57E+01	9.57E+01	9.57E+01
Sm-152	3.95E+01	3.95E+01	3.95E+01	3.95E+01	3.95E+01
Eu-151	1.51E+00	4.63E+00	4.63E+00	4.63E+00	4.63E+00
Eu-153	3.84E+01	3.84E+01	3.84E+01	3.84E+01	3.84E+01
Gd-155	2.31E+00	2.32E+00	2.32E+00	2.32E+00	2.32E+00
U-233			1.06E+00	8.94E+00	1.44E+01
U-234	1.19E+01	3.49E+01	3.44E+01	3.00E+01	2.63E+01
U-235	4.73E+03	4.76E+03	5.05E+03	5.95E+03	6.02E+03
U-236	1.03E+03	1.07E+03	1.31E+03	1.46E+03	1.46E+03
U-238	2.74E+05	2.74E+05	2.74E+05	2.74E+05	2.74E+05
Np-237	9.84E+01	2.97E+02	3.46E+02	3.36E+02	3.25E+02
Pu-238	2.28E+01				
Pu-239	1.29E+03	1.25E+03	9.71E+02	7.33E+01	4.11E+00
Pu-240	4.39E+02	3.95E+02	1.52E+02		
Pu-241	2.19E+01				
Pu-242	8.33E+01	8.32E+01	8.19E+01	6.97E+01	5.83E+01
Am-241	2.26E+02	5.01E+01			
Am-243	1.40E+01	1.28E+01	5.48E+00		

2.2.3 Model Development

The schematic layout of the neutronics model is shown in Figure 2-1. The canister-buffer system has been determined mainly based on the design from ref. [4], which consists of a carbon-steel[28] canister (inner radius r, inner height h and thickness θ_1 surrounded by buffer [29] (70% Kunigel V1 Bentonite + 15% Silica sand No. 3 + 15% Silica Sand No. 5, thickness θ_2). The canister is assumed to be emplaced vertically and is filled with spherical fuel particles (diameter D) in a hexagonal lattice (with pitch distance P), up to height H. The unit cell of the lattice is shown in the right bottom of Figure 2-1.The dimensions and compositions of the canister and buffer are shown in Table 2-3 and Table 2-4. The inner height of the canister is assumed to be 100cm.

The fraction of volume taken by the fuel lattice f for a hexagonal lattice with pitch distance D and fuel radius R can be written as[30],

$$f = \frac{\pi}{3\sqrt{2}}\left(\frac{D}{P}\right)^3, P \geq D. \quad (2\text{-}3)$$

The canister is initially contains M_0 [kg] of damaged fuel. After canister failure, the mass of remaining damaged fuel in the canister $M(t)$ can be written as,

$$M(t) = M_0\left(1 - \frac{t - T_f}{T_l}\right), T_f \geq t \geq T_f + T_l. \quad (2\text{-}4)$$

From the mass balance in a canister with inner radius r and height H filled by fuel lattice, the following formula can be written:

$$M(t) = \pi r^2 H(t) f \rho, T_f \geq t \geq T_f + T_l, \quad (2\text{-}5)$$

where ρ is the density of the damaged fuel, assumed to be the density of UO_2. Note that the height of the lattice is a function of time. By substituting (2-3) and (2-4) in equation(2-6), the relation between H, D, and t can be given as

$$\frac{\pi^2}{3\sqrt{2}} r^2 H(t)\left(\frac{D}{P(t)}\right)^3 \rho = M_0\left(1 - \frac{t - T_f}{T_L}\right), T_f \geq t \geq T_f + T_l \quad (2\text{-}6)$$

Note that the pitch distance D of the lattice is also dependent on time.

In order to determine P and H for a given time t, further assumptions are needed. Among four cases defined in the last paragraph of Section 2.2.1, the pitch distance P can either make particles contact each other (in cases 1a and 1b), which means P(t)=D=constant, or make the particles lattice fully fill the canister (in cases 2a and 2b) which means H(t)=h=constant. With this applied, for case 1a and case 1b, equation(2-6) can be modified as

$$H(t) = M_0\left(1 - \frac{t - T_f}{T_L}\right) / \left(\rho \frac{\pi^2}{3\sqrt{2}} r^2\right), T_f \geq t \geq T_f + T_l \quad (2\text{-}7)$$

And for case2a and case2b, equation (2-6) can be written as,

$$P(t) = \left\{ \frac{\pi^2}{3\sqrt{2}} r^2 h \frac{\rho D^3}{\left[M_0\left(1 - \frac{t - T_f}{T_L}\right)\right]} \right\}^{\frac{1}{3}}, T_f \geq t \geq T_f + T_l. \quad (2\text{-}8)$$

The difference between case 1a and case 1b or case 2a and case 2b is that, in case (a) the released fuel is assumed to be removed from the system, while in the case (b) the released fuel is assumed to be homogeneously mixed with the corroded canister, which has a porosity of 0.3. By definition, there is no difference between case (a) and case (b) in t=0 and t= T_f.

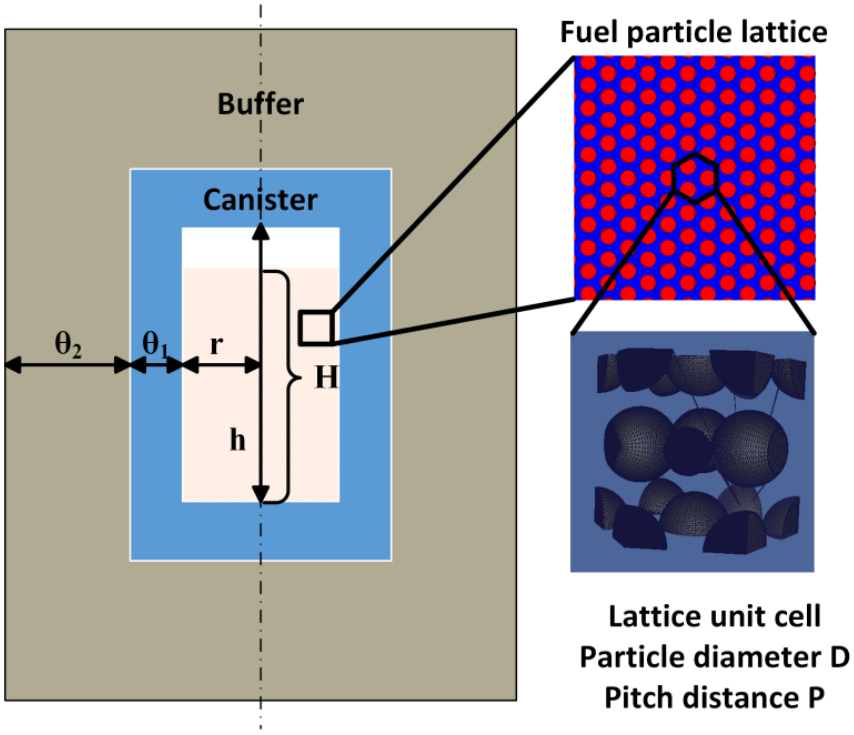

Figure 2-1: Schematic layout of the canister-buffer system and hexagonal close packed (HCP) fuel particle lattice.

Table 2-3: System dimensions of the canister-buffer model.

System dimension	Values
Canister inner radius r [cm]	27.95
Canister inner height h [cm]	100.00
Canister thickness θ_1 [cm]	14.00
Buffer thickness θ_2 [cm]	70.00
Fuel particle diameter D [cm]	1.11

The fuel particle diameter has been assumed to give same volume of a fuel pellet, for reasons reported in ref. [8]. Because the damaged fuels[1] are mainly STEP-III[31] type, the equivalent fuel particle diameter has been calculated based on the pellet diameter of STEP-III fuel. The pellet diameter of STEP-III fuel is 9.6 mm[31], and the pellet height is assumed to be 10 mm. By solving $\frac{1}{6}\pi D^3 = \frac{1}{4}\pi \times (9.6)^2 \times 10 \left[mm^3 \right]$, the diameter can be calculated as D=1.11 cm.

Table 2-4: Canister and buffer compositions.

Canister composition: Carbon steel[28]	Weight fraction [%]
Fe	99.5
C	0.5
Density [g/cm^3]	7.82
Buffer composition[29]: 70% Bentonite + 30% Silica sand	Weight fraction [%]
SiO_2	78.157
TiO_2	0.138
Al_2O_3	11.033
Fe_2O_3	1.368
MgO	1.449
CaO	1.533
Na_2O	1.429
K_2O	0.358
MnO	0.035
P_2O_3	0.021
SO_3	0.448
H_2O	4.033
Dry density [g/cm^3]	1.60
Porosity	0.38

The diameter of the fuel particle is calculated to match the volume of a fuel pellet. And is fixed at a constant value through analysis in this section, the influence of the lattice parameters is discussed in Section 2.3. With the fuel composition, the dimension of the canister-buffer system, and the fuel lattice parameters calculated by equation(2-7) or (2-8), MCNP criticality calculations have been made for the four cases with initial loadings of 500kg, 1000kg, and 1500kg. Six nominal time steps are considered, at t=0 (emplacement time, 50 years from the accident), the canister is filled with fuel particles (no water is included) defined by the second column of Table 2-2. The canister material has zero porosity initially. At the canister failure time T_f, the canister suddenly becomes porous with 30% porosity, and water fills inside the canister. The fuel composition after 1050 year decay was shown in the third column of Table 2-2. At the subsequent four leaching steps, composition after 200050 years decay (the sixth column of Table 2-2) is used. In addition, the hypothetical cases in which the canister is filled with water at time zero were also calculated.

2.2.4 Numerical Results

The numerical results for initial loadings of 500kg, 1000kg, and 1500kg are shown in Figure 2-2, Figure 2-3, and Figure 2-4, respectively. The neutron multiplication factor k_{eff} is plotted against the nominal time steps for various combinations of cases and initial loadings. Note that the time axis only represents the order of the time points and does not represent the actual time. The failure time (1000 years) should be several orders

of magnitude smaller than the leach time. In Figure 2-2, Figure 2-3, and Figure 2-4, the solid points represent case (1), or cases assuming that fuel particles are in close contact each other, whereas the hollow points represent case (2), or cases assuming that the fuel lattice fills the canister. Red points represent case (a), assuming all fissile nuclide released from the canister are removed from the system, and blue points represent case (b), assuming released nuclides are homogeneously mixed with the corroded canister. The green points in three figures in Figure 2-2, Figure 2-3, and Figure 2-4 represent cases assuming the canister is filled with water at time zero.

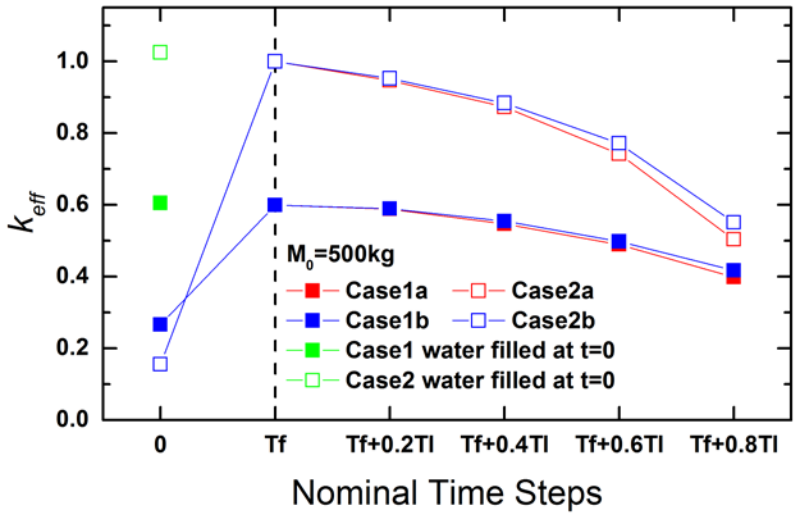

Figure 2-2: Calculated k_{eff} for various cases versus nominal time steps for initial loading of 500kg.

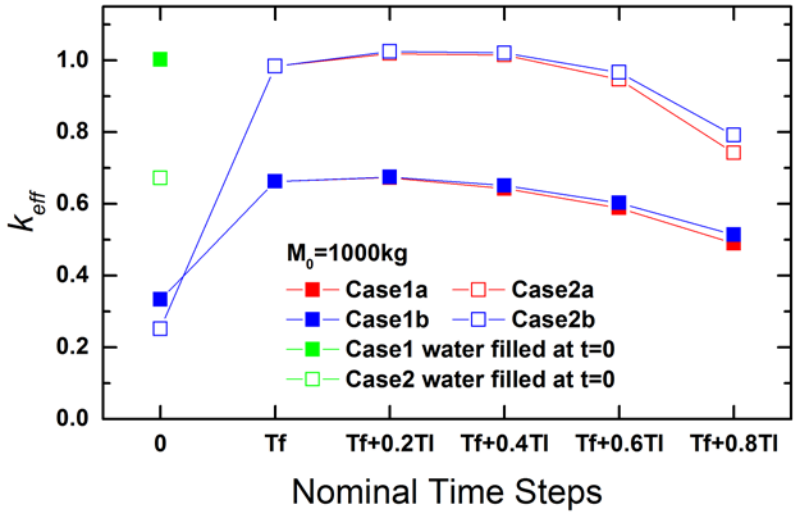

Figure 2-3: Calculated k_{eff} for various cases versus nominal time steps for initial loading of 1000kg.

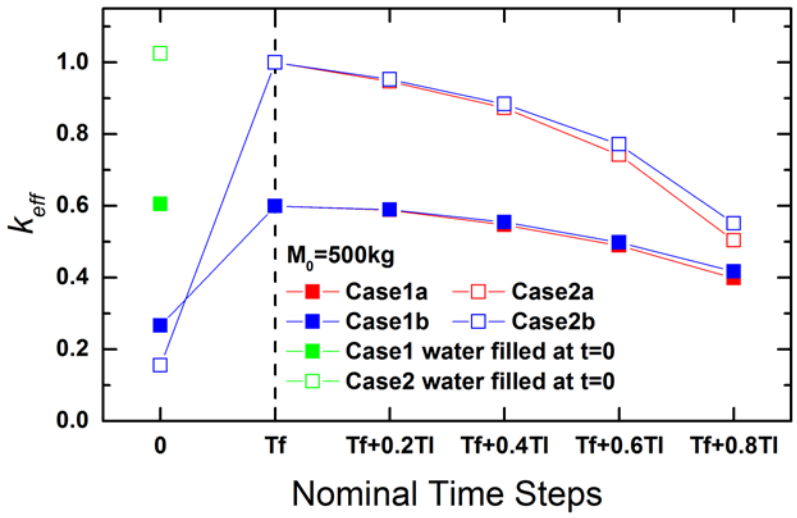

Figure 2-4: Calculated k_{eff} for various cases versus nominal time steps for initial loading of 1500kg.

At time zero, if the canister is filled with water, the k_{eff} is significantly greater than the no water cases, because the reactivity is greatly increased by introducing moderation from water. For the same reason, there is a significant increase in k_{eff} observed in all cases from time zero to canister failure time, when water is assumed to fill the void spaces in the system.

After $t=T_f$, the damaged fuels in the canister start to dissolve and be released from the canister. Also between $t= T_f$ and $t= T_f + 0.2T_l$, most of the plutonium isotopes decay into uranium isotopes. In the following time steps, the isotopic composition of the damaged fuels is assumed to remain the same, while the mass in the canister is decreased. However, only with the 500kg initial loading (Figure 2-2), decrease in k_{eff} with time for all cases is observed. In case 2a, case 2b for 1000kg and 1500kg initial loadings, respectively, the k_{eff} once increases, and then decreases, as an increasing fraction of the fuel is released from the canister. This observation is discussed and explained in Section 2.2.5.2. In addition, the maximum k_{eff} values for M_0=1000kg and M_0=1500kg are nearly equal to each other, which indicates that if the canister and buffer are in the same configurations, which are designed to realize sub-critical right after disposal, the initial loading might not be a sensitive factor to determine the magnitude of k_{eff} of the system.

Comparing cases (1) (solid points) and (2) (hollow points), in all time steps with water in canister, case (2) gives much higher k_{eff} than case (1). Case (2), in which fuel particles are assumed to "float" in the canister might be considered unphysical but more conservative. This result is consistent with our findings in the literature survey.

Another important finding is that, after a fraction of damaged fuels is released, by mixing all the released fissile nuclide with the corroded porous carbon-steel canister, case (b) results are only slightly higher than results from case (a), and be very different from the canister at T_f, which have the same amount of total fissile material. This result shows

that, within the assumed conditions, although the fissile materials released from the canister are assumed to be conservatively retained within the canister-buffer system, the influence on criticality can be very small.

2.2.5 Discussions

2.2.5.1 Influence of Leakage and Moderation

Generally speaking, nuclear criticality is influenced by neutron leakage and moderation[32]. Among the parameters defined in the present work, neutron leakage is related with the mass of fuels in the canister M(t). The greater mass in canister, the lower the neutron leakage, and the higher the k_{eff}. The moderation, or neutron slowing down, is determined by the amount of water relative to the amount of the fuel in the system, and can be represented by the P/D ratio. With fuel particle diameter D assumed constant, the larger pitch distance P, the more neutrons are moderated or thermalized.

The dependence of criticality on moderation can be understood by calculating the neutron multiplication factor k_{inf} of infinite fuel particle lattice for different pitch distance D. The results for damaged fuels after different decay time are plotted in Figure 2-5. Note that the pitch distance must be greater than or equal to the diameter of the fuel particle (in the present work D=1.11). Both curves shows drastic changes in k_{inf} as a function of P; the maximum is found at around P=1.5 cm, and the minimum (within the range of calculations) is found at D=1.11 cm. The system is called under-moderated or over-moderated when P is lower or higher than the value for maximum k_{inf} respectively. By definition, case (1) assumes fuel particles are closely packed, in which P=1.11 remains constant at its minimum for different time steps. While in case (2), according to equation(2-8) , the pitch distance is increased as time increases, and is decreased with greater initial loading M_0, but be always higher than 1.11 cm.

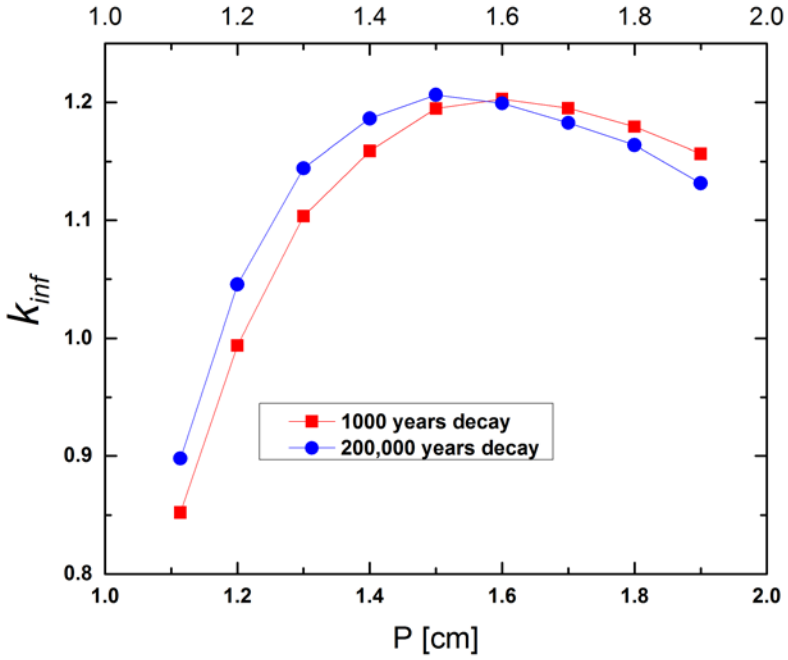

Figure 2-5: Neutron multiplicity of infinite HCP lattice for different pitch distances.

As a result, case (2) always gives higher k_{eff} than case (1). For case (2), the initial loading which gives P(t=0)=1.5 can be calculated from equation(2-8) as M_0^*=817 kg. If M_0 is smaller than M_0^*, P(t=0) will be greater than 1.5, and the system started under-moderation will be even further under-moderated as time increases. However, if M_0 is greater than M_0^*, the system will reach its optimized moderation after a fraction of the fissile nuclide has been released. This explained the observations for case (2) results when M_0=1000 kg and 1500 kg.

2.2.5.2 Role of the Carbon-Steel Canister

The canister considered in the present work is made of 14 cm thick carbon steel. The thickness of the canister was primarily determined to delay sufficiently the failure from corrosion, so that at least the major heat-emitting radionuclides, Cs-137 and Sr-90, in the waste canisters decay out. Our numerical results indicate that the neutron-absorbing corroded canister could profoundly enhance the criticality safety. For all initial loadings after canister failure time in Figure 2-2, Figure 2-3, and Figure 2-4, case (a) and case (b) show very close results, which means mixing the fissile nuclide with the corroded canister is almost equivalent to removing those nuclides from the system. A fundamental reason for this result is that the minimum critical mass of a homogeneous mixture between the damaged fuel and corroded canisters or buffer is much higher than the minimum critical mass of the fuel particle lattice (see Section 2.3). More discussions on critical mass for a homogeneous mixture of rock and fissile nuclides are presented in

Chapter 3. Therefore, as long as a fraction of the damaged fuels remains, the neutronics property of system is principally determined by the materials inside the canister.

Coming back to the three stages introduced in Section 1.1 in CSA: (1) the stage before package failure, (2) the stage after package failure, while fissile nuclides remain within the engineered barriers, and (3) the stage in which fissile nuclides originated from multiple packages deposit in far-field host rocks. The boundary between stages (2) and (3) was not well defined. There are conceivable scenarios when fissile nuclides from multiple canisters form a deposition near the canisters while there are fissile nuclides remaining in one or more of these canisters. Naturally, the situation can be much more simplified if the deposition and individual canisters can be decoupled and modeled separately. Whether or not this can be achieved certainly depends on the design of the disposal system. Although further confirmation by numerical results is necessary, the neutron absorbing canister seems to play an important role to decouple the domains inside and outside the canister from CSA.

2.2.5.3 Criticality Constrains for Canister Design

The engineered barrier, including canister and buffer, needs to be designed to minimize or eliminate, if possible, the potential of criticality over hundreds of thousands of years. Sub-criticality with certain safety margin assuming water flooded configuration with geometry fixed at initial condition is the one which is the most commonly used in spent fuel canister design criteria.

Due to the uncertainties on geometry change during material degradation, various conservative assumptions could be applied. For the case of damaged fuels, the geometry of materials is not well known at the time of emplacement. Therefore, in the present work, two different cases have been defined and compared. Case (2) is considered more conservative but unphysical. However for case (1), due to the existence of cladding and structural materials, fuel particles could not be so closely packed, resulting in underestimation of k_{eff} due to optimistic assumption of poor moderation.

If the canister and the initial loading need to be designed to be subcritical according to the case (2) assumptions, several interesting points could be pointed out. First, depending on the initial loading, the maximum keff value might or might not occur before canister failure, when the canister contains maximum amount of fissile nuclides. Second, the maximum k_{eff} value could be almost independent from the initial loading, when the initial loading exceeds a threshold. The threshold is the mass of fuel when the canister is filled with fuel particles with optimized pitch distance for moderation. This quantity has already been defined as M_0^* =817 kg in Section 2.2.5.1 which is dependent on the dimension and material of the canister but independent of the initial mass loading. Even if the initial mass loading is much greater than the threshold, the maximum k_{eff} value will not increase; because (1) the maximum k_{eff} only occurs when the mass inside the canister is reduced to the amount of the threshold (see Section 2.2.5.1), and (2) the materials released from the canister contribute very little to the criticality (see Section 2.2.5.2).

From the above discussions, if the canister could be designed to be sub-critical with initial loading at M_0^*, the system is very likely to be sub-critical with initial mass loading higher than M_0^*. As a result, actual limit on the initial mass loading might not be coming from criticality, but by other constrains such as decay heat emission.

2.3 Parametric Study to Determine the Canister Mass Loadings for the Disposal of Fukushima Damaged Fuels

2.3.1 Background and Assumptions

Based on discussions in 2.2.5, for a fixed canister design, the maximum initial damaged fuels loadings can be determined in the following two steps. The first step is to perform a two-dimensional parametric search for the lattice constants in an infinite HCP lattice, and identify the parameter values that yield maximum neutron multiplicity for the infinite lattice (k_{inf}). In the second step, we consider the canister be filled with the fuel particle lattice with lattice constants identified in the first step. And search for maximum mass of damaged fuels that can be contained in the canister without making it critical. (If canister is still sub-critical even it has been fully filled, there will be no constraint for mass loading from criticality. However other constrains such as thermal power or volume may still be applied.)

The influence of fuel particle diameter needs to be further investigated. In the previous TMI defueling report, the fuel particle diameter was set so that the particle has the same volume of a fuel pellet. According to ref. [8], this assumption was made for two reasons. Firstly, the numerical results indicate that, in the infinite HCP lattice model, at optimized pitch distance for criticality, damaged fuel particles that are smaller than fuel pellets have lower k_{inf}. Therefore, it is conservative to model damaged fuels particles that are smaller than fuel pellets, to have equal sizes of the fuel pellets. Secondly, damaged fuels that are larger than fuel pellets could only occur after pellet meltdown and re-solidification, which make the fissile nuclide concentration much lower. They were therefore also modeled as the particles with same volume of fuel pellets. To verify same assumption could be made for the Fukushima damaged fuels, a parametric study for fuel particle diameter is needed.

In addition to the discussions above several additional improvements were recognized necessary. It has been reported that the k_{eff} could be maximum about 10^4 years after disposal due to actinide decay. But only situation at 1050 years or at 200050 years decay time was studied in our previous work. More time steps between 1050 years and 200050 years are assumed to discuss the effect of actinide decay on criticality. In later sections, the numerical scheme for the parametric study is firstly introduced. Numerical results for damaged fuels from Fukushima Unit 1-3 have been presented. Optimized lattice parameters are found for different fuels with different decay time. Using lattice parameters and decay time for criticality, the maximum canister loading have been calculated for damaged fuels from Unit 1-3 separately.

2.3.2 Method

The dimensions and material compositions of the canister-buffer system are the same as assumed in Section 2.2.3. A schematic view of the model is shown in Figure 2-1. The dimensions and compositions of the canister and buffer are shown in Table 2-3 and Table 2-4.

Based on the previous discussions, our work consists of two parts. To understand the general behavior of the fuel particle lattice, a parametric study for the infinite HCP lattice has been firstly performed. The MCNP simulations were made in a two-dimensional parameter space for the fuel particle diameters and the pitch-to-diameter ratio (or P/D for short). The P/D is commonly used in nuclear reactor analysis to describe the design of a fuel assembly. Based on the method developed in Section 2.2.2, the compositions of damaged fuels from Fukushima Unit 2 and Unit 3 are tabulated in Table 2-5 and Table 2-6. Nuclide compositions in Table 2-2, Table 2-5 and Table 2-6, are used to perform parametric study and to determine the canister mass loadings in later discussions. The neutron multiplicity for the infinite HCP lattice (k_{inf}) is calculated and presented in contour plots in the two-dimensional parametric space. The equivalent fuel particle diameter based on the pellet diameter of STEP-III fuel has been calculated in Section 2.2.3.

Table 2-5: Composition of damaged fuels from Fukushima-Daiichi Unit 2 reactor.

	Amount of nuclides (mole) for different decay times from the accident (values cut-off at one mole)				
Nuclide	50 (yr)	1050 (yr)	10050 (yr)	100050 (yr)	200050 (yr)
Rh-103	2.95E+02	2.95E+02	2.95E+02	2.95E+02	2.95E+02
Nd-143	3.95E+02	3.95E+02	3.95E+02	3.95E+02	3.95E+02
Nd-145	3.17E+02	3.17E+02	3.17E+02	3.17E+02	3.17E+02
Sm-147	1.32E+02	1.32E+02	1.32E+02	1.32E+02	1.32E+02
Sm-149	1.69E+00	1.69E+00	1.69E+00	1.69E+00	1.69E+00
Sm-150	1.21E+02	1.21E+02	1.21E+02	1.21E+02	1.21E+02
Sm-152	4.88E+01	4.88E+01	4.88E+01	4.88E+01	4.88E+01
Eu-151	1.97E+00	6.06E+00	6.06E+00	6.06E+00	6.06E+00
Eu-153	4.62E+01	4.62E+01	4.62E+01	4.62E+01	4.62E+01
Gd-155	2.85E+00	2.86E+00	2.86E+00	2.86E+00	2.86E+00
U-233			1.30E+00	1.09E+01	1.76E+01
U-234	1.17E+01	3.44E+01	3.41E+01	3.10E+01	2.84E+01
U-235	7.24E+03	7.28E+03	7.64E+03	8.78E+03	8.87E+03
U-236	1.27E+03	1.32E+03	1.60E+03	1.78E+03	1.77E+03
U-238	3.74E+05	3.74E+05	3.74E+05	3.74E+05	3.74E+05
Np-237	1.19E+02	3.63E+02	4.23E+02	4.11E+02	3.97E+02
Pu-238	2.26E+01	1.58E+03			
Pu-239	1.63E+03	4.62E+02	1.23E+03	9.25E+01	5.19E+00
Pu-240	5.13E+02	3.44E+01	1.78E+02		
Pu-241	2.76E+01				
Pu-242	9.98E+01	9.97E+01	9.81E+01	8.35E+01	6.98E+01
Am-241	2.77E+02	6.14E+01			
Am-243	1.65E+01	1.50E+01	6.45E+00		

Table 2-6: Composition of damaged fuels from Fukushima-Daiichi Unit 3 reactor.

	Amount of nuclides (mole) for different decay times from the accident (values cut-off at one mole)				
Nuclide	50 (yr)	1050 (yr)	10050 (yr)	100050 (yr)	200050 (yr)
Rh-103	2.82E+02	2.82E+02	2.82E+02	2.82E+02	2.82E+02
Nd-143	3.79E+02	3.79E+02	3.79E+02	3.79E+02	3.79E+02
Nd-145	3.01E+02	3.01E+02	3.01E+02	3.01E+02	3.01E+02
Sm-147	1.27E+02	1.27E+02	1.27E+02	1.27E+02	1.27E+02
Sm-149	1.76E+00	1.76E+00	1.76E+00	1.76E+00	1.76E+00
Sm-150	1.13E+02	1.13E+02	1.13E+02	1.13E+02	1.13E+02
Sm-152	4.66E+01	4.66E+01	4.66E+01	4.66E+01	4.66E+01
Eu-151	2.01E+00	6.20E+00	6.21E+00	6.21E+00	6.21E+00
Eu-153	4.30E+01	4.30E+01	4.30E+01	4.30E+01	4.30E+01
Gd-155	2.71E+00	2.71E+00	2.71E+00	2.71E+00	2.71E+00
U-233			1.39E+00	1.18E+01	1.90E+01
U-234	1.73E+01	4.47E+01	4.41E+01	3.88E+01	3.43E+01
U-235	7.19E+03	7.24E+03	7.67E+03	9.00E+03	9.10E+03
U-236	1.21E+03	1.28E+03	1.65E+03	1.88E+03	1.87E+03
U-238	3.75E+05	3.75E+05	3.75E+05	3.75E+05	3.75E+05
Np-237	1.13E+02	3.87E+02	4.55E+02	4.42E+02	4.27E+02
Pu-238	2.73E+01				
Pu-239	1.91E+03	1.86E+03	1.44E+03	1.08E+02	6.08E+00
Pu-240	6.71E+02	6.04E+02			
Pu-241	3.09E+01	1.16E+02			
Pu-242	1.16E+02	6.92E+01	2.33E+02	9.68E+01	8.09E+01
Am-241	3.12E+02	1.44E+01	1.14E+02		
Am-243	1.58E+01	1.86E+03	6.18E+00		

2.3.3 Numerical Results

The contour plots of k_{inf} for particle diameters ranging from 0.4 cm to 4.0 cm, P/D ranging from 1.0 to 1.9, and decay time ranging from 50 years to 200050 years are presented for damaged fuels from Fukushima Unit 1 (see Figure 2-6 to Figure 2-10). The red contour lines indicate for k_{inf} =1.0. And the dashed blue line indicate the maximum k_{inf} for D=1.11 cm. To avoid showing similar results with shared tendency, the contour plots for Unit 2 (Figure A-1 to Figure A-5) and Unit 3 (Figure A-6 to Figure A-10) are shown in Appendix A. 1. The parameter ranges for particle diameters and P/D was set to contain the maximum k_{inf}, which is crucial for our study. Based on the numerical results, we expect same tendency to be observed in extended parameter ranges. The P/D ratio can also be presented in terms of the particle volume fraction *f*, which is shown in the right vertical axis of the figures. The relation between P/D and *f* is shown in equation(2-3). Because P/D should always be greater than one, *f* has a maximum value about 0.74.

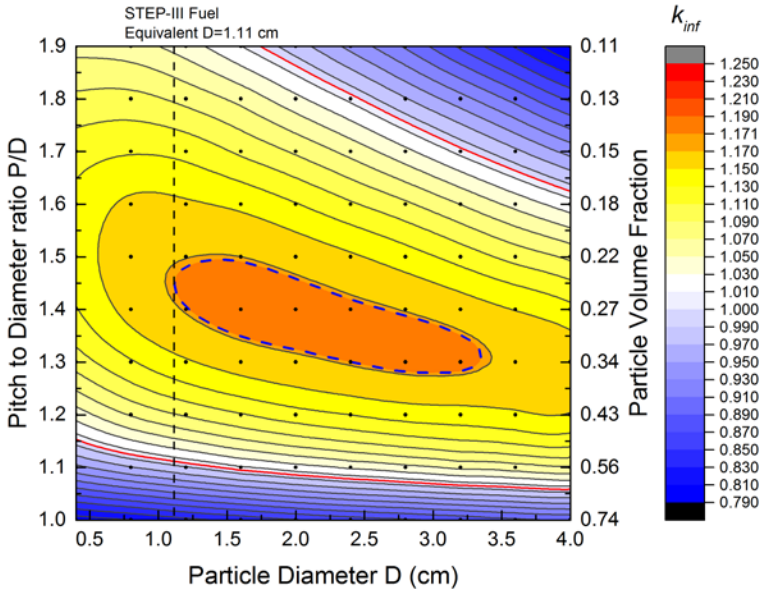

Figure 2-6: K_{inf} contour plot for the damaged fuels from Fukushima Unit 1 in infinite HCP lattice, after 50 years decay. The red contour lines indicate for k_{inf} =1.0. The dashed blue line indicate the maximum k_{inf} for D=1.11 cm.

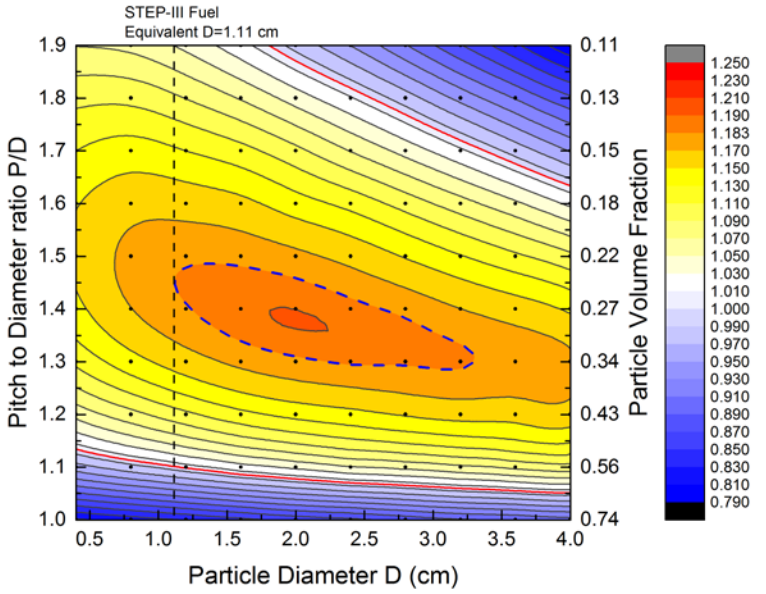

Figure 2-7: K_{inf} contour plot for the damaged fuels from Fukushima Unit 1 in infinite HCP lattice, after 1050 years decay. The red contour lines indicate for k_{inf} =1.0. The dashed blue line indicate the maximum k_{inf} for D=1.11 cm.

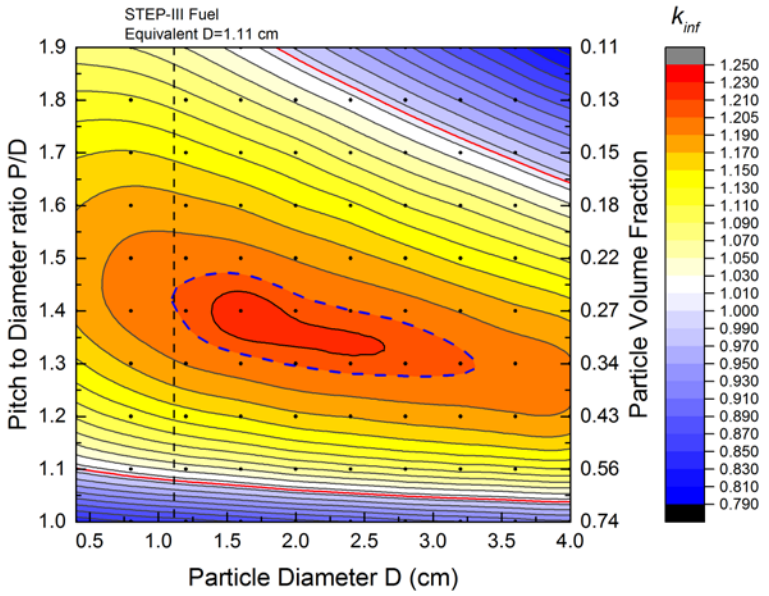

Figure 2-8: K_{inf} contour plot for the damaged fuels from Fukushima Unit 1 in infinite HCP lattice, after 10050 years decay. The red contour lines indicate for k_{inf} =1.0. The dashed blue line indicate the maximum k_{inf} for D=1.11 cm.

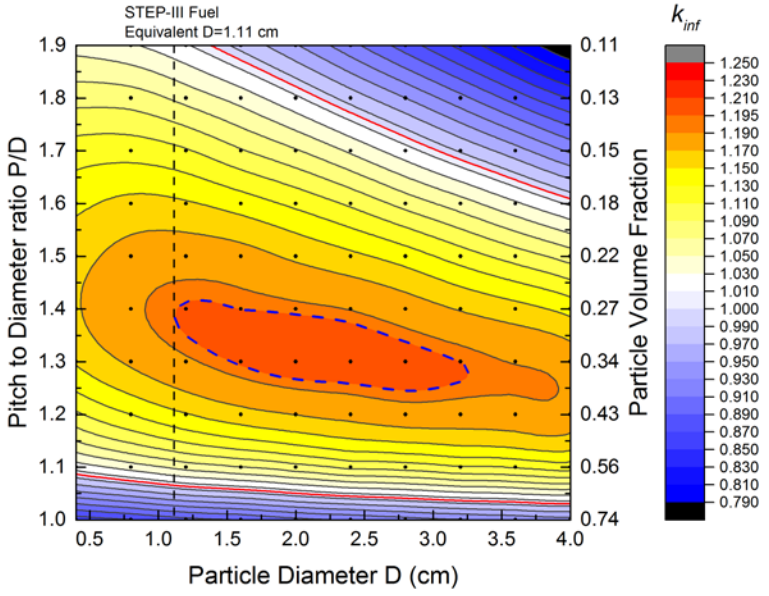

Figure 2-9: K_{inf} contour plot for the damaged fuels from Fukushima Unit 1 in infinite HCP lattice, after 100050 years decay. The red contour lines indicate for k_{inf} =1.0. The dashed blue line indicate the maximum k_{inf} for D=1.11 cm.

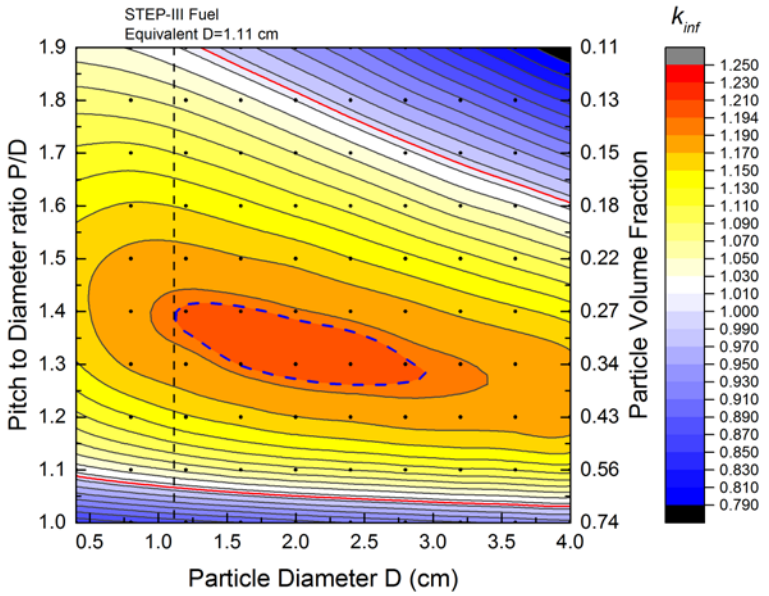

Figure 2-10: K_{inf} contour plot for the damaged fuels from Fukushima Unit 1 in infinite HCP lattice, after 200050 years decay. The red contour lines indicate for k_{inf} =1.0. The dashed blue line indicate the maximum k_{inf} for D=1.11 cm.

Similar patterns are found in these contour plots; Results for damaged fuels from Fukushima Unit 1 have been discussed in details, so that the results for Unit 2 and 3 could be easily understood. We could immediately notice that the neutron multiplicity changes drastically as P/D changes the k_{inf} gain significant increase as P/D increase, and then gradually decrease when the system is over-moderated. The red contour lines are for k_{inf} =1.0, between the two red contour lines, critical mass has a finite value.

When the diameter is smaller than about 2 cm, the contour lines have a convex shape towards left the vertical axis. If we consider different diameters within that parameter range, at an optimized P/D, the k_{inf} will be higher for larger diameter. Because the diameter equivalent to the STEP-III fuel (the black dashed line) is within this range, the previous assumption that the particle diameter should be fixed at its maximum (equivalent to initial fuel pellet) is now verified.

To reiterate the discussions, we assume the fuel particle diameter was set so that the particle has the same volume of a fuel pellet. This assumption was made for two reasons. Firstly, the numerical results indicate that, in the infinite HCP lattice model, at optimized pitch distance for criticality, damaged fuel particles that are smaller than fuel pellets have lower k_{inf}. Therefore, it is conservative to model damaged fuels particles that are smaller than fuel pellets, to have equal sizes of the fuel pellets. Secondly, damaged fuels that are larger than fuel pellets could only occur after pellet meltdown and re-solidification, which makes the fissile nuclide concentration much lower. They were therefore also modeled as the particles with same volume of fuel pellets.

We then draw a contour line (in blue) that tangent to the black dashed line. The blue contour line then indicates the maximum k_{inf} value and the tangent point gives the optimized P/D. For example, for Unit 1 damaged fuels after 50 years decay, in Figure II-2, the maximum k_{inf} is 1.1174 when P/D=1.45.

In all results, the optimized P/D shifts to lower value as the particle diameter increases. A qualitative explanation for this tendency is that, as the particle diameter increases, less thermal neutron could reach the center of the particle due to self-shielding effect. As a result, the system favors fissions at higher energy. Therefore, the optimized moderation shifts to harder spectrum or lower P/D.

The change of the system over the range of decay times also has influences on the k_{inf} values and the optimized moderation condition. More discussions are given in the next section.

Comparing damaged fuels from three cores (for example, by Figure 2-8, Figure A-3, and Figure A-8), due to relative lower fissile nuclide concentration, Unit 1 damaged fuels generally show lower k_{inf} than the other two cases. Unit 3 results are slightly higher than Unit 2, but the two cases are quite similar. We would expect the canister loading limit for the three cases be in the order of Unit 1 > Unit 2 > Unit 3.

2.3.4 Discussions

2.3.4.1 Influence of Actinides Decay

Comparing the k_{inf} contour for decay times ranging from 50 years to 200050 years, we observe that the results for fuels from three damaged cores share a common tendency. For example, Figure 2-11 shows the neutron multiplicity plot versus decay time for damaged fuel from Fukushima Unit 1, where k_{inf} values are calculated for infinite HCP lattice with D=1.2 cm and P/D=1.4. The k_{inf} is slightly increased from 50 years decay to 1050 years decay, and then continue increasing until reaches the maximum after 10050 years decay. The k_{inf} is then decreased after 100050 years decay and continue decreasing after 200050 years decay. According to Section 2.2.2, with more than 50 years decay, the remaining neutron poisons in fission products are all stable. Therefore, changes of the k_{inf} results are only due to actinides decay. The actinides compositions of damaged fuels from Unit 1 are made into two groups (based on their amount in the core) and are shown in Figure 2-12 and Figure 2-13. Only actinides with amount more than 1 mole (at any decay time) are displayed. Because in the problem concerned, fissions mainly occur in thermal energy, neutron cross sections [33] at thermal energy (0.0253 eV) are used in the later discussions.

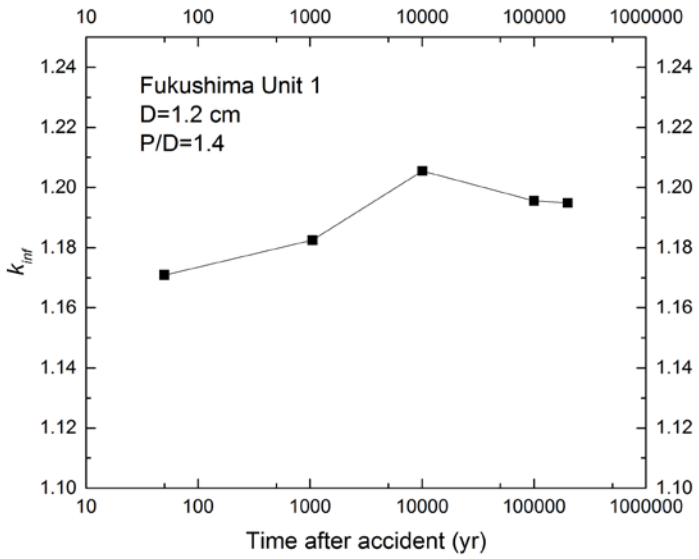

Figure 2-11: Neutron multiplicity plot versus decay time for damaged fuel from Fukushima Unit 1, kinf values are calculated for infinite HCP lattice with D=1.2 cm and P/D=1.4.

Comparing the actinide compositions for 50 years decay and 1050 years decay, the most important nuclide decay chains are Pu-241->Am-241->Np-237 and Pu-238-> U-234. With half-life of 14 years, about 20 moles of Pu-241 remains after 50 years decay, which quickly decays to Am-241 in the next hundred years. The major cause of the increase of k_{inf} is the relatively more neutron absorbing nuclides decaying to less absorbing daughter nuclides. Am-241 (with the thermal neutron capture cross section $\sigma_{2200}^{(n,\gamma)} = 684.3b$) decays to less absorbing Np-237 ($\sigma_{2200}^{(n,\gamma)} = 178.1b$) with a half-life of 432.2 years; And Pu-238 ($\sigma_{2200}^{(n,\gamma)} = 412b$) decays to less absorbing U-234 ($\sigma_{2200}^{(n,\gamma)} = 100.3b$) with a half-life of 87.7 years.

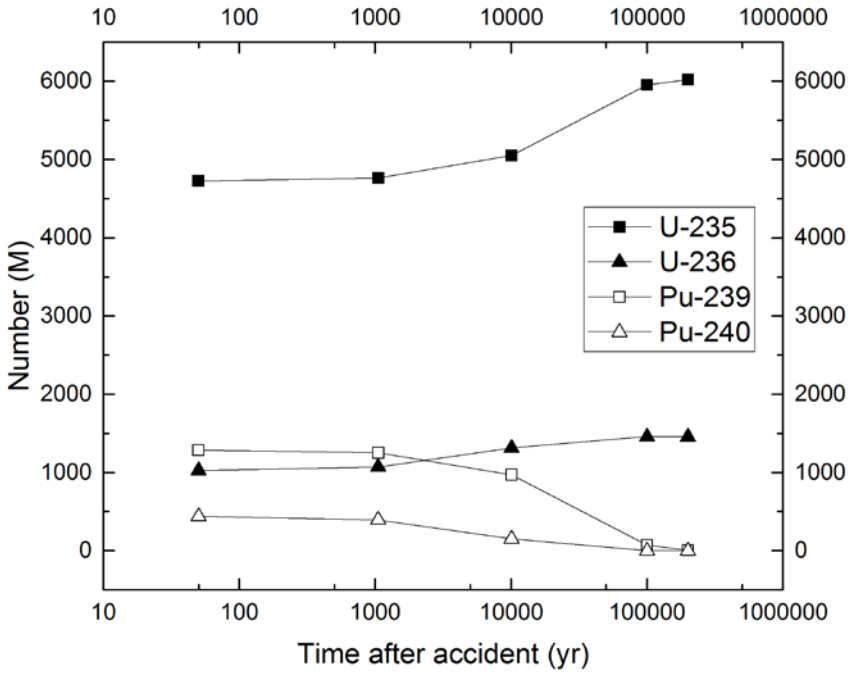

Figure 2-12: Amount of actinides in Fukushima Unit1 damaged fuel versus decay times for actinides with initial amount more than 400 moles.

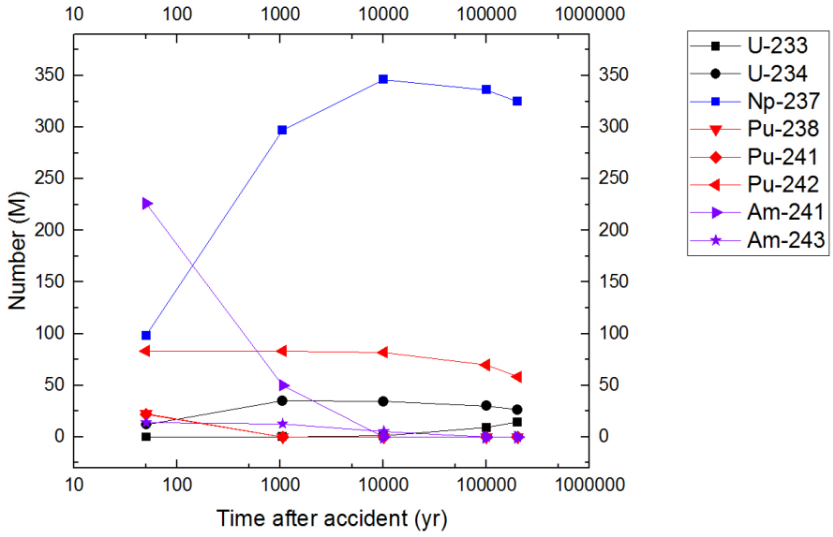

Figure 2-13: Amount of actinides in Fukushima Unit1 damaged fuel versus decay times for actinides with initial amount less than 400 moles.

Between 1050 years to 10050 years, Am-241 decays to Np-237 which reduce the neutron absorption. At the same time, Pu-240 ($\sigma_{2200}^{(n,\gamma)} = 289.3b$) decays to less absorbing

U-236 ($\sigma_{2200}^{(n,\gamma)} = 5.123b$) with half-life of 6563 years. These two factors further increase the k_{inf} values during the decay time. The Pu-240 to U-236 decay is more important because the relatively higher amount of Pu-240 in the damaged fuels.

During time from 10050 to 100050 years, Pu-240's decay further decreases the neutron absorption. But a much stronger influence comes from the Pu-239 to U-235 decay. Because Pu-239 has both larger thermal fission and capture than U-235, the net effect is that the system's k_{inf} decreases when Pu-239 decays to U-235. This trend continues till the decay time of 200050 years. By that time, almost all Pu-239 has decayed.

To summarize the discussions above, during a hundred years until ten thousand years' time range, the neutron multiplicity increases due to some neutron absorbing nuclides decay to less absorbing daughters. From ten thousand years and on, the decay of Pu-239 lowers the neutron multiplicity. The net effect is that the neutron multiplicity reaches its maximum at around ten thousand years. We should emphasize that, with the five time steps considered, the present work only demonstrate and explain the general behavior of the k_{inf}. To obtain more accurate time to reach the maximum k_{inf}, additional work with more time steps is needed.

2.3.4.2 Canister Mass Loadings

With results shown in the previous sections, we can now calculate the canister mass loading for damaged fuels from three reactor cores. Recall the method described in Section 2.3.2. Because we assumed the fuel particle diameter be fix (at D=1.11 cm), the first step is find the optimized P/D and corresponding k_{inf} for each decay time, which can be done graphically by considering the black and blue dashed lines in Figure 2-6 to Figure 2-10 and in Figure A-1 to Figure A-10. For example, in Figure 2-6, the optimized P/D=1.45, and the corresponding k_{inf} is 1.1174. The P/D values and corresponding values for three damaged cores at different decay times after the accident are tabulated in Table 2-7 to Table 2-9. The second step is to compare the k_{inf} values (with optimized P/D) at different decay times. For example, for damaged fuels from Fukushima Unit 1, comparing k_{inf} values at optimized P/D in Table 2-7, the maximum k_{inf} was found when decay time is 10050 years. The same process can be repeated for damaged fuels from Unit 2 and Unit 3.

Using the parameter values highlighted in Table 2-7 to Table 2-9, we can calculate the k_{eff} value of the canister-buffer model (see Figure 2-1) for a given lattice filling height H. If the system is critical when the lattice filling height equals to some value no greater than the canister height h, the corresponding mass of damaged fuels can be considered as the maximum canister loading. For the canister design assumed in our work, the maximum canister loadings can be calculated for damaged fuels from three damaged cores. The calculated results are shown in Table 2-10. Comparing damaged fuels from three cores, Unit 1 damaged fuels have relatively lower fissile nuclide concentrations, due to lower initial enrichment (part of the fuel in Unit is STEP-II) and higher average burnup[1] (25.9 GWd/t) at the time of the accident. As a result the mass loadings limit is higher than the other two cases.

If we convert the mass of damaged fuel (assumed the property of UO_2) into mass of heavy metal, the number of canister can be estimated. Approximately a thousand canisters are required according to the canister loadings suggested.

Table 2-7: Lattice parameters for maximum k_{inf} values loadings for damaged fuels from Unit 1 with different decay times.

Decay time from the accident (yr)	D (cm)	P/D	k_{inf}
50	1.11	1.45	1.1714
1050	1.11	1.45	1.1833
10050	1.11	1.42	1.2045
100050	1.11	1.39	1.1948
200050	1.11	1.39	1.1939

Table 2-8: Lattice parameters for maximum k_{inf} values loadings for damaged fuels from Unit 2 with different decay times.

Decay time from the accident (yr)	D (cm)	P/D	k_{inf}
50	1.11	1.45	1.2040
1050	1.11	1.44	1.2162
10050	1.11	1.43	1.2357
100050	1.11	1.39	1.2302
200050	1.11	1.39	1.2271

Table 2-9: Lattice parameters for maximum k_{inf} values loadings for damaged fuels from Unit 3 with different decay times.

Decay time from the accident (yr)	D (cm)	P/D	k_{inf}
50	1.11	1.47	1.2066
1050	1.11	1.46	1.2190
10050	1.11	1.43	1.2447
100050	1.11	1.40	1.2375
200050	1.11	1.40	1.2358

Table 2-10: Maximum canister loadings and estimated number of canisters for damaged fuels from unit 1, 2, and 3.

Cases	Maximum loading per canister [kg](k_{eff}=0.98)	Mass of heavy metal in fresh fuel [ton]	Estimated number of canisters
Core 1	356	69	219
Core 2	282	94	379
Core 3	269	94	396
Total		257	994

2.4 Near-Field Analysis for the Disposal of Spent Fuels with Different Initial Enrichments and Burnups

2.4.1 Background and Assumptions

The repository is assumed to be in a water-saturated reducing environment. The neutronics model consists of a canister containing spent fuel and the buffer material surrounding the canister. The composition and dimension of the canister and the buffer for BWR and PWR spent fuels are assumed according to the design developed by JAEA[4]. The BWR canister contains seven assemblies, and the PWR canister contains two assemblies.

The spent fuels are assumed to be emplaced in the repository after 50 years of cooling, the canister failure time is assumed to be 1000 years after emplacement. After its failure, the canister is assumed to be filled with groundwater. The failure of assembly structures and claddings is assumed to be a transient event in a time scale of thousand years. Therefore, we assume the spent fuels exist in the form of pellets immediately after the canister failure. In a reducing environment, the fuel pellets dissolves and are released from the canister over the next hundreds of thousands of years. The BWR assembly design is assumed to be STEP-III B[31] type, and the PWR assembly is assumed to be 17×17 type. Although these assembly designs are for UO_2 fuels, same conditions are assumed for MOX fuels. Numerical results for specific MOX fuel design can be generated in the future. Because the present work only consider the situation when assembly structures and claddings have failed, in our model, the assembly designs would only affect the mass of the spent fuel to be contained per canister, and the size of the fuel particles. Spent fuels with different initial enrichments and burnups are considered. They are described in details in later discussions.

For the system, including the spent fuel pellets, the canister, and the buffer remains subcritical during the fuel dissolution time, we need to explore under what conditions the neutron multiplicity of the system can be maximized.

2.4.2 Method and Numerical Scheme

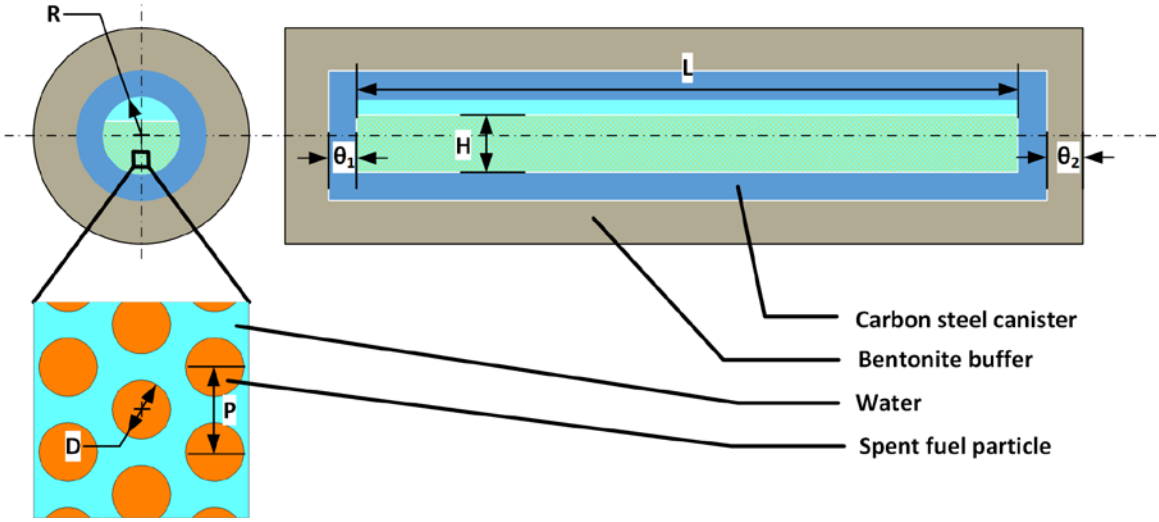

Figure 2-14: Schematic layout of the canister-buffer system. The carbon-steel canister is filled with spent fuel particles in HCP lattice and is surrounded by bentonite buffer.

The present work aims at calculating numerical results over a broad range of input parameters including lattice parameters and different spent fuels. The numerical scheme needs to be carefully designed to reduce the computation time. The criticality calculations have been carried out by a Monte-Carlo code called SERPENT[34]. The SERPENT code is publicly available and has been distributed by the OECD/NEA Data Bank and RSICC. For criticality calculations, the SERPENT code has been well validated. A comparison between MCNP and SERPENT results for a set of standard benchmarking problems can be found in ref. [35]. The results calculated by the two codes agreed sufficiently well, and SERPENT is at least eight times faster than MCNP[35]. By using the SERPENT code, the computation time has been greatly reduced.

Based on the discussions in the previous section, the first step of the numerical scheme is to identify the fuel particle diameter and the pitch distance to give maximum k_{inf} for the infinite HCP lattice for different spent fuels at different decay times. To make the parameter search more efficiently, a broad survey has been firstly made in a two-dimensional parameter space (diameter and pitch distance) for BWR and PWR UO_2 spent fuels with different values for the initial enrichment (IE), burnup (BU), and decay time.

The compositions for spent fuels are calculated in ref. [22], for UO_2 and MOX fuels from BWRs and PWRs with different burnups and initial enrichments. The burnup calculations have been carried out by ORIGEN-ARP using an input generator developed in ref. [22]. For most LWR spent fuels, the ratio of discharge burnup [MWd/t] to initial enrichment [wt. %] is typically between 9 and 12. Therefore, three combinations of initial enrichment and burnup (IE = 2.0%, BU = 20GWd/t; IE = 4.0%, BU = 40 GWd/t, IE= 6.0 %) have been considered, which crudely cover the parameter range of common spent fuels. Combining two reactor types (BWR/PWR), three initial enrichment and burnup

cases, and three decay times (1050, 10050, and 100050 years), eighteen cases in total have been calculated.

Based on the numerical results from the two-dimensional parametric search (see Section 2.4.3.1), the parameter search has been reduced to one-dimensional. A second round of the parametric search has been made for more cases of burnup and initial enrichment for UO_2 and MOX fuels. For UO_2 spent fuels, 20 cases of burnup and initial enrichment have been calculated for both BWR and PWR spent fuels. The cases roughly covered the burnup to initial enrichment ratio range between 9 and 12[36]. Due to the relative lack of industry experience with MOX fuels, 42 cases have been defined by combing the burnup ranging from 10 GWd/t to 60 GWd/t and the plutonium weight fraction ranging from 4.0% to 10.0%. The isotopic fractionations of plutonium isotopes in the MOX fuels are shown in Table 2-11.[22]

Table 2-11: Isotopic fractionation of plutonium isotopes in the simulated MOX fuels.

Isotope	wt.%
Pu-238	1.5
Pu-239	60.1
Pu-240	24.5
Pu-241	8.8
Pu-242	5.0

The combination of the fuel particle diameter and the pitch distance to give maximum k_{inf} has been identified for each case. Then, we have calculated the k_{eff} values using the diameters and pitch distances in the canister-buffer model to examine whether the canister could be critical.

The input parameters for the BWR and PWR canisters are shown in Table 2-12. The canister and the buffer compositions are assumed to be the same as was shown in shown Table 2-4. The total volume inside the canister V_0 can be calculated by $V_0 = \pi r^2 L$, where r is the canister inner radius, and L is the canister inner length. The total volume of spent fuel per canister (V) is defined as $V = N \times n \times \frac{1}{4}\pi d^2 l$, where N is the number of assembly per canister, n the number of fuel rods per assembly, d the pellet diameter, and l the fuel length. The fuel particle diameter D in the present model has been determined to give the same volume of a cylindrical fuel pellet. The length of a fuel pellet is assumed to be 1 cm.

Note that same fuel design parameters for UO_2 fuels are assumed for MOX fuels. Numerical results for specific MOX fuel design can be generated in the future. Because the present work only consider the situation when assembly structures and claddings have failed, the fuel designs would only affect the mass of the spent fuel to be contained per canister, and the size of the fuel particles.

Table 2-12: Summary of input parameters for BWR and PWR spent fuel canisters.

Canister design parameters[4]	**BWR**	**PWR**
Canister inner radius r [cm]	34.40	27.95
Canister inner length L [cm]	450	450
Canister thickness θ_1 [cm]	14	14
Buffer thickness θ_2 [cm]	70	70
Number of assemblies per canister N	7	2
Fuel design parameters	**BWR**	**PWR**
Fuel type	BWR STEP-III B type	PWR 17x17 type
Fuel length l [m]	3.71	3.6
Number of fuel rods per assembly n	72	264
Fuel density	97% of theoretical density	95% of theoretical density
Pellet diameter [cm]	0.96	0.82
Calculated model parameters	**BWR**	**PWR**
Volume inside canister V_0	1.672	1.104
Total spent fuels volume V [m^3]	0.1353	0.1003
Fuel particle diameter D [cm]	1.114	1.003

2.4.3 Results and Discussions

2.4.3.1 Two-dimensional Parametric Study for BWR and PWR Spent Fuels in Infinite HCP Lattice

The parametric study on kinf has been performed for the particle diameters D ranging from 0.4 cm to 1.4 cm, and P/D ranging from 1.0 to 1.7. To understand the general behavior, totally six combinations of burnups, enrichments and fuel types have been calculated. These cases cover the low burnup, low enrichment fuels (BU = 20 GWd/t, IE = 2.0%); mid burnup, mid enrichment fuels (BU = 40 GWd/t, IE = 4.0%); and high burnup, high enrichment fuels (BU = 60 GWd/t, IE = 6.0%) for BWRs and PWRs. For example, the k_{inf} contours for BWR (STEP-III-B) type UO_2 spent fuels with burnup of 40 GWd/t and initial enrichment of 4.0% are plotted for decay times of 1050, 10050, and 100050 years, in Figure 2-15, Figure 2-16 and Figure 2-17, respectively. Results for other cases are included in Figure A-11 to Figure A-25, in Appendix A. 2. Because the numerical results show similar tendency for different cases, we hereafter discuss the results shown in Figure 2-15, Figure 2-16 and Figure 2-17 as examples, so that other results could be similarly understood.

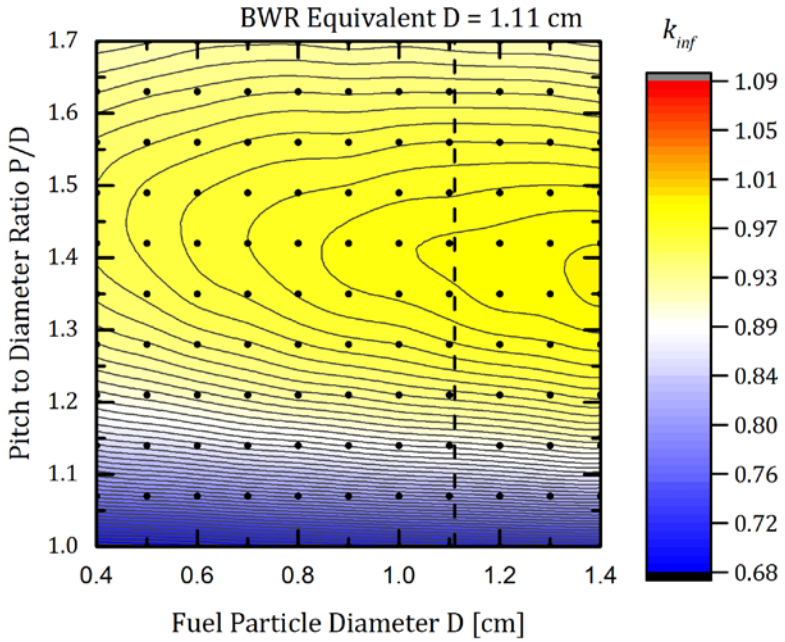

Figure 2-15: K_{inf} contour plot for BWR UO_2 spent fuel in infinite HCP lattice, after 1050 years decay. The spent fuel has burnup of 40 GWd/t and initial enrichment of 4.0%.

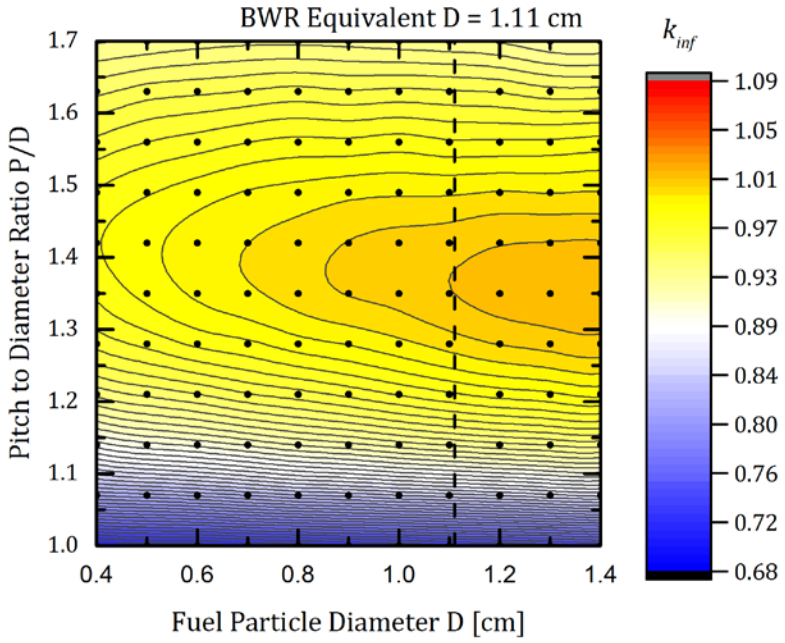

Figure 2-16: K_{inf} contour plot for BWR UO_2 spent fuel in infinite HCP lattice, after 10050 years decay. The spent fuel has burnup of 40 GWd/t and initial enrichment of 4.0%.

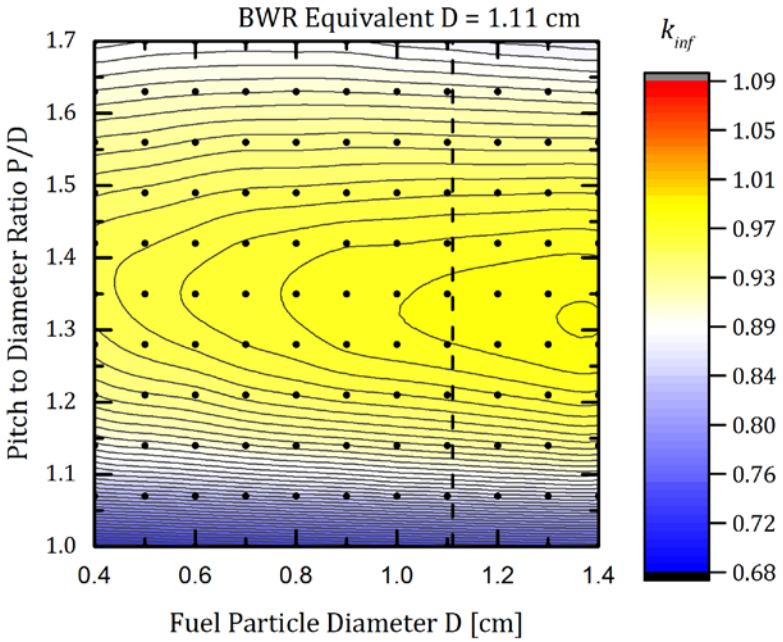

Figure 2-17: K_{inf} contour plot for BWR UO_2 spent fuel in infinite HCP lattice, after 100050 years decay. The spent fuel has burnup of 40 GWd/t and initial enrichment of 4.0%.

Like the numerical results presented for the damaged fuels in Section 2.3, the first observation is that, the neutron multiplicity changes drastically as P/D changes. For a given diameter D, the k_{inf} gain significant increases as P/D increases, and then gradually decreases when the system is over-moderated. The diameter D of the spherical fuel particle that has same volume of a BWR fuel pellet (D = 1.11 cm) is indicated by the vertical dashed line in the contour plots. Because we assumed the spent fuel particles are only shrinking during dissolution, the diameters should be equal or smaller than 1.11 cm. The parameter pair that maximizes the k_{inf} value should always be found on the dashed line, because for the left side of the dashed line, the contour lines always have a convex shape toward smaller diameter values. This is a general observation for all calculated cases (shown in Figure 2-15 to Figure 2-17, and Figure A-11 to Figure A-25), which cover the range of different spent fuels. Therefore, we can simplify the parameter search from two-dimensional to one-dimensional, i.e., to fix the diameter at its maximum value and search for pitch distances to maximize the k_{inf}. With this simplification, we can perform the one-dimensional parametric search for the pitch distance with a smaller step length. The results are discussed in the next section.

Comparing the k_{inf} results for the three different decay times, the highest k_{inf} values are generally found in the 10050-year decay case. The reason for this has been discussed for the damaged fuels case in Section 2.3.4.1. Again, it is important to notice that, with only three time steps considered, the present work only demonstrate the general behavior of the k_{inf}. To obtain more accurate time to reach the maximum k_{inf}, additional work with more time steps is needed.

2.4.3.2 One-dimensional Parametric Search on Pitch Distance

One-dimensional parametric search on the pitch distance was made for different spent fuel types with three different decay times to search for the maximum k_{inf}. For UO_2 spent fuels, 20 cases of burnup and initial enrichment have been calculated for both BWR and PWR spent fuels. The combinations are defined according to the range of common spent fuels shown in Figure II-2. For all cases, the maximum k_{inf} values and corresponding P/D ratios are tabulated in Table 2-13 for BWR spent fuels and in Table 2-14 for PWR spent fuels. For MOX fuels, 42 cases were defined by combing burnup ranging from 10 GWd/t to 60 GWd/t (with 10 GWd/t increment) and plutonium weight fraction ranging from 4.0% to 10.0% (with 1.0% increment). The isotopic composition of plutonium was defined in ref. [22]. The numerical results are tabulated in Table 2-15 and Table 2-16 for BWR and PWR spent fuels, respectively.

If we fix the same fuel type, burnup, and initial enrichment/plutonium weight fraction, and compare the results for different decay times, the maximum k_{inf} is found at the 10050 years decay. The same observation has been made and explained in the previous section. It has also been observed that the pitch distance that maximizes the k_{inf} tends to decrease with increasing decay time. The reason is probably that, for Pu-239, due to the resonance neutron capture in epithermal energy, Pu-239 favors higher moderation than U-235. As a result, the higher fraction of Pu-239 among the fissile nuclides, the higher moderation (meaning larger pitch distance) the system requires to reach maximum k_{inf}. That explains two observations from the results. First, as time increase, Pu-239 decays to U-235, resulting in the decrease of the pitch distance for maximum $k_{inf.}$ Second, the pitch distance for maximum k_{inf} is always higher for MOX fuels than in UO_2 fuels, because the fissile nuclide initially in the MOX spent fuels is mainly Pu-239.

Comparing spent fuels with different burnup and initial enrichments, it is obvious that the k_{inf} is higher, for lower burnup or higher initial enrichment, because in either situation, there is greater mass of fissile nuclides remaining in the spent fuels. Another interesting observation is that, for same burnup and initial enrichment, the PWR spent fuels gives slightly higher k_{inf} than the BWR spent fuels. This is actually a net effect of two opposing factors: the PWRs generally breed more fissile nuclides than BWRs (see next section) and thus more fissile nuclides remain in the spent fuels; while the BWRs have larger pellets than the PWRs, which is more favored for higher k_{inf}.

The next step is to apply the results from the parameter search to calculate the k_{eff} values of the canister-buffer system. The canister design and initial spent fuel loadings have been described in Section 2.4.2. The first task is to examine whether or not the fuel particle diameter and the pitch distance identified from the parameter search could be realized for the given canister design and initial loadings. In other words, we need to check if the canister will be over-filled if such lattice parameters are assumed. From Table 2-12, the total spent volume is 0.1353 m^3 for BWR canisters and is 0.1003 m^3 for PWR canisters. The packing fraction f (the volume fraction of fuel particles), in the present situation, for the HCP lattice with the particle diameter D and the pitch distance P is given by equation(2-3). Among all calculated cases, the maximum P/D value is 1.78 for both BWR and PWR cases. Therefore, by equation(2-3), the packing fraction f should be larger than 0.1313. Therefore, the maximum volume of the HCP lattice is 0.1353 m^3 /

0.1313 = 1.0305 m^3 for BWR canisters, and 0.1003 m^3 / 0.1313 = 0.7639 m^3 for PWR canisters. Apparently, these values are smaller than the canister volumes calculated in Table 2-12, which is 1.672 m^3 for BWR canisters, and 1.104 m^3 for PWR canisters. Therefore, based on the discussions in Section 2.4.1, we assume all initial spent fuels to be included inside the canister.

Table 2-13: Results for parametric search on pitch distances for the maximum neutron multiplicity in infinite HCP lattice for BWR UO_2 spent fuels after different decay times.

Burnup [GWd/t]	Initial enrichment [wt. %]	After 1050 years decay		After 10050 years decay		After 100050 years decay	
		P/D to maximize k_{inf}	k_{inf}	P/D to maximize k_{inf}	k_{inf}	P/D to maximize k_{inf}	k_{inf}
10	1.5	1.32	1.051290	1.32	1.063180	1.28	1.02586
20	2.0	1.32	0.965839	1.30	0.984536	1.28	0.94206
20	2.5	1.40	1.058400	1.36	1.078890	1.32	1.05041
30	2.5	1.36	0.892926	1.32	0.915328	1.26	0.86432
30	3.0	1.38	0.978616	1.34	1.002160	1.32	0.9665
30	3.5	1.40	1.056530	1.38	1.081060	1.36	1.05899
40	3.0	1.32	0.833815	1.32	0.857740	1.28	0.79838
40	3.5	1.38	0.908457	1.36	0.932628	1.28	0.88829
40	4.0	1.40	0.983599	1.38	1.007820	1.32	0.97787
40	4.5	1.42	1.052450	1.38	1.077290	1.36	1.05838
50	3.5	1.38	0.782677	1.30	0.809221	1.26	0.74385
50	4.0	1.38	0.847421	1.34	0.873745	1.3	0.82084
50	4.5	1.40	0.916320	1.36	0.942113	1.3	0.90314
50	5.0	1.40	0.982588	1.42	1.010060	1.36	0.98329
50	5.5	1.46	1.047180	1.44	1.074600	1.4	1.05713
60	4.0	1.34	0.740621	1.32	0.769110	1.28	0.69599
60	4.5	1.38	0.794902	1.32	0.822976	1.3	0.76185
60	5.0	1.38	0.855571	1.36	0.883673	1.3	0.83431
60	5.5	1.40	0.920547	1.36	0.949030	1.36	0.91157
60	6.0	1.44	0.980829	1.42	1.010600	1.38	0.98469

Table 2-14: Results for parametric search on pitch distances for the maximum neutron multiplicity in infinite HCP lattice for PWR UO_2 spent fuels after different decay times.

Burnup [GWd/t]	Initial enrichment [wt. %]	After 1050 years decay		After 10050 years decay		After 100050 years decay	
		P/D to maximize k_{inf}	k_{inf}	P/D to maximize k_{inf}	k_{inf}	P/D to maximize k_{inf}	k_{inf}
10	1.5	1.36	1.057610	1.32	1.067830	1.26	1.02598
20	2.0	1.36	1.006610	1.34	1.023080	1.3	0.97488
20	2.5	1.38	1.086230	1.38	1.105400	1.32	1.07103
30	2.5	1.38	0.959072	1.38	0.981865	1.3	0.92557
30	3.0	1.40	1.030330	1.40	1.051540	1.34	1.01113
30	3.5	1.42	1.095970	1.40	1.118810	1.34	1.09189
40	3.0	1.36	0.920090	1.34	0.943678	1.32	0.88248
40	3.5	1.38	0.982469	1.38	1.006770	1.32	0.95941
40	4.0	1.44	1.042580	1.40	1.068630	1.38	1.03401
40	4.5	1.44	1.099870	1.42	1.124820	1.36	1.10052
50	3.5	1.40	0.887309	1.34	0.912689	1.32	0.84710
50	4.0	1.44	0.941315	1.36	0.968291	1.34	0.91446
50	4.5	1.46	0.995887	1.42	1.023100	1.36	0.98093
50	5.0	1.42	1.050850	1.42	1.076450	1.38	1.04611
50	5.5	1.46	1.100100	1.46	1.129200	1.4	1.10325
60	4.0	1.42	0.856454	1.38	0.885559	1.34	0.81452
60	4.5	1.42	0.905280	1.40	0.932540	1.34	0.87248
60	5.0	1.42	0.953985	1.42	0.983323	1.34	0.93441
60	5.5	1.46	1.004010	1.48	1.032170	1.38	0.99412
60	6.0	1.46	1.050860	1.42	1.079360	1.42	1.05058

Table 2-15: Results for parametric search on pitch distances for the maximum neutron multiplicity in infinite HCP lattice for BWR MOX spent fuels after different decay times.

Burnup [GWd/t]	Plutonium fraction [wt. %]	After 1050 years decay		After 10050 years decay		After 100050 years decay	
		P/D to maximize k_{inf}	k_{inf}	P/D to maximize k_{inf}	k_{inf}	P/D to maximize k_{inf}	k_{inf}
10	0.05	1.54	1.11865	1.56	1.17724	1.44	1.13912
10	0.06	1.62	1.15550	1.58	1.21750	1.46	1.19466
10	0.07	1.68	1.18347	1.62	1.24883	1.48	1.23333
10	0.08	1.66	1.20422	1.66	1.27146	1.50	1.26429
10	0.09	1.72	1.22136	1.64	1.29155	1.56	1.29132
10	0.10	1.76	1.23618	1.70	1.30665	1.54	1.31366
20	0.04	1.78	1.24922	1.72	1.31900	1.58	1.33056
20	0.05	1.54	1.01207	1.48	1.07691	1.42	1.03137
20	0.06	1.58	1.06439	1.58	1.13498	1.44	1.10371
20	0.07	1.62	1.10584	1.58	1.18096	1.48	1.15506
20	0.08	1.64	1.13765	1.62	1.21114	1.50	1.19636
20	0.09	1.64	1.16106	1.64	1.23691	1.52	1.22839
20	0.10	1.72	1.18143	1.70	1.25826	1.56	1.25589
30	0.04	1.74	1.19529	1.70	1.27341	1.58	1.27819
30	0.05	1.52	0.90539	1.46	0.97487	1.38	0.91993
30	0.06	1.56	0.96958	1.52	1.04426	1.40	1.00024
30	0.07	1.62	1.02160	1.56	1.09822	1.48	1.06493
30	0.08	1.70	1.06257	1.60	1.14265	1.48	1.11924
30	0.09	1.68	1.09703	1.70	1.17532	1.50	1.16079
30	0.10	1.70	1.12438	1.66	1.20473	1.52	1.19624
40	0.04	1.74	1.14446	1.68	1.22772	1.56	1.22632
40	0.05	1.48	0.81824	1.42	0.88911	1.36	0.82582
40	0.06	1.52	0.88160	1.50	0.95752	1.40	0.90467
40	0.07	1.54	0.93739	1.52	1.01767	1.42	0.97427
40	0.08	1.64	0.98518	1.60	1.06806	1.44	1.03452
40	0.09	1.64	1.02659	1.62	1.11082	1.46	1.08456
40	0.10	1.70	1.06056	1.64	1.14555	1.52	1.12695
50	0.04	1.70	1.08827	1.70	1.17303	1.52	1.16298
50	0.05	1.38	0.75399	1.38	0.82496	1.28	0.75646
50	0.06	1.46	0.80979	1.46	0.88801	1.36	0.82630
50	0.07	1.52	0.86383	1.50	0.94555	1.44	0.89282
50	0.08	1.58	0.91314	1.56	0.99826	1.44	0.95419
50	0.09	1.54	1.11865	1.58	1.04352	1.48	1.00782

50	0.10	1.62	1.15550	1.62	1.08469	1.48	1.05488
60	0.04	1.68	1.18347	1.64	1.11727	1.54	1.09764
60	0.05	1.66	1.20422	1.38	0.78185	1.30	0.70879
60	0.06	1.72	1.22136	1.42	0.83295	1.36	0.76711
60	0.07	1.76	1.23618	1.44	0.88323	1.40	0.82445
60	0.08	1.78	1.24922	1.52	0.93364	1.40	0.88082
60	0.09	1.54	1.01207	1.52	0.98021	1.46	0.93573
60	0.10	1.58	1.06439	1.62	1.02263	1.46	0.98529

Table 2-16: Results for parametric search on pitch distances for the maximum neutron multiplicity in infinite HCP lattice for PWR MOX spent fuels after different decay times.

Burnup [GWd/t]	Plutonium fraction [wt. %]	After 1050 years decay		After 10050 years decay		After 100050 years decay	
		P/D to maximize k_{inf}	k_{inf}	P/D to maximize k_{inf}	k_{inf}	P/D to maximize k_{inf}	k_{inf}
10	0.05	1.56	1.12283	1.52	1.18244	1.40	1.14848
10	0.06	1.60	1.16305	1.58	1.22715	1.48	1.20433
10	0.07	1.64	1.19200	1.62	1.25896	1.50	1.24684
10	0.08	1.68	1.21542	1.70	1.28323	1.52	1.27870
10	0.09	1.72	1.23142	1.68	1.30278	1.54	1.30542
10	0.10	1.76	1.24575	1.70	1.31698	1.58	1.32729
20	0.04	1.78	1.25717	1.72	1.32976	1.62	1.34486
20	0.05	1.60	1.02601	1.50	1.09055	1.44	1.04208
20	0.06	1.60	1.07794	1.56	1.14567	1.44	1.10754
20	0.07	1.62	1.11749	1.62	1.18616	1.48	1.16079
20	0.08	1.68	1.14583	1.62	1.21983	1.50	1.20258
20	0.09	1.76	1.16966	1.68	1.24412	1.54	1.23532
20	0.10	1.74	1.18873	1.68	1.26407	1.58	1.26077
30	0.04	1.76	1.20411	1.78	1.28062	1.56	1.28288
30	0.05	1.52	0.94996	1.48	1.01470	1.36	0.95519
30	0.06	1.60	1.00319	1.54	1.07337	1.44	1.02530
30	0.07	1.64	1.04672	1.62	1.11942	1.46	1.08200
30	0.08	1.70	1.08359	1.62	1.15793	1.52	1.12927
30	0.09	1.74	1.11116	1.64	1.18891	1.50	1.16827
30	0.10	1.72	1.13470	1.68	1.21467	1.54	1.19954
40	0.04	1.76	1.15504	1.70	1.23432	1.58	1.22651
40	0.05	1.54	0.88885	1.46	0.95390	1.38	0.88479
40	0.06	1.58	0.94155	1.52	1.01078	1.40	0.95247
40	0.07	1.64	0.98611	1.54	1.05907	1.44	1.01044

40	0.08	1.64	1.02315	1.66	1.10073	1.48	1.06146
40	0.09	1.72	1.05615	1.68	1.13457	1.52	1.10299
40	0.10	1.74	1.08368	1.68	1.16674	1.54	1.13859
50	0.04	1.74	1.10720	1.72	1.18865	1.54	1.17029
50	0.05	1.50	0.84599	1.48	0.90907	1.36	0.83233
50	0.06	1.58	0.89092	1.48	0.95971	1.40	0.89322
50	0.07	1.58	0.93466	1.54	1.00719	1.46	0.94795
50	0.08	1.64	0.97289	1.60	1.04952	1.48	0.99711
50	0.09	1.66	1.00730	1.60	1.08516	1.50	1.04338
50	0.10	1.70	1.03580	1.66	1.11598	1.50	1.08114
60	0.04	1.78	1.06131	1.70	1.14332	1.54	1.11539
60	0.05	1.46	0.81546	1.46	0.87734	1.36	0.79525
60	0.06	1.54	0.85549	1.48	0.92205	1.38	0.84715
60	0.07	1.58	0.89380	1.52	0.96362	1.44	0.89523
60	0.08	1.60	0.92853	1.60	1.00348	1.46	0.94288
60	0.09	1.68	0.96057	1.66	1.03846	1.46	0.98629
60	0.10	1.70	0.99085	1.68	1.07126	1.56	1.02664

2.4.3.3 Numerical Results for the Canister-Buffer System

By utilizing the results from the parametric search in the infinite lattice, the k_{eff} values are calculated for the canister-buffer system for different combinations of fuel types, burnup, initial enrichment/plutonium weight fraction, and decay times. The k_{eff} contour plots for UO_2 BWR, UO_2 PWR, MOX BWR, and MOX PWR spent fuels, after 10050 years decay, are shown in Figure 2-18, Figure 2-19, Figure 2-20, and Figure 2-21, respectively. The results for other decay times are shown in Figure A-26 to Figure A-33 in Appendix A. 3.

The first observation is that for all calculated UO_2 spent fuel cases, the k_{eff} values of spent fuel canisters are all far below unity. Within the present model assumptions, numerical scheme and parameter ranges (burnup, initial enrichment, and decay time), we could not construct a case to make the canister critical. Comparing BWR and PWR UO_2 spent fuels (see Figure 2-18 and Figure 2-19), the k_{eff} for the BWR canister is slightly higher than the PWR canister due to higher mass loading (see Table 2-12). Although most of the spent fuels are within the range of burnup and initial range considered in the present work, there are spent fuels with very low burnup relative to initial enrichment for various reasons, such as early fuel failure. For those special fuels, further study is necessary.

For the MOX fuel results, there are combinations of plutonium weight fractions and burnups that make the canister supercritical. The critical parameter ranges are shown in the contour plots (Figure 2-20 and Figure 2-21) for the MOX fuel cases by indicating the contour lines for $k_{eff} = 1.0$ (red lines) and 0.98 (blue lines), which could be considered as nominal criticality safety limits.

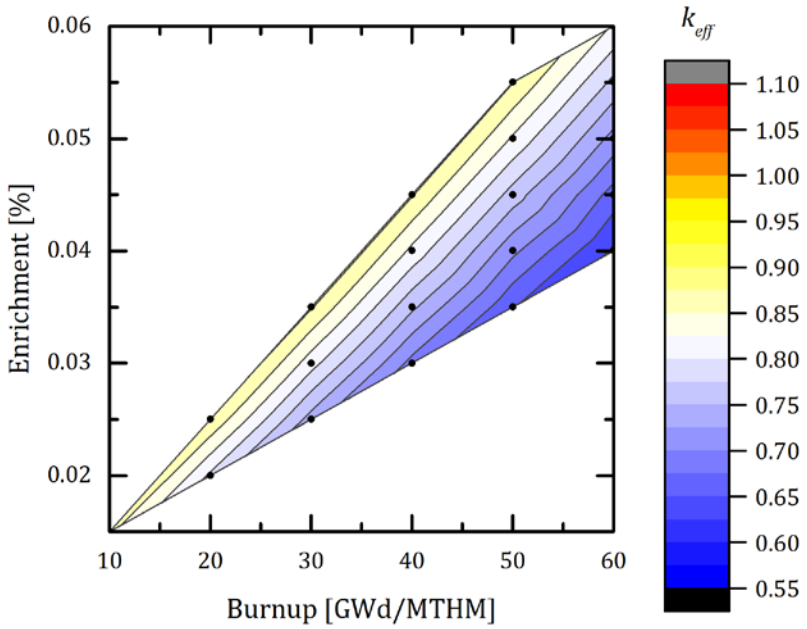

Figure 2-18: K_{eff} contour for a spent fuel canister containing BWR UO_2 spent fuel after 10050 years decay, for different combinations of spent fuel burnups and initial enrichments.

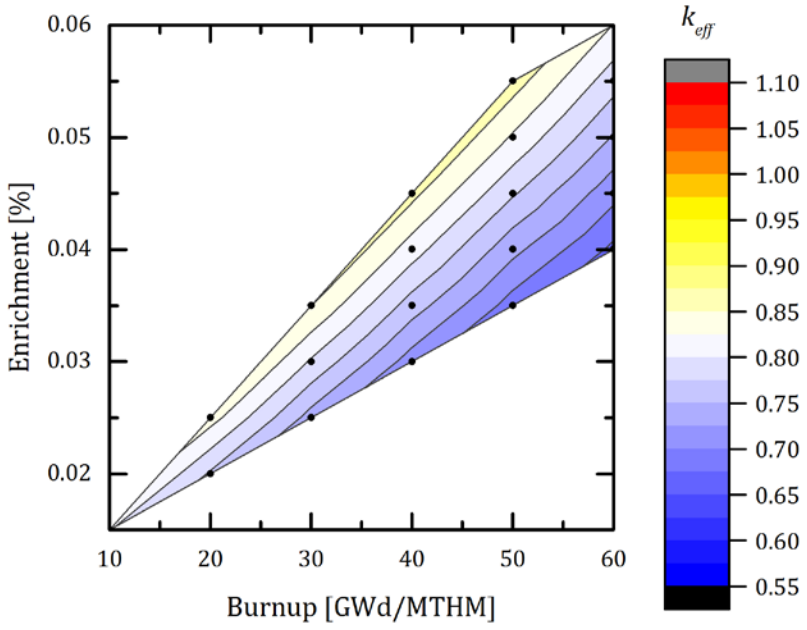

Figure 2-19: K_{eff} contour for a spent fuel canister containing PWR UO_2 spent fuel after 10050 years decay, for different combinations of spent fuel burnup and initial enrichment.

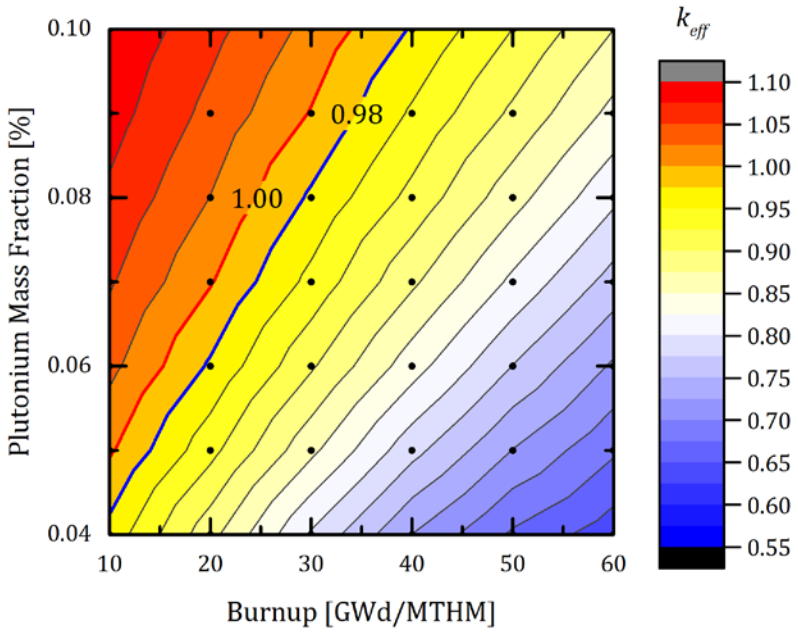

Figure 2-20: K_{eff} contour for a spent fuel canister containing BWR MOX spent fuel after 10050 years decay, for different combinations of spent fuel burnup and plutonium mass fractions.

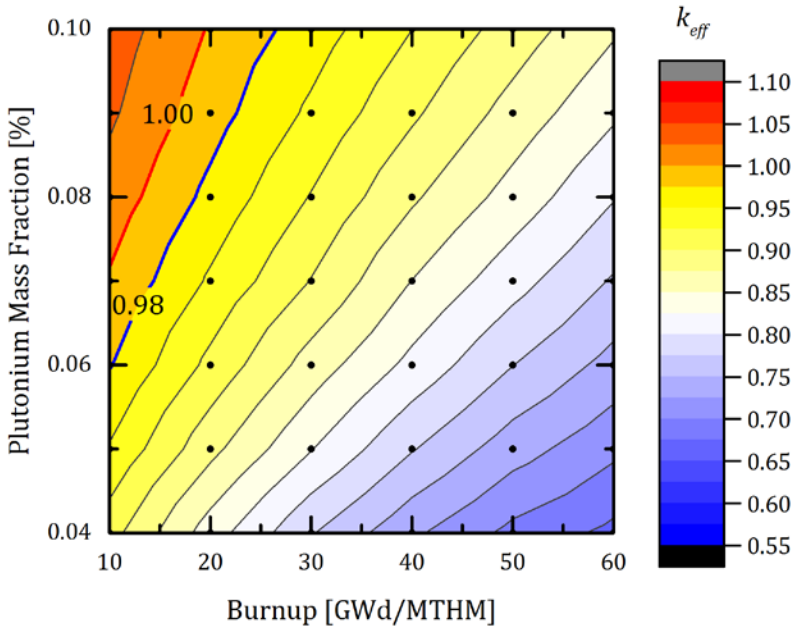

Figure 2-21: K_{eff} contour for a spent fuel canister containing PWR MOX spent fuel after 10050 years decay, for different combinations of spent fuel burnup and plutonium mass fractions.

2.5 Summary

This chapter focuses on model development and numerical results for the near-field analysis. In Section 2.2, neutronics analysis was made for a system consisting of a canister containing fuel debris from Fukushima Unit 1 reactor and the surrounding buffer, in a water-saturated deep geological repository. Based on literature review, the fuel debris has been modeled as a hexagonal lattice of spherical fuel particles. The pitch distance has been determined either by (1) making particles in contact each other or (2) letting the particles float in a lattice fully filling the canister. And during the leach time, the released materials from the damaged fuels are assumed to be either (a) removed from the system, or (b) be homogeneously mixed with the corroded canister. Combining the variations above, k_{eff} values were calculated by MCNP code for four different cases were compared at different time points for different initial canister loadings. Following key observations have been concluded from the numerical results: (a) the calculated k_{eff} is sensitively dependent on assumptions related to moderation, (b) the carbon steel canister plays an important role in reducing the potential for criticality, (c) the maximum k_{eff} of the canister-buffer system could be achieved after a fraction of fissile nuclides been released from the canister, and (d) under several assumptions, the maximum k_{eff} of the canister-buffer system could be principally determined by the dimension and composition of the canister, not by the initial fuel loading.

Based on the numerical results and findings in Section 2.2, a parametric study for the damaged fuel particles in the infinite HCP lattice has been presented in Section2.3. The compositions of the three damaged cores have been considered at five different decay times. Optimized lattice parameters for criticality have been identified and qualitatively explained. Numerical results for suggest that the system may reach highest reactivity after about ten thousand years decay. By comparing actinide compositions and thermal neutron cross-sections, the numeral results are well explained. Using the optimized lattice parameters and decay time, the critical masses of damaged fuels to be contained a single canister were calculated. If this critical mass is used as the maximum canister mass loadings, roughly a thousand canisters are needed to contain the damaged fuels from the three damaged cores.

The near-field criticality analysis for the LWR spent fuels has been presented in Section 2.4. Analysis has been made to explore under what conditions the neutron multiplicity of a spent fuel canister can be maximized, so that the uncertainty of the result can be bounded. A parametric study has been performed to examine spent fuels with different designs and burnup histories. Because the present work aims at obtaining numerical results over a broad range of input parameters including lattice parameters and different spent fuels, a new numerical scheme based on SERPENT code has been designed to reduce the computation time. A two-dimensional parametric search has firstly been made for a few representative cases of burnup and enrichment. Based on the numerical results, the parametric search has been reduced to a one-dimensional case. The numerical results indicate that, under the conditions assumed, for all UO_2 spent fuels and most of the MOX spent fuels, the single canister model will always subcritical.

Chapter 3 Far-Field Analysis: Criticality of Uranium Depositions in Geologic Formations

3.1 Introductions

This chapter focuses on model development and numerical results for the far-field analysis. Conditions for criticality of fissile depositions in geologic formations are discussed. A deep geologic repository containing damaged fuels from Fukushima reactors is considered as the source term of the fissile deposition in the far-field. The central research question is whether or not critical configurations are conceivable with fissile depositions under geological and groundwater conditions for the prospective repository. If such critical configurations are conceivable, further works need to be done to study whether or not such configurations can actually be achieved by nuclide transport analysis.

Because of the lack of actual repository-site information at the present time for the longevity of the CSA, it is crucial that the analysis is performed with well-established conservative models. In the previous studies for repository criticality safety such as[10], [18], the planar fracture model was used for representing heterogeneity of fissile deposition in geological formations. However, the conservativeness of the planar fracture model has never been investigated in detail. In this chapter, in addition to detailed analysis on mechanism and parameters that would affect neutron multiplication, the conservativeness of the planar fracture model has been investigated by comparing various geometries.

3.2 Background and Assumptions

As time elapses, Pu-239 decays to U-235 with the half-life of 24,100 years. Similarly, other trans-uranic isotopes also decay to uranium isotopes, eventually. Because combined time for canister corrosion and dissolution of damaged fuel after canister failure tends to be longer than their decay half-lives, minor-actinide isotopes (Np, Am and Cm) decay to plutonium and then to uranium isotopes while they are still in the canister. The host rock of the repository is assumed to be water-saturated.

The temperature of the uranium depositions is arbitrarily assumed to be fixed at 20 °C. In reality, however, due to decay heat and geothermal gradient, ambient temperature is likely to be elevated. To determine the temperature of the system, more detailed analyses are required for heat and mass transfer, based on site-specific information. For example, the contribution of decay heat of the radionuclides of interest is influenced by how long they remain in the system, for which sorption retardation and solubility limitation would play important roles. Also, the temperature elevation due to geothermal gradient is influenced by the site location and the depth of the uranium deposition. The primary objective of the present work is to develop a mechanistic view for how different rock types and geometries affect the neutronics, which will be crucially important information to develop Criticality Safety Assessment models for specific sites when they become known. Work required to determine the ambient temperature should and will be carried out, but out of the scope of the present work. Authors consider that the

present study with the assumption of 20 °C still provides important insights without losing the nature of the problem in a neutronics perspective, while avoiding unnecessary complexity in the discussions.

Under repository conditions, transport mechanisms of uranium and plutonium are known to be distinctively different[18], [37]. Plutonium exhibits very low solubility in groundwater and strong sorption with rock. It would adhere to colloids and be transported with groundwater motion. Either in solute or colloid-facilitated transport, most plutonium stays within short distances (< a few meters) from canisters placed in the repository[18].

Due to difference in solubility between U (VI) and U (IV), hexavalent uranium tends to dissolve in water in an oxidizing environment, such as under strong radiolytic conditions in the vicinity of a waste canister, and tetravalent uranium tend to precipitate in a reducing environment, such as in organic-rich or iron-rich rock in the far field. Compared with their critical concentrations in the aqueous phase, solubilities of uranium and plutonium are so small that criticality event could not happen with them.

250 metric tons of damaged fuel are assumed to be contained in multiple canisters, and placed in a geological repository together with other high-level wastes. To simplify, however, we do not consider in this analysis effects of other wastes co-disposed of in the same repository. Due to extremely low solubility and strong sorption with the backfill materials around the canister, and due to colloid formation, most of plutonium isotopes would stay in the vicinity of the waste canister, and decay to uranium isotopes, which dissolves in groundwater, and is transported further away into the far field.

A plume of uranium from each canister is generated by uranium originally included in the damaged fuel and by uranium generated by decay of precursors. We have conservatively assumed that uranium plumes from all damaged fuel canisters are lumped into a single uranium deposition in the far field. In the current study, neutronics analysis has been carried out for this uranium deposition in the far-field host rock.

3.3 Method and Geometries

The neutronics analyses have been performed by the Monte Carlo code MCNP[24]. Cross section libraries in ENDF/B.VII have been used for isotopes of uranium and plutonium. For compositions of rock and groundwater, natural isotopic abundance is assumed. All the k_{eff} results from MCNP calculations have standard deviation smaller than 0.002.

There are four categories of factors that affect neutronics of the system for criticality analysis: (1) geometry of the system, (2) chemical composition, density, and porosity of rock, (3) mass and isotopic compositions of uranium and plutonium, and (4) compositions and densities of chemical compounds including uranium and plutonium. The present study mainly focuses on effects of (1) and (2) on the k_{eff} and critical mass, while keeping (3) and (4) fixed. For factors (2), (3) and (4), see Section 3.5.

Uranium is assumed to deposit in its oxide form in either porous or fractured rock, such as roll-front sandstone or vein type ore in existing natural uranium deposit[38]. Because the size of the uranium deposition in porous rock[39] is of the order of the grain size of those rock, i.e., tens of microns, which is much smaller than typical neutron mean-

free-path (several centimeters), we can consider that uranium deposition in porous rock is homogeneously mixed with rock and water in an MCNP model.

For deposition in the fractured rock, two different configurations have been considered for uranium deposition and water in the fracture, as shown in Figure 3-1. The neutron shielding capability of the rock mainly depends on its chemical composition and water content. In the present numerical exploration, the thickness of infinite neutron reflector has become the largest, around 70 cm, with dry sandstone, indicating if two uranium depositions are more than 70 cm apart, they are neutronically independent each other.

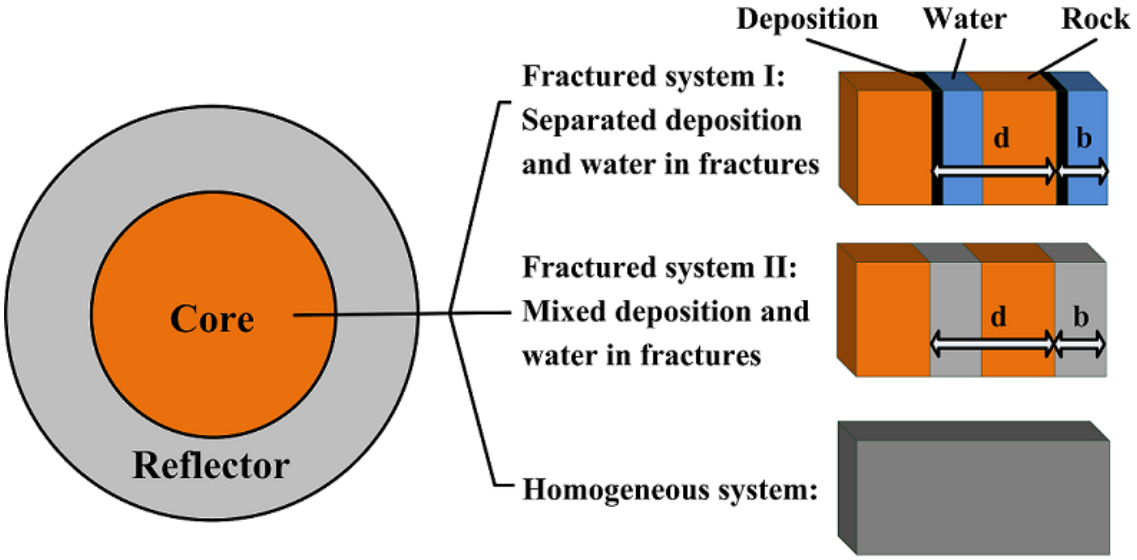

Figure 3-1: Three geometries for the MCNP simulations: (1) Fractured system I, (2) Fractured system II, and (3) Homogeneous system.

Figure 3-1 shows the schematic of the MCNP model, in which the spherical core is filled with one of the three different geometries (shown right), surrounded by the 1-meter-thick rock as reflector. The reflector is "infinitely" thick for neutrons, so that no neutron leakage could occur. Two types of heterogeneous cores and one type of the homogeneous core are considered. The heterogeneous cores consist of layered plates. In fractured geometry I, the core is filled with layers of rock (in orange), heavy metal depositions (in black), and water (in blue) alternately. The geometry of the fracture is characterized by aperture *b*, and pitch distance *d* between two adjacent fractures. The fractured system II is the same as the fractured system I, except that the heavy metal deposition layer and the water layer are homogenized into one phase. In the homogeneous system all the three materials are homogenized.

The combination of rock, water, and heavy metal is expressed by two independent variables: void volume fraction (VVF) and heavy-metal volume fraction (HMVF). For the heterogeneous systems, the VVF is given by *b*/*d*, representing the averaged fracture volume fraction, or the fracture porosity in rock. For the homogeneous system, VVF represents the void space fraction that is filled with water and heavy metal precipitations,

equivalent to the porosity of a porous rock. The HMVF is defined in a similar way, representing the volume fraction of heavy metal precipitations in the entire core. The volume fraction of the solid-phase of the rock then equals to (1-VVF), and the water volume fraction is given by (VVF-HMVF). By definition, the HMVF must be smaller than VVF, because the volume of precipitation cannot exceed the available void space in the rock.

Once the VVF and HMVF are given, the number densities of each nuclide species for MCNP calculation can be estimated by densities given in the materials input for each region. The radius of the core is determined by the total heavy metal mass and HMVF. The reflector is fixed to one meter thick, and consists of the same type of rock.

In order to perform the parametric study, an MCNP-input-file generator has been newly developed to combine the materials and geometry input parameters, and the output of ORIGEN calculations into MCNP input file. For given compositions and geometry for rock and heavy metal, calculations have been first performed for various VVF and HMVF parameters, assuming that the mass of heavy metal in the core is 250 MT. The discrete k_{eff} results have been used to generate a k_{eff} contour plot by interpolation. By defining a nominal sub-criticality criterion $k_{\text{eff}}<0.98$, the super-critical region can be determined in the parametric space. Within the super-critical parameter range, MCNP calculations have been conducted to obtain the critical mass of heavy metal deposition.

The search for the critical mass based on a given combination of rock type, geometry, VVF, and HMVF values has been carried out by calculating the k_{eff} values for different core radius values. An iterative process have to be continued, until the result match the nominal critical value ($k_{\text{eff}}=0.98$). To make find the critical mass more effectively, a semi-empirical formula was used to make "guesses" for the critical mass. In one-group diffusion theory[32], k_{eff} equals to the infinite multiplication factor k_{inf} times the non-leakage probability P_{NL}.

$$k_{eff} = k_{inf} \times P_{NL} \tag{3-1}$$

For homogeneous multiplying material in bear spherical geometry, the non-leakage probability can be expressed as,

$$P_{NL} = 1/(B_g^2 L^2 + 1), \tag{3-2}$$

$$B_g^2 = \left(\pi / \tilde{R}\right)^2,\ \tilde{R} = R + \delta, \tag{3-3}$$

where δ is the extrapolated distance, and L is the diffusion length. If we only change the core radius R and keep other parameters, the k_{inf} and L can be assumed to be constant for given set of rock type, geometry, VVF, and HMVF values. And for our scoping estimation, we simply assume the extrapolated distance constantly equals to two centimeters. Therefore, the following relation between k_{eff} and R holds approximately,

$$1/k_{eff} = A \times \left(B/\left(R + 2cm\right)^2 + 1\right) \tag{3-4}$$

Equation (3-4) is used as the semi-empirical formula to "guess" the critical core radius, in which A and B are considered constant.

The numerical scheme to determine the critical mass includes the following steps,
(1) The k_{eff} is calculated (by MCNP) on VVF and HMVF lattice for given rock type and geometry for mass of uranium=250MT,

(2) The k_{eff}<0.98 range is determined on the VVF and HMVF lattice, store the results of core radius and k_{eff} in the 0th iteration as (R_0, k_0).
(3) Make a "blind guess" in the first iteration, calculate the k_{eff} of assuming mass of uranium=25MT, store the core radius and k_{eff} as (R_1, k_1).
(4) Calculate constant A, and B in equation (3-4) by (R_0, k_0), and (R_1, k_1), store the result (A_1, B_1).
(5) Determine the core radius in 2nd iteration R_2 by solving the equation below:

$$1/0.98 = A_1 \times \left(B_1 / \left(R_2 + 2cm \right)^2 + 1 \right) \quad (3\text{-}5)$$

Then calculate k_{eff} for the 2nd iteration, store (R_2, k_2).
(6) Keep updating A, B, R until the k_{eff} converge to 0.98 (for example in the ith iteration).
(7) Calculate the critical mass by the radius R_i.

3.4 Input Data

3.4.1 Heavy Metal Compositions

The burnup calculations based on detailed Fukushima Daiichi reactor operation schedule and corrected average thermal power are given by ref. [1]. The heavy-metal compositions at the accident time are summarized in Table 3-1. Isotopes with weight fraction below 0.01% are not shown.

Table 3-1: Heavy metal compositions at the time of the accident.

Uranium Isotopes	Isotopic Weight Fraction (%)	Plutonium Isotopes	Isotopic Weight Fraction (%)
U-235	1.81	Pu-238	1.25
U-236	0.33	Pu-239	61.97
U-238	97.86	Pu-240	21.18
		Pu-241	3.93
		Pu-242	11.67
Total mass (MTHM)	248.88	Total mass (MTHM)	1.84

Table 3-2: Heavy metal compositions after 200,000 years decay.

Uranium Isotopes	Isotopic Weight Fraction (%)	Plutonium Isotopes	Isotopic Weight Fraction (%)
U-235	2.25	Pu-239	6.78
U-236	0.48	Pu-242	93.22
U-238	97.25		
Total mass (MTHM)	250.46	Total mass (MTHM)	0.054

The heavy-metal compositions after 200,000 years are tabulated in Table 3-2. These compositions have been used as the input for the MCNP calculations. In this case,

only 3.7 kg of Pu-239 remains but the enrichment of U-235 increases from 1.81% to 2.25%. The heavy metal precipitations are assumed to be UO_2 and PuO_2, with densities 10.97 g/cm^3 and 11.50 g/cm^3 [40].

3.4.2 Compositions of Rock and Groundwater

Observation at the Oklo natural reactors[41] indicates that the highest-grade uranium ore in sandstone always coexists with hematite and illite[42]. Thus, iron-rich minerals in the rock play crucial roles in both transport and neutronics aspects. Uranium precipitations are usually close to iron-rich minerals in the rock. Iron is also a strong neutron-absorber that decreases the neutron multiplicity.

Table 3-3: Host rock compositions.

Sandstone		Iron-rich rock: Magnetite-hematite-bearing pelitic gneiss	
Composition	Weight fraction (%)	Composition	Weight fraction (%)
SiO_2	78.7	SiO_2	44.09
TiO_2	0.25	TiO_2	1.69
Al_2O_3	4.8	Al_2O_3	23.64
Fe_2O_3	1.1	Fe_2O_3	12.01
FeO	0.3	FeO	3.66
MnO	0.03	MnO	0.37
MgO	1.2	MgO	2.61
CaO	5.5	CaO	0.85
Na_2O	0.45	Na_2O	2.03
K_2O	1.3	K_2O	6.01
H_2O	1.3	H_2O	3.22
P_2O_5	0.08	P_2O_5	0.15
CO_2	5.0		
Grain density (g/cm^3)	2.71	Grain density (g/cm^3)	3.09

Based on these observations, two types of host rocks (Table 3-3) are considered in the present study: average sandstone and magnetite-hematite-bearing pelitic gneiss containing 15% iron. The chemical compositions are given in ref. [43], where the crystalized water in the rock is also included. The grain densities are calculated based on the normative compositions, and the porosities of the rock are considered in the range from 0 to 30%.

Groundwater is assumed to consist of H_2O with density 1g/cm^3, and soluble neutron absorbers such as chlorine are neglected for conservatism. For each kind of rock, homogeneous and heterogeneous geometries are considered (see Figure 3-1). For the heterogeneous systems, the fracture aperture takes values of 0.1, 0.2, 0.5, 1.0, 2.0, 3.0, 4.0, 5.0, and 10.0 centimeters. In the fractured geometry, several percent of crystalized water existing in the host rock is included (see Table 3-3).

3.5 Numerical Results

3.5.1 Neutron Multiplicity

The numerical results for the effective neutron multiplication factor k_{eff} for the deposition containing 250 metric tons of uranium with the composition shown in Table 3-2 are first discussed in this section. Calculations have been made for combinations of two rock types (sandstone and iron-rich rock) as shown in Table 3-3, and three geometries as shown in Figure 3-1.

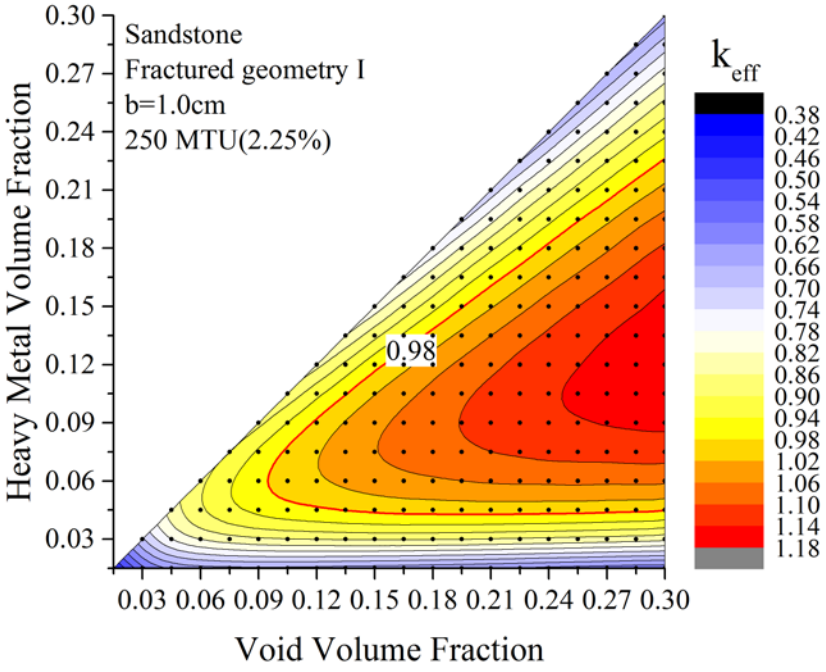

Figure 3-2: K_{eff} contour plot for fractured sandstone with fractured geometry I.

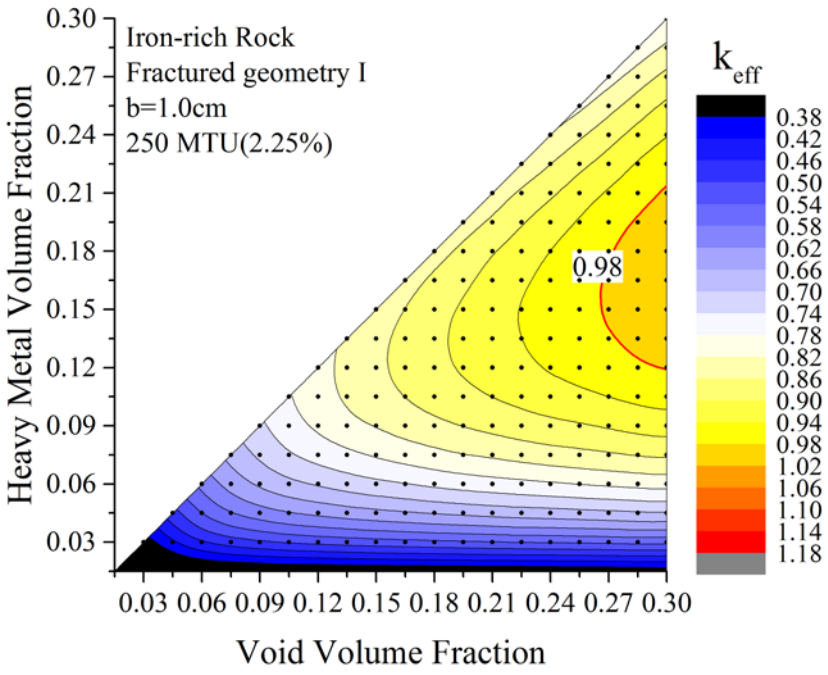

Figure 3-3: K_{eff} contour plot for iron-rich rock with fractured geometry I.

Figure 3-2 and Figure 3-3 show the contour plots of k_{eff} for fractured geometry I with b=1.0 cm for the sandstone and for the iron-rich rock, respectively. Black dots represent points at which MCNP computations have been performed. Contour lines have been drawn by interpolation among the nearest dots. The contour line in red color, referred to as the critical contour line hereafter, indicates the nominal criticality criterion, k_{eff}=0.98. The triangular region results from the fact that the HMVF cannot be greater than VVF. In either case of rock, the k_{eff} value tends to be greater for a greater value of VVF (i.e., to the right along the horizontal axis). A maximum k_{eff} is observed as HMVF increases for a fixed VVF.

These general tendencies can be explained by the amount of water in the system. Fission neutrons have greater chance to be thermalized with greater amount of water. More detailed discussions on the criticality mechanisms are given in Section 3.6. If the VVF is 0.094 or smaller for sandstone (Figure 3-2) and 0.265 for iron-rich rock (Figure 3-3), then the uranium deposition with enrichment of 2.25% in fractured geometry I is always subcritical. We call this threshold VVF as the minimum critical VVF hereafter. The comparison between sandstone and iron-rich rock shows importance of rock compositions. For the iron-rich rock, the likelihood of criticality event would be significantly smaller because iron strongly absorbs neutron.

The minimum critical VVF can be found similarly for every combination of rock type, geometry, and a certain mass of uranium deposition. The results are summarized in Figure 3-4, where the minimum critical VVF versus fracture aperture b for different rock types and geometries are plotted for 250 metric ton of uranium deposition. The solid lines represent the minimum critical VVF for sandstone and the dashed lines for the iron-rich rock, respectively. Because the homogeneous geometry has no dependence on b, the red

horizontal line shows the results. The minimum critical VVF for the combination of the iron-rich rock and homogeneous geometry is not shown in the figure, because the system remains sub-critical when VVF<0.3.

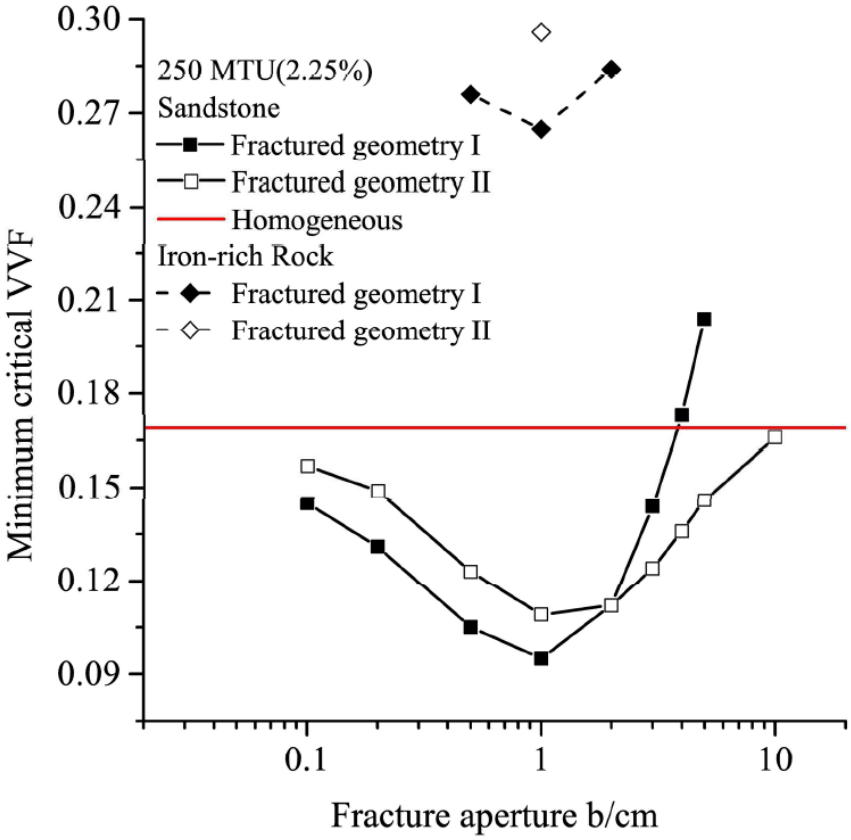

Figure 3-4: Minimum VVF for k_{eff}>0.98 for different rocks and geometries, assuming all 250 metric tons of uranium is deposited.

For both rock types with fractured I geometry, the minimum critical VVF becomes the smallest at aperture b=1.0 cm. For sandstone, in the range of b<2.0 cm, the minimum critical VVF for fractured geometry I is smaller than that for fractured geometry II. Conversely, in the range of b>2.0cm, the minimum critical VVF for fractured geometry II is smaller than that for fractured geometry I. This result indicates that heterogeneity of the uranium deposition has sensitive effects on neutron transport. Detailed discussions on effects of heterogeneity and fracture apertures are given in Section 3.6.2. For iron-rich rock, the minimum critical VVF is much greater than that for sandstone.

Similar tendencies were observed when considering the multiplication factor k_{eff} for different geometries with various fixed VVF values. For example, Figure 3-5 shows the k_{eff} as a function of fracture aperture b for the three geometries shown in Figure 3-1. For all the geometries, the VVF is fixed at 0.24, while the HMVF is chosen to optimize the multiplication. For both types of rocks, in the small-b region, the k_{eff} decreases in the order of fractured geometry I, fractured geometry II, and homogeneous geometry. Both

fractured geometries approach the homogeneous system when *b* approaches 0, because the heterogeneity of fractured systems vanishes when the fracture aperture is much smaller than thermal neutron mean free path.

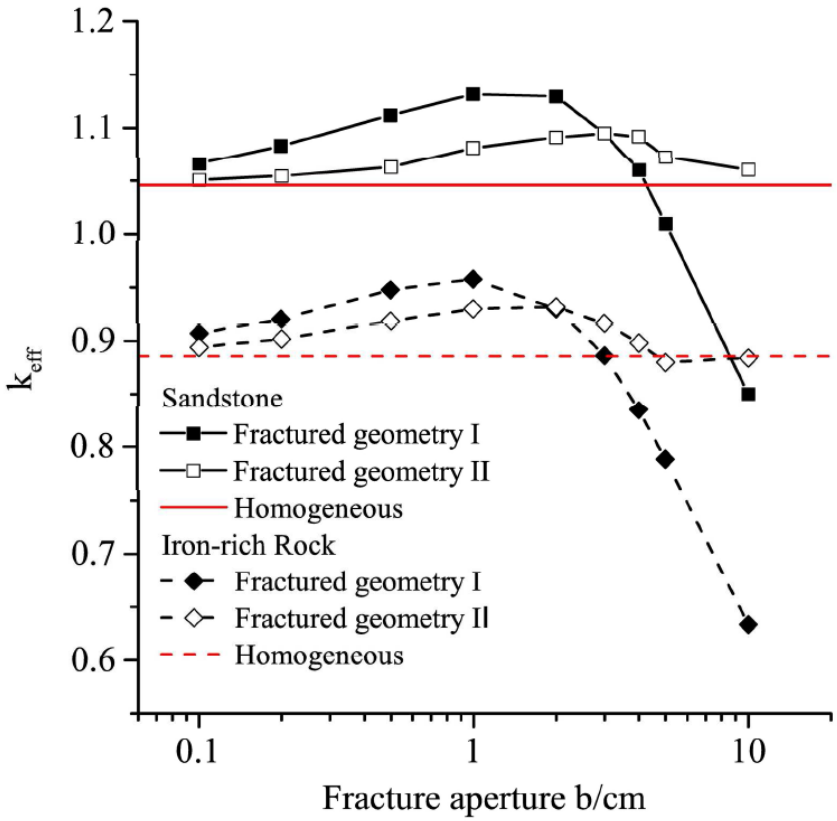

Figure 3-5: K_{eff} for different rock types and heterogeneous geometries with different fracture apertures.

The k_{eff} starts to decrease for both fractured systems when *b* is larger than several centimeters. The k_{eff} for fractured geometry I decreases much more sharply than fractured II, and eventually falls far below the homogeneous k_{eff}. Detailed discussions on this behavior at large *b* are given in Section 3.6.2.

3.5.2 Critical Mass

By reducing the mass of uranium deposit within the super-critical parameter range while fixing the geometry, the critical masses can be calculated. For fractured geometry I, the value of fracture aperture *b* is fixed at 1.0 cm as the reference value for the critical mass calculations.

Figure 3-6 and Figure 3-7 show the contour plots for the critical mass for sandstone comparing two geometries as indicated within the figures. The boundary of the plot is extracted from the red contour line from the k_{eff} results (Figure 3-2 and Figure 3-3). The values for critical masses are shown in a logarithm scale in unit of metric tons

of uranium, and the contour lines for 1, 10, and 100 metric ton are shown in black, red, and blue, respectively.

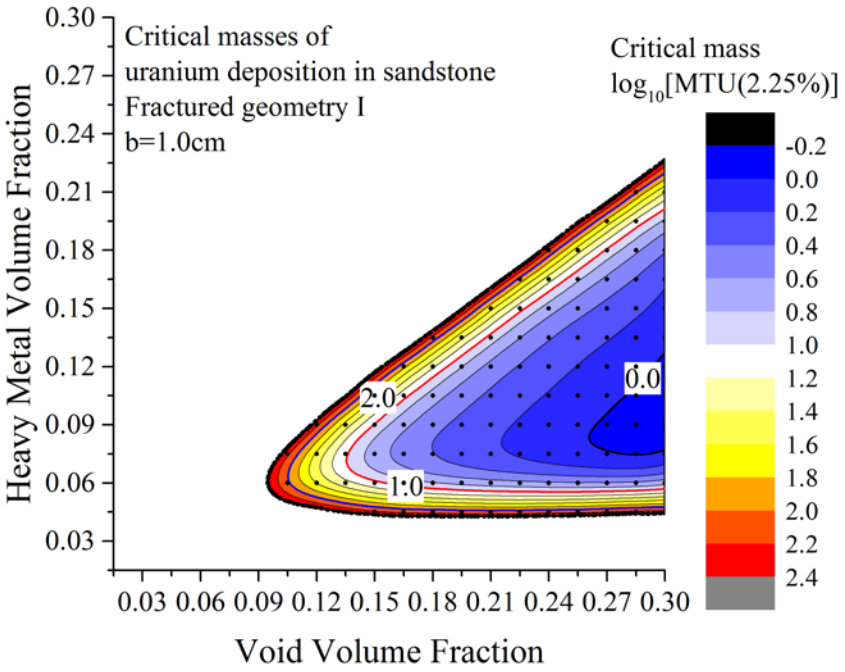

Figure 3-6: Critical mass contour plot for fractured sandstone. The values in the figure and in the side-bar scale are logarithm of metric ton of uranium included in the system.

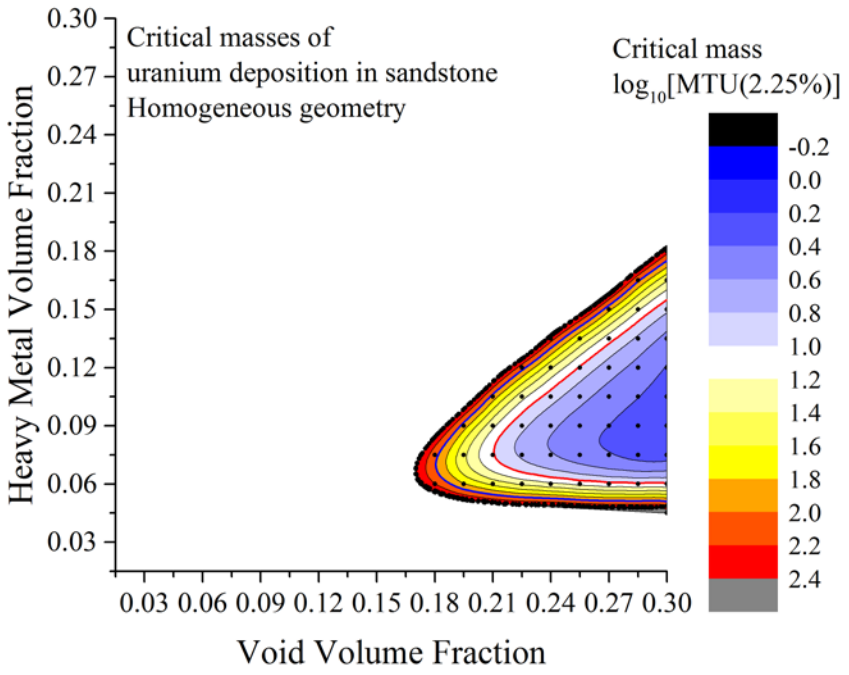

Figure 3-7: Critical mass contour plot for homogeneous sandstone. The values in the figure and in the side-bar scale are logarithm of metric ton of uranium included in the system.

It is interesting to note that more than 700 metric ton of uranium with the enrichment of about 3.7% was involved in the sustainable chain reactions in reactor zones 1-6 of Oklo uranium deposit[39]. The highest-grade uranium ore found in Oklo contains up to 15% of uranium by weight, which can be converted into the HMVF by assuming dry sandstone as 0.047[1]. With this value of HMVF, the results shown in Figure 3-7 indicate that 100 metric ton of uranium deposited homogeneously in the sandstone can become critical.

This comparison of the results in Figure 3-6 and Figure 3-7 with the Oklo phenomenon implies that uranium deposition with a mass of the order of a few hundred tons could actually exist in natural geological environment, and that a uranium deposition with the mass in the range between fractions of metric ton to a few hundred metric tons can become critical dependent on rock types, geometries, and uranium enrichment. Thus, we cannot exclude the possibility of critical configurations to occur in the far field originating from damaged fuel simply by the neutronics analysis.

In order to summarize the influence of various conditions on criticality, the minimum critical VVF for different rock types, geometries, and masses of uranium

[1] The HMVF can be calculated as following,

$$\left\{\frac{15\%\times(237.93+16\times2)\left[g\times mol^{-1}\right]}{237.93\left[g\times mol^{-1}\right]\times10.97\left[g\times cm^{-3}\right]}\right\}\Big/\left\{\frac{15\%\times(237.93+16\times2)\left[g\times mol^{-1}\right]}{237.93\left[g\times mol^{-1}\right]\times10.97\left[g\times cm^{-3}\right]}+\frac{85\%}{2.71\left[g\times cm^{-3}\right]}\right\}=0.047$$

deposition are tabulated in Table 3-4. The rock type has prominent influence on criticality due to the neutron-absorbing constituents.

Table 3-4: Minimum critical void volume fractions (VVF) for various combinations of geometries and uranium deposition masses.

Rock type	Geometry	Mass of uranium deposition (MTU)			
		250	100	10	1
		Minimum critical VVF			
Sandstone	Fractured geometry I	0.094	0.104	0.133	0.260
Sandstone	Homogeneous	0.169	0.179	0.209	>0.300
Iron-rich rock	Fractured geometry I	0.265	0.273	>0.300	>0.300

Observing each (horizontal) row individually, for any combination of rock and geometry, the minimum critical VVF decreases, as mass of uranium deposition increases, indicating that with greater mass of uranium included, the criticality is achieved in a wider range of rock porosity. Comparing different rock types with fixed geometry (fractured geometry I; see rows 1 and 3), for different uranium deposition masses, the minimum critical VVF for the iron-rich rock is always larger than the sandstone by approximately 0.17. Then, comparing different geometries for the sandstone systems (see rows 1 and 2), the minimum critical VVF for fractured geometry I for sandstone is around 0.07 smaller than that for homogeneous geometry for different masses of uranium deposition.

It is observed that the uranium mass has significant influence only in a small mass range. The decrement of minimum critical VVF is decreasing as the mass of uranium deposition is getting larger. The minimum critical VVF is decreased by 0.01 when the deposition mass is increased from 100 MT to 250MT, while the minimum critical VVF is decreased by 0.1 from the 1 MT to 10 MT. This is because with greater mass of the deposition, the neutron leakage is getting lower, which makes the system approaching an "infinite" system in terms of neutron leakage. Consequently, the k_{eff} is more determined by the composition instead of its size, which is almost equal to k_{inf}, and almost independent of the mass or size of the uranium deposition.

In summary, the systems k_{eff} increases, when (1) the rock contains fewer neutrons absorbing materials, (2) the rock has larger porosity, (3) the deposition has heterogeneous geometry, (4) the deposition contains larger amount of uranium.

3.6 Discussions

3.6.1 Influences of Uranium Mass

For a fixed VVF, there is the HMVF that gives the maximum k_{eff} because the void volume is filled with the uranium deposition and water (see Figure 3-2). For the fractured geometry I (Figure 3-1), these are expressed by the layer thickness of respective materials. With increasing the layer thickness of HMVF, the thermal neutron absorption in the uranium deposition increases, while the thermal neutron flux decreases because the

moderation decreases. These two competing effects result in the maximum HMVF for a fixed VVF. For example, for sandstone with b=1.0 cm and VVF=0.24, the maximum k_{eff} occurs at HMVF ~ 0.12, or the H/U-235 number density ratio ~ 120. Compared with the homogeneous uranium-water system, for which the optimized H/U-235 ratio is about 300 [44], it is smaller because the rock provides additional moderation.

In the k_{eff} calculations, the total mass of uranium is fixed with 250 metric ton; the radius of the core is determined in such a way that 250 metric ton of TFM is accommodated with the given value of HMVF. Therefore, the neutron leakage is also influenced by HMVF. This effect is considered less important, however, because the core radius is usually as large as several meters, and well reflected.

3.6.2 Influences of Different Geometries

The influences of different geometries can be semi-quantitatively explained by expressing the infinite multiplication factor of different systems by the four-factor formula[32],

$$k_{inf} = pf\epsilon\eta, \tag{3-6}$$

where p is the resonance escape probability, f the thermal utilization factor, ε the fast fission factor, and η the thermal reproduction factor. To simplify the discussion, the comparison is made only between fractured I and the homogeneous systems. And to adopt the convention of neutronics analysis for reactors, in the discussion hereafter, the uranium deposition is referred to as the fuel, and the water and rock are as the moderator.

Generally speaking, the resonance escape probability p of heterogeneous systems is larger than that of a homogeneous system, due to two major effects[32]. First, the separation of moderator and fuel allows some neutrons to slow down without contacting the fuel, and second, the outer layer of the fuel shields the inner layer from resonance energy neutrons, or the so-called self-shielding effect. For the fractured geometry I, the first effect is more important in the small b region. However, with increasing fracture aperture, the thickness of the fuel layer increases to keep the same HMVF. As a result, the self-shielding effect becomes more prominent.

For the heterogeneous system consisting of uranium, water, and rock, the thermal utilization factor f is given by:

$$f^{het} = \frac{\overline{\Sigma_{a,th}^{F}} V^{F} \overline{\phi_{th}^{F}}}{\overline{\Sigma_{a,th}^{F}} V^{F} \overline{\phi_{th}^{F}} + \overline{\Sigma_{a,th}^{M}} V^{M} \overline{\phi_{th}^{M}}}, \tag{3-7}$$

where $\overline{\Sigma_{a,th}^{X}}$, V^{X}, and $\overline{\phi_{th}^{X}}$ are the averaged macroscopic thermal absorption cross section, volume, and averaged thermal flux of fuel (X=F) or moderator (X=M)[32]. Recall the definition of VVF and HMVF, and define the thermal disadvantage factor as the ratio between the averaged thermal flux in the moderator and the fuel:

$$\zeta = \overline{\phi_{th}^{M}} \Big/ \overline{\phi_{th}^{F}}. \tag{3-8}$$

Then, the thermal utilization factor of a heterogeneous system can be written as:

$$f^{het} = \frac{1}{1+\left(\overline{\Sigma_{a,th}^{M}} / \overline{\Sigma_{a,th}^{F}}\right)\left(1/HMVF - 1\right)\zeta}. \tag{3-9}$$

By averaging the number densities of materials in fuel and moderator, the thermal utilization factor after the fully homogenization of the heterogeneous system can be given in a similar way:

$$f^{hom} = \frac{1}{1+\left(\overline{\Sigma_{a,th}^{M}} / \overline{\Sigma_{a,th}^{F}}\right)\left(1/HMVF - 1\right)}. \tag{3-10}$$

Again, due to the self-shielding effect, the thermal flux tends to be depressed in the highly absorbing fuel region. Thermal disadvantage factor ζ is usually greater than unity, and increases with the thickness of fuel layer due to stronger self-shielding. Comparing equations (4) with (5), the thermal utilization factor becomes greater after homogenization, and decreases with increasing *b*.

The aforementioned discussion can be further demonstrated by numerical results. The thermal disadvantage factor of the fractured geometry I for sandstone with VVF=0.24 and HMVF=0.12 has been calculated by MCNP, as shown in Figure 3-8. The result is given by the ratio between the averaged thermal fluxes tallied in the moderator layer (water + rock) and fuel layer (heavy metal depositions) that are located in at the center of the core. Because the VVF and HMVF are fixed, the thickness of uranium deposition increases proportional to the fracture aperture *b*. When *b* is greater than 2 cm, the inner part of the fuel is depleted of thermal flux due to spatial self-shielding. If the thickness of the fuel layer continues to increase, the averaged thermal flux in the fuel region will decrease rapidly. Therefore, the thermal disadvantage factor ζ increases sharply when *b* is greater than 2 cm. The contribution to the decrease of the thermal utilization factor *f* overcomes the increase of resonance escape probability *p*, corresponding to the sharp decrease of k_{eff} in Figure 3-5.

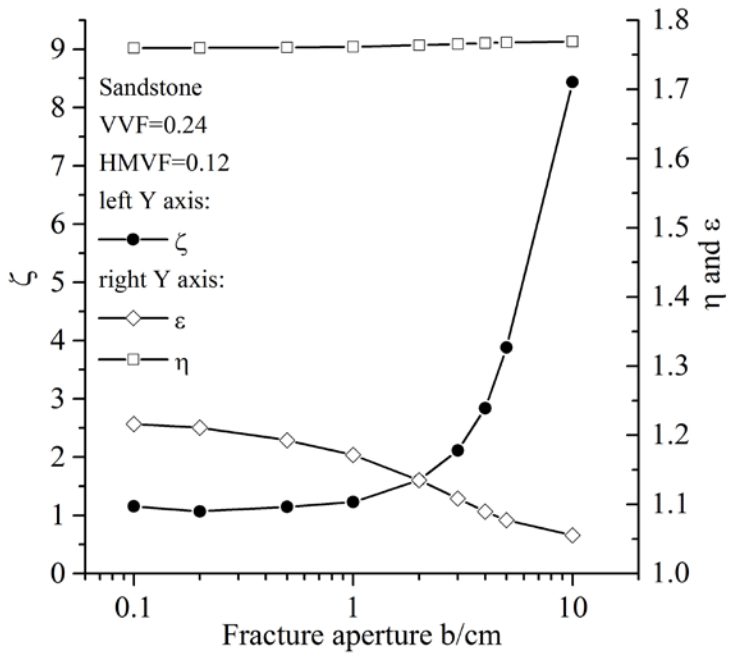

Figure 3-8: Thermal disadvantage factor, fast fission factor, and thermal reproduction factor for different fracture apertures for fractured system I.

The influences of fast fission factor ε and thermal reproduction factor η are also evaluated by MCNP calculations and shown in Figure 3-8 in a similar way. When *b* increases from 0.1 cm to 10 cm, the fast fission factor ε decreases from 1.22 to 1.06. The thermal reproduction factor η is not sensitive to the change in fracture aperture. In all calculations its value is always 1.76.

To summarize the discussions in this section, for the fractured geometry I with increasing fracture apertures, the neutron multiplication is determined by the net effect of increasing resonance escape probability *p*, decreasing thermal utilization factor *f* and decreasing fast fission factor ε. For the fractured geometry II, because the fuel and moderator are only mixed in the fracture region, the system behaves somewhere between the fractured I and homogeneous systems. Compared with fractured I, by mixing fuel and water, both resonance and thermal neutron self-shielding become weaker in fractured geometry II. The net effect is that the k_{eff} of fractured geometry II is smaller than fractured I when *b* is small, and the situation is reversed when *b* is large as shown in Figure 3-8.

3.6.3 Influences of Rock Compositions

The influence of different rock types could also be explained by equation (4). The rock with stronger neutron absorption has larger value of the denominator of equation (4), resulting in smaller f and smaller k_{eff}. Another effect is the increased ζ for large b is amplified by the term $\overline{\Sigma_{a,th}^{M}} / \overline{\Sigma_{a,th}^{F}}$. For the rock with stronger neutron absorption, the k_{eff}

decreases at smaller fracture aperture. For example, the optimized *b* for sandstone is 1 and 2 cm, but for iron-rich rock is 1 cm as shown in Figure 3-5.

3.7 Conclusions

As an analysis for the criticality safety in the far-field, works described in this chapter have been focusing on neutronic analysis to examine the criticality conditions for uranium depositions in geological formations that result from geological disposal of damaged fuels from Fukushima Daiichi reactors. MCNP models are used to evaluate the neutron multiplication factor (k_{eff}) and critical mass for various combinations of host rock and geometries. The present study has revealed that the planar fracture geometry applied in the previous criticality safety assessment for geological disposal would not necessarily yield conservative results against the homogeneous uranium deposition.

It has been found that various far-field critical configurations are conceivable for given conditions of materials and geological formations. Whether any of such critical configurations would occur in actual geological conditions remains unanswered. To answer this question, additional works need to be done in the following directions. First, from the neutronics point of view, a more "realistic" fractured system with both the fracture orientation and size randomly distributed is suggested. It is observed in the present study that the difference between the homogeneous and heterogeneous geometries could result in around 0.07 differences in the minimal critical porosity, by assuming the heterogeneous geometries are regularly fractured. However, it is still an open question whether a randomly fractured system is enveloped by the homogeneous and regularly fractured systems. Preliminary considerations on this issue are discussed in the next chapter.

Second, mass transport analysis needs to be performed to explore whether such a configuration obtained by neutronics analysis is likely to occur in geological formations. In order to make meaningful analysis along this direction of studies, however, detailed information about geological formations, geohydrology and geochemistry is required, which can only be obtained after determining a disposal site. If a repository site is given, as demonstrated for the Yucca Mountain Repository, the possibility of criticality event to happen can be thoroughly investigated, and if necessary, engineering measures to eliminate such possibility can be considered.

Third, prior to knowing the site location, it is still useful to conduct a generic mass transport analysis. With the results of the neutronics analysis, which has been performed partially in the present study, some important points for selecting a site for criticality safety can be suggested. These include: (1) iron existing in the host rock reduces the likelihood of criticality significantly; (2) low host rock porosity is preferred for criticality safety; (3) the conservatism could change when comparing heterogeneous geometries for different fracture apertures, in other words, the planar fracture geometry applied in the previous criticality safety assessment for geological disposal would not necessarily yield conservative results against the homogeneous uranium deposition because the k_{eff} for heterogeneous geometry can be smaller than that for homogeneous one in case of larger width of fracture aperture; and (4) the importance of the mass of the

deposition increases when it is smaller. To make these more reliable and specific, further studies in the neutronics and mass transport are crucially important.

Chapter 4 Preliminary Considerations on Uranium Depositions in Randomly Fractured Rocks

4.1 Introductions

Fractures in geological formations distribute randomly in locations, sizes, and orientations. To understand the criticality conditions of uranium depositions in fractured rocks, neutronics models need to be constructed based on assumptions and simplifications that properly reflect such geometrical conditions. In all previous studies[12]–[15], [18] including works presented in Chapter 3, uranium depositions in fractured rock were modeled by repeated parallel slabs surrounded by a spherical boundary. In order to reliably perform the criticality safety analysis in the far-field, we need to understand whether or not these models correctly represent the randomly fractured rock at least in the neutronics point of view.

In this chapter, the differences between the regular and random geometry in the modeling of uranium depositions in the fractured rocks are firstly discussed. The motivation, scope of the problem, and framework for discussions are then addressed. Preliminary considerations on uranium depositions in randomly fractured rocks have been demonstrated through direct sampling of randomly fractured rocks by two different numerical methods. The first approach uses the Monte-Carlo code MCNP combined with an input generator by which randomly fractured systems are sampled. The second approach utilizes an approximated analytical solution to calculate spherical fuel lumps with random locations.

4.2 Motivations and Framework

4.2.1 Motivations

From neutronics point of view, the regular fractured model (parallel slabs) might not be able to represent uranium depositions in randomly fractured rock for two major reasons.

Firstly, in fractured rocks, the fracture apertures follows lognormal or fractal distribution[45], ranging from hundreds of microns to centimeters, and only its mean value is considered in the regular geometry models. Results in Chapter 3 (see Figure 3-4) have shown that, the system's k_{eff} value sensitively depends on the fracture aperture. When we consider a system containing fractures with distributed aperture values, there is no guarantee that its k_{eff} can be correctly estimated by fixing the aperture to the mean value.

Secondly, fractures intersect each other due to the randomness of orientations. If we fix all other factors but only change the distributions of fracture orientations, the number of intersections increases when the fractures become more isotropic. In the case paralleled slabs model, the fractures are fully anisotropic and there is no intersections considered. Intersections of fractures actually affect neutron transport importantly. For example, let us consider a simple case, where two fractures intersect each other. The host rock is sandstone (defined in Table 3-3), the fractures have aperture b=2cm, filled with

homogenously mixed UO_2 and water (half water, half UO_2 by volume). The calculation is done in a cubical space (with side length of two meters), with vacuum boundary condition. And the center of the cube is the origin of the Cartesian coordinate (x, y, z) = (0, 0, 0). One fracture is parallel with the x-z plane and another is parallel with the y-z plane. Both fractures pass through the origin, and extend to the boundaries. Looking down alone z direction, the spatial distributions of the normalized on x-y plane are calculated by the "mesh tally" function in MCNP[24] for thermal (E<0.625 eV), moderate (0.625 eV<E<100 keV) and fast (100 keV<E) energy groups, corresponding to Figure 4-1, Figure 4-2, and Figure 4-3.

Clearly shown by Figure 4-1, the thermal neutron flux concentrates at the intersection of the fractures in the host rock. The flux distribution is considerably different from results given by the paralleled slabs models. Considering the spherical model with regular fractures used in Chapter 3, because the radius of the core is closely to infinite for neutrons (several meters), due to the symmetry along the paralleled fractures, the neutron flux is almost uniformly distributed in that direction. The thermalized neutrons in the host rock diffuse back to the fractures, absorbed by uranium and cause fission reactions. The thermal neutron flux in the intersection region is significantly higher than rest part of the fractures and thus the fission rate. The fission neutrons in the next generation are in the fast energy group (Figure 4-3), and again concentrate in the intersection region. The fast neutrons are then slowed down to moderate energy (Figure 4-2) by collision with rock and water, and eventually slow down to thermal energy group.

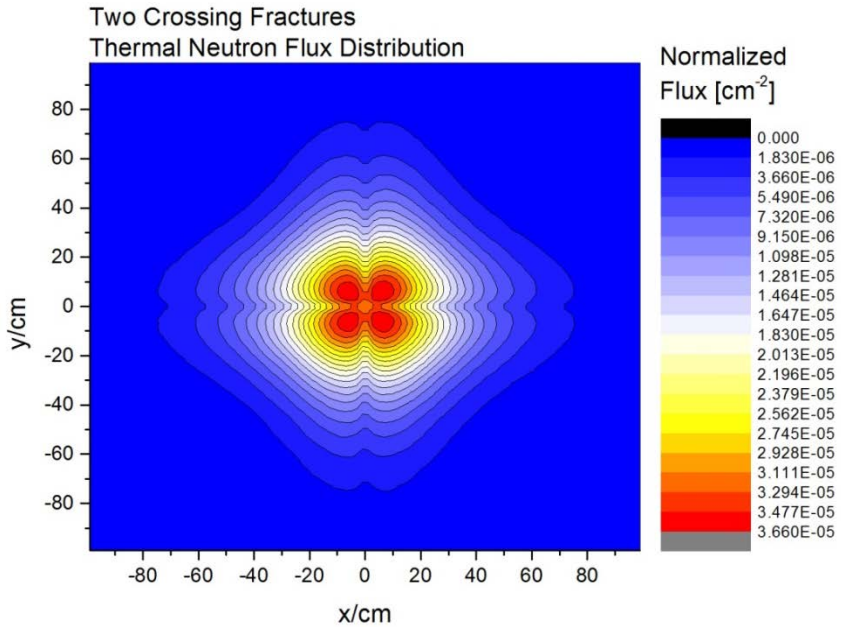

Figure 4-1: Thermal neutron flux distribution for a system consists of two intersecting fractures.

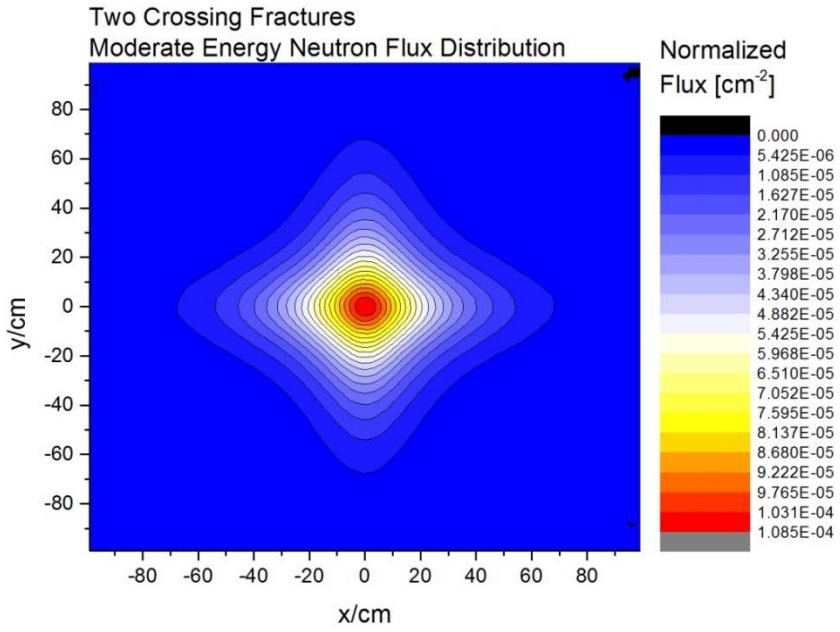

Figure 4-2: Moderate energy neutron flux distribution for a system consists of two intersecting fractures.

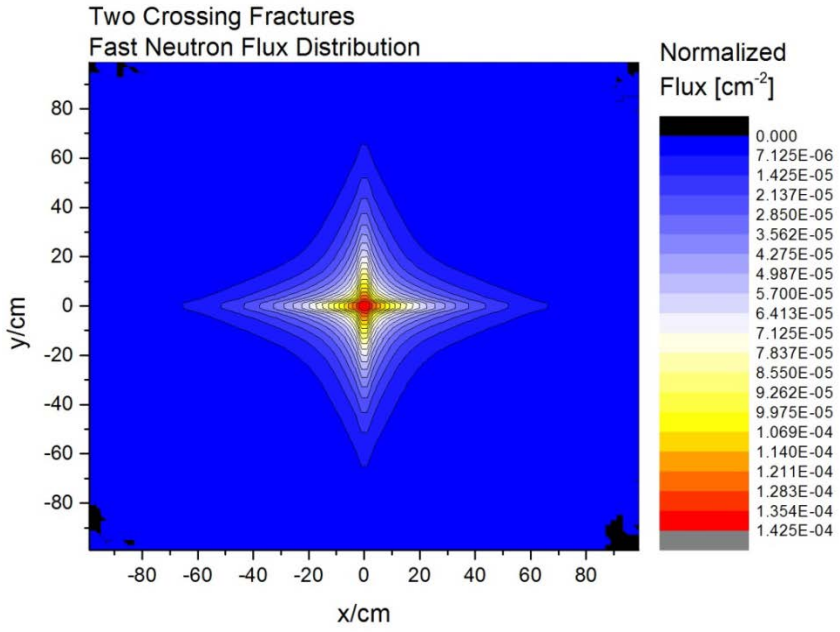

Figure 4-3: Contour plot of fast neutron flux distribution for a system consists of two intersecting fractures.

From Figure 4-3 we have found that almost all fission neutrons come from the intersection of fractures. By definition, the k_{eff} equals to the average number of neutron generation per neutron loss. It is determined statically in the Monte Carlo method by tracking neutrons from generation to loss. Therefore in criticality problems, the fission source distribution influences the k_{eff} fundamentally, since higher neutron generation

means higher statistical importance. And from that we know the fully anisotropic fractured system is fundamentally different from the isotropic fractured system, due to the difference in fission source distribution.

4.2.2 Framework of Discussions

Based on the discussions in Section 4.2.1, the criticality conditions for uranium depositions in randomly fractured rocks need to be further studied. Since no previous effort has been made to address this problem, the first step of the study is to setup the framework for future discussions and identify potential difficulties. At least the following tasks or issues need to be addressed.

(1) The randomness in the fractured rocks needs to be correctly represented. As has been mentioned in Section 4.1, randomness includes the distribution of sizes, locations and orientations. In the present work, provisional assumptions have been made to demonstrate the methodology. With more detailed work to be performed in the future, correlation of random parameters (such the fracture length and fracture aperture) should be incorporated with a reasonable data set for distributions of stochastic parameters.

(2) As has been demonstrated for the regular geometry in Chapter 3, numerical tools also need to be developed to sample randomly fractured systems and develop equivalent neutronics models. The numerical scheme and parameter space should be carefully designed, so that the calculations can be finished within a reasonable computational time.

(3) The neutron transport problem needs to be numerically solved for the sampled cases, using deterministic or Monte-Carlo methods.

(4) With given distributions of parameters such as fracture apertures, numerical results from the neutronics calculations need to be studied statistically. Through neutronics calculations, the randomness of the fractured rock propagates to the k_{eff} values. The results of criticality analysis could be interpreted in terms of probabilities with confidence intervals.

4.3 Direct Sampling of Randomly Sized and Oriented Fractures Using MCNP

A code has been developed to sample fractures with random sizes, locations, and orientations within a spherical core. The fracture is modeled as a thin box, the length of three sides are sampled independently according to lognormal distribution. Location of the center of the fracture is sampled according to a homogeneous distribution. Orientation of the fracture is assumed to be fully isotropic, and is determined by sampling in homogeneous distribution for three Euler angles. The sampled fractured system is then converted to MCNP input file. And the fissile materials and rock compositions remains the same as previously defined in

Table 3-2 and Table 3-3. Figure 4-6 shows the cross-sectional view of a system containing 25 randomly generated fractures surrounded by a spherical core. The red region indicates the fractures containing uranium dioxide and water, surround by the host rock (in blue, assumed to be sandstone here), and reflected by water saturated host rock (in yellow, sandstone with 30% porosity). Ideally speaking, the code can generate MCNP

task for unlimited number of fractures. However, practically, the computational time and memory limit the total number of fractures. The MCNP computational time increases non-linearly with increasing number of fractures. Current limit is about 150 fractures in total.

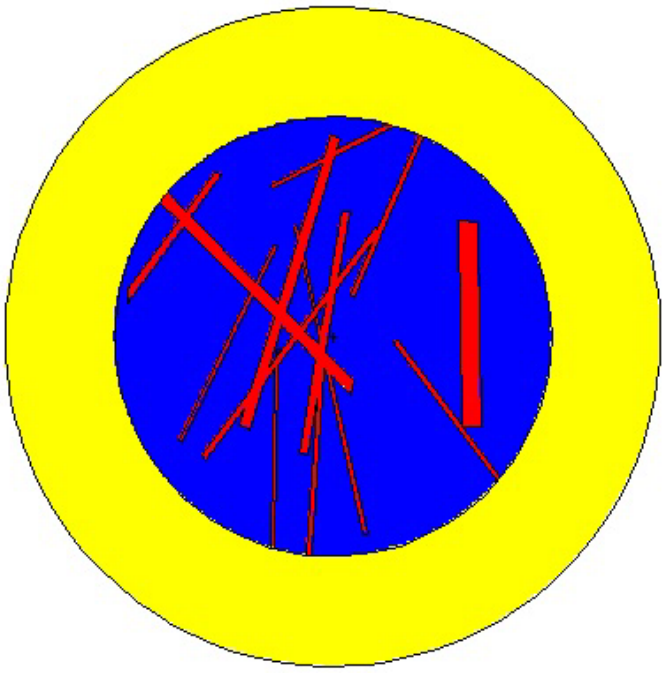

Figure 4-4: Cross-sectional view of the randomly fractured system.

4.3.1 Sampling Randomly Fractured System by Identical Unit Cells

One possible way to resolve this problem is to firstly generate random fractures in a unit cell. Then fill the core by repeating the same cell in lattice. The computation time is determined mainly by the number of surfaces in one unit cell rather than the entire system. An example using this approach is shown in Figure 9. Short coming of this method is that, the randomness of the system is artificially decreased. Also, the system cannot include any fracture larger than the cell. However, the computation time is greatly reduced, so that we can repeat the calculations for systems with large amount of fractures to study the distribution of the k_{eff} results. And the number intersection of fracture is to some extent preserved. The validity this simplification needs to be further studied. We can also optimize the size and number of the cell, to balance between the saving of computational time and representation of the reality.

Using the lattice of randomly generated cell (shown in Figure 9), 400 different realizations were sampled and converted into MCNP input files. The core has radius of 2 meter, filled with randomly generated cells, which are cubes with edge length equals to 50 centimeters. The cell contains seven randomly generated fractures. Other properties such as host rock compositions are the same as the previous example. The histogram of the k_{eff} results are shown in Figure 4-6. The distribution of the k_{eff} values is not symmetric by its mean value. Clearly, this sampling scheme using identical unit cells might not

properly represent the geometry of fractured system, a different sample scheme based on fractal distribution is discussed in the next section.

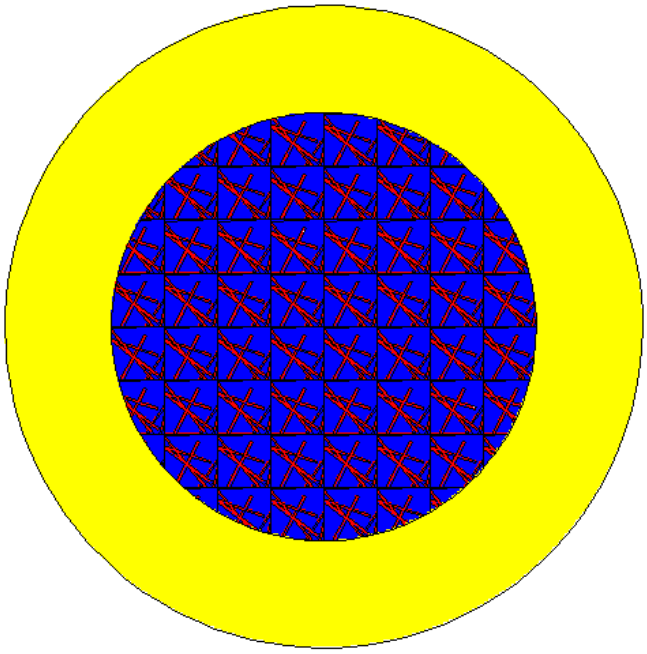

Figure 4-5: Cross-sectional view of the randomly fractured system with identical unit cells.

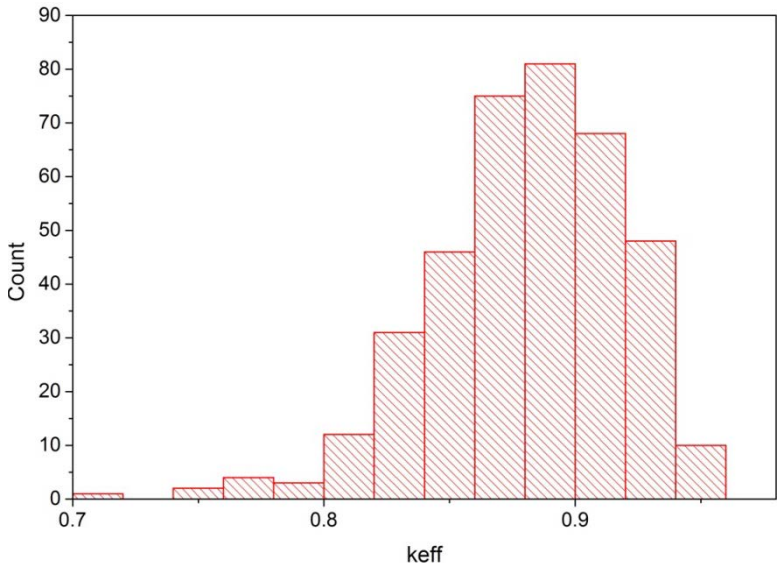

Figure 4-6: K_{eff} results for 400 randomly generated fractured systems assuming identical unit cells.

4.3.2 Sampling Randomly Fractured System using Fractal Distributions

In order to understand how the mass of uranium distributed in small and big fractures, we consider the fracture aperture follow a fractal distribution, as was suggested in ref. [45]. Assuming the probabilistic density function $f(b)$ of the fracture aperture b defined on range $B_0 < b < B_2$ and is given by,

$$f(b) = \frac{D_b}{B_0^{-D_b} - B_2^{-D_b}} \times b^{-D_b - 1}. \tag{4-1}$$

The cumulative distribution function $F(b)$ is then given by,

$$F(b) = \frac{B_0^{-D_b} - b^{-D_b}}{B_0^{-D_b} - B_2^{-D_b}}, \tag{4-2}$$

where D_b is the dimension of the system and for the fractures in rocks D_b is ranges between 1 and 2.

Divide the fractures into two groups, for $B_0 < B_1 < B_2$, $B_0 < b < B_1$ consider as small fractures, and $B_1 < b < B_2$ as big fractures. By equation(4-2), the probability of a fracture is small or big is given by, $\frac{B_0^{-D_b} - B_1^{-D_b}}{B_0^{-D_b} - B_2^{-D_b}}$ and $\frac{B_1^{-D_b} - B_2^{-D_b}}{B_0^{-D_b} - B_2^{-D_b}}$, respectively. The ratio of fracture number density in the small to same quantity for the large group equals to the ratio of probability of fractures in two groups,

$$\frac{N_{small}}{N_{big}} = \frac{B_0^{-D_b} - B_1^{-D_b}}{B_1^{-D_b} - B_2^{-D_b}}. \tag{4-3}$$

If the volume of a fracture is proportional to the third power of the aperture by a dimensionless factor α, For a system containing N fractures, the total volume of fractures in small and big fracture groups are given by,

$$V_{small} = \alpha N \int_{B_0}^{B_1} b^3 f(b)\, db = \frac{D_b}{3 - D_b} \times \frac{B_0^{3-D_b} - B_1^{3-D_b}}{B_0^{-D_b} - B_2^{-D_b}} \tag{4-4}$$

$$V_{big} = \alpha N \int_{B_1}^{B_2} b^3 f(b)\, db = \frac{D_b}{3 - D_b} \times \frac{B_2^{3-D_b} - B_1^{3-D_b}}{B_0^{-D_b} - B_2^{-D_b}} \tag{4-5}$$

And the ratio between the volumes in two groups equals to,

$$\frac{V_{small}}{V_{big}} = \frac{B_0^{3-D_b} - B_1^{3-D_b}}{B_1^{3-D_b} - B_2^{3-D_b}} \tag{4-6}$$

Assuming $B_0 = 0.1cm, B_1 = 1cm$ and $B_2 = 100cm$, and D_b=1.4, from the ratio of fracture number and volume in small and big fracture group can be calculated by equation (4-3) and equation(4-6). The results are $\frac{N_{small}}{N_{big}} = 24.16$ and $\frac{V_{small}}{V_{big}} = \frac{1}{1624.7}$.

This result indicates that, if we divide the fractures into small and big groups, most of the fractures are in the small group. However, the large fractures take almost all

the total fracture volume. For the case of uranium depositions in the fractured rock, the result suggests that, a cut-off value of the fracture aperture could be defined, so that fractures smaller than that lower bound are homogenized. In terms of volume or mass, only negligible fraction of the system is influenced due to the homogenization. However, the total number of fractures in the simulation decreases significantly. And thus reduce the computational time

For the two different sampling schemes discussed in Section 4.3.1, each realization contains a fix number of fractures, and the aperture of each fracture is sampled independently. Because the volume of the each fracture is calculated based on the fracture aperture, the total volume of fractures in the system is different for different realizations. Because we assume the fissile deposition share a constant fraction of the fracture volume, the total mass of fissile nuclides contained in the system are very different for different realizations. As a consequence, variance of the k_{eff} values shown in Figure 4-6 is very large. To reduce the variance, the following sampling scheme based on fractal distribution of fracture aperture is considered.

Consider sequence $B_0>B_1>B_2>\ldots>B_n$, defined by $B_i = B_0\alpha^i$. We sample a number of N_i fractures fixed aperture $(B_{i-1}+B_i)/2$ by random locations and orientations. (i=1, 2 … n). The N_i can be determined in the following way,

$$N_i = N \Pr\left(b \in \left[B_i, B_{i-1}\right]\right) = N \frac{\alpha^{-D_b^i}}{\sum_{k=0}^{n-1} \alpha^{-D_b^k}} \qquad (4\text{-}7)$$

where N is the total number of fractures to be sampled.

For example, suppose D_b=1.4, then set N=31, n=5, α=0.61, we can define the aperture bins so that the expected number of fracture in bins are N_1=1, N_2=2, N_3=4, N_4=8, N_5=16. From equation(4-7), it requires α^{-D_b} =2, or $\alpha = 0.6096$. If we further set the upper bound of the aperture B_5 to 5 cm, the boundary of fracture aperture bins can be calculated as, B_0= 0.421 cm,B_1= 0.690 cm, B_2= 1.132 cm, B_3= 1.857 cm, B_4= 3.047 cm. And the mid values of each bins $(B_{i-1}+B_i)/2$ (i=1,2,3,4,5) are, 0.555 cm, 0.911 cm, 1.495 cm, 2.453 cm, and 4.024 cm, respectively. We further assume the fractures length (l) and width (w) are proportional to the aperture with constant ratios (arbitrarily assumed to be 10 and 5) for all fractures, and let the largest fracture locates at the center of the model.

From the above example, with this new samplings scheme, totally 31 fractures are sampled per realization. For each realization, the fracture aperture range has been divided into 5 bins. The fractures apertures in each bin are assumed to have the same center value of the bin. And the number of fractures to be modeled equals to the expected number of fractures in the bin, which is calculated from fractal distribution. To reduce variance from fracture sizes, for different realizations, the fractures with same set of aperture, length, and width are sampled, but different locations and orientations which are randomly distributed following uniform distribution.

The randomly fractured systems described above are sampled, and numerical results are carried out by MCNP. The fractures are embedded in two different types of host rock, which are sandstone and iron-rich rock. The rock and fissile nuclides compositions are assumed to be the same as in Table 3-3. A summary of the input is

shown in Table 4-1. A hundred realizations have been sampled for each rock type. The host rock is water saturated with porosity as 0.01. Figure 4-7 shows an example of the realizations, where the deep blue part are the sampled fractures.

Table 4-1: Summary of model input for the random fracture sampling.

Fracture Aperture [cm]	Number of fractures modeled
4.024	1
2.453	2
1.495	4
0.911	8
0.555	16
Total number of fractures: 31	
Total mass of UO_2: 32.04 kg	

The k_{eff} values have been calculated by MCNP and the results for sandstone and iron-rich rock are shown in Figure 4-8 and Figure 4-9. For the sandstone the mean k_{eff} is 0.38363 and the standard deviation is 0.00734. And for the iron-rich rock the mean k_{eff} is 0.37356 and the standard deviation is 0.01033. The distribution of the k_{eff} is also asymmetric as was found in Figure 4-6. The relative standard deviation of the results is around 2%, which indicates the influence from the distribution small fractures are relative small, and the neutronics property of the system is mainly represented by the major fracture. It is also observed that compared with the iron-rich rock, the sandstone gives higher k_{eff}.

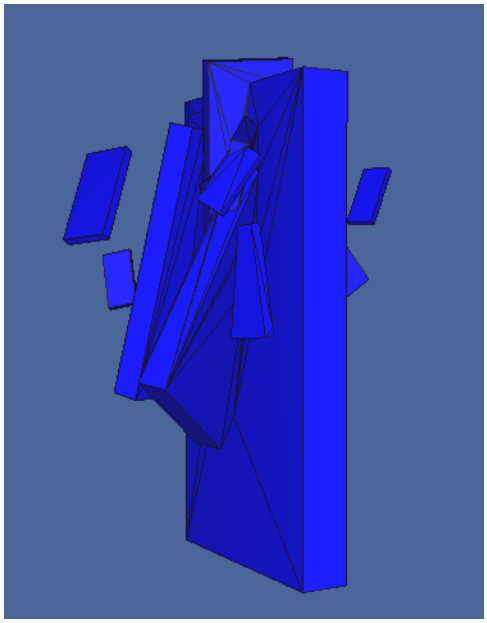

Figure 4-7: A Three-dimensional view of a sampled randomly fractured system.

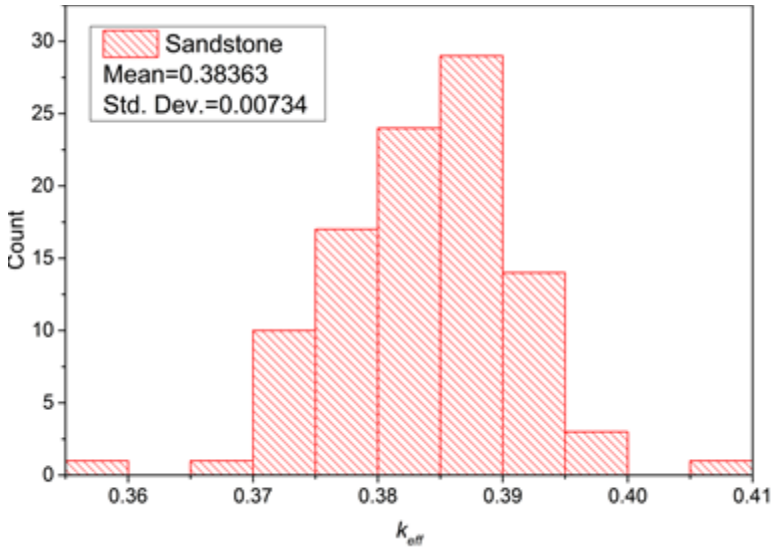

Figure 4-8: K_{eff} results for the sandstone from 100 samples.

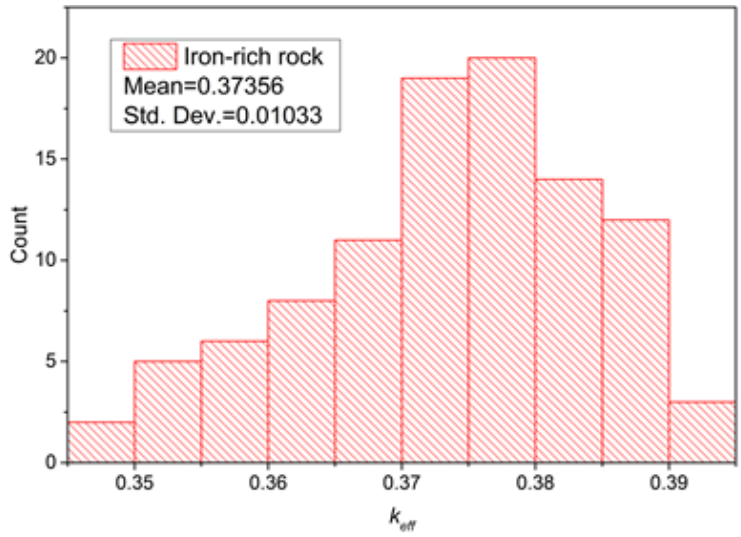

Figure 4-9: K_{eff} results for the iron-rich rock from 100 samples.

4.4 Development of an Analytical Neutronics Model for Randomly Located Fuel Lumps

In previous sections, an input generator was developed to generate randomly fractured systems for MCNP simulations. The fractal distribution has been discussed mathematically and applied numerically. Generally speaking, Monte-Carlo codes are highly accurate but very computational expensive. If Monte-Carlo codes are used, even for a very simple problem involving random geometry, it is almost impossible to generate a sample size large enough to make meaningful discussion.

To resolve this problem, a fast numerical method is needed. Due to unknowns and uncertainties in the problem, the accuracy of the method is of secondary importance. Numerical methods based on analytical solutions could provide fast, approximate results, and could be more suitable for our problem. No previous work has been made to study the effect of random geometry in the context of the long-term criticality safety in a geologic repository. Therefore, a general review of existing methods for neutron transport problems with random processes is firstly presented.

4.4.1 Literature Survey on Methods for Neutron Transport Problems with Random Processes

The study of neutron transport problems with random processes has brought a lot of research interest for almost half a century. For example, the control rod vibration problem in a light water reactor was studied in 1970s[46]. Recent efforts[47] have been made to simulate the very high temperature gas-cooled reactors (VHTR), which has fuel elements randomly located in the reactor.

In many literatures, the problem was simplified to consider only two types materials (in many cases only one contains fissile nuclides) with homogeneous properties randomly occupy a 1-D, 2-D or 3-D domain. The simplified problem was commonly stated as the neutron transport problem in binary stochastic media. In the past decade or so, efforts on this topic followed two major trends.

The first approach[25], [48]–[50] aims to explicitly calculate every sampled random system. To generate results within acceptable computational time, an approximated method based on analytical solution, namely Feinberg-Galanin-Horning (FGH) method was applied. The FGH method was firstly developed in 1950s to calculate the neutron multiplicity for system containing a few fuel elements in arbitrary locations. The method requires the fuel elements to have symmetric shape, so that they could be treated as point neutron source/sink at the center location by define a thermal constant.

The second approach[51]–[53] treats the problem in a completely different way. Instead of calculating any individual realization of the random system, the method aims to calculate the average properties of all possible systems. The method is mainly based Levermore–Pomraning (LP) equations with different modifications and improvements. The set of all possible realizations is defined as an ensemble, and the ensemble average properties based on the distributions of the two materials are described by the L-P equations.

The criticality of uranium deposition in randomly fractured rock can be formulated in similar ways. In this section, the Feinberg-Galanin-Horning (F-G-H) method has been studied. Analytical solution for a simple problem has been derived, and has been applied to generate 50000 sampled results.

4.4.2 Method and Numerical Example

Definitions and derivations of the FGH method based two-group diffusion equations have been described in Appendix B. A FORTRAN code has been developed to solve the eigenvalue problem numerically. Parallel computing was enabled using the

OpenMP framework. To demonstrate the new numerical method, we apply the method on a simple example. Consider a 3X3X3 square lattice with pitch distance of 8 centimeters. We assume there is a spherical UO_2 fuel lump randomly located with a distance less than two centimeters from each lattice point, with a uniform distribution. One of the sampled realizations is shown in Figure 4-10, where red dot represent the lattice points and black spheres represent the fuel lumps.

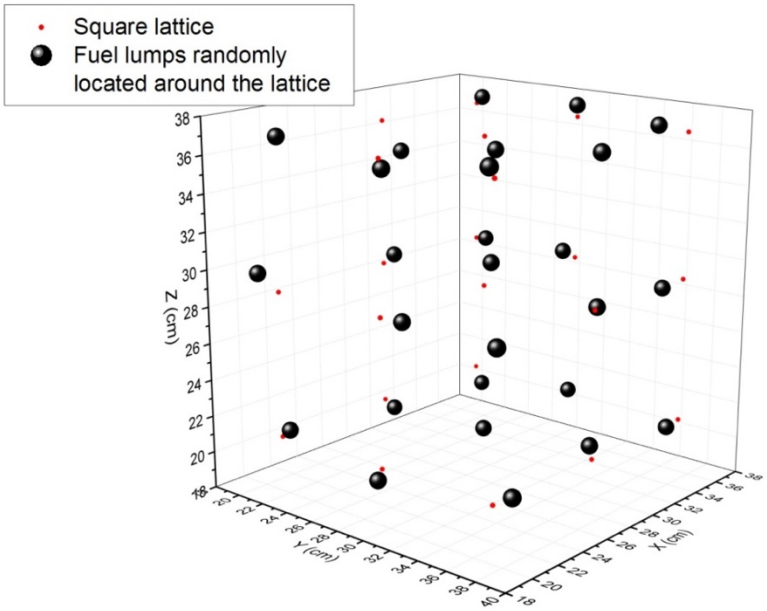

Figure 4-10: Spherical UO2 fuel lumps located lattice points of a 3X3X3 square lattice.

The fuel lumps are assumed to have 2% enrichment. The entire domain is filled with water. There is a 14-centimeter-thick layer of water surrounding the domain as reflector. In order to apply the FGH method, we need to generate the group averaged constants. We applied Monte Carlo codes to generate these constants, based on the result for the same fuel lumps in an infinite square lattice. The constants generated from the lattice (regular) geometry are used in each realization of the sampled cases using FGH method.

MCNP was the Monte Carlo code we used in previous works. However, it cannot generate neutron cross-sections between different energy groups. Therefore, a different Monte Carlo code called SERPENT was applied. We tabulated the constant calculated by SERPENT and also compared k_{inf} value calculated by MCNP and SERPENT to verify the two codes gives same results within statistical uncertainty (see Table 4-2 for comparison).

Table 4-2: Comparison between MCNP and SERPENT results.

SERPENT/MCNP comparison	
k_{inf} (SERPENT)	0.14549
k_{inf} (MCNP)	0.14594

Table 4-3: Group constants for infinite square lattice.

Group constants	Fast energy	Thermal energy
Macroscopic transport cross section Σ_t [cm^{-1}]	2.21817E-01	2.33782E+00
Macroscopic removal cross section Σ_r [cm^{-1}]	5.08963E-02	1.95076E-02
Diffusion Coefficients D [cm]	1.50278E+00	1.42583E-01
Thermal reproduction factor η	N/A	1.71470
Galanin Constant γ[cm^2]	N/A	1.18049

With the input parameters shown in Table 4-3, we can firstly compare results for 3X3X3 fuel lumps when all the fuels lumps are exactly at the lattice points. This configuration represents the average of the randomly located fuel lumps, because the average location of each fuel lump is at the lattice point by definition. For this case, the MCNP simulation gives the k_{eff} value of 0.08348 with standard deviation equal to 0.00019, FGH method gives the k_{eff} value of 0.08258, which is about 1% lower than the MCNP result. The difference is at the acceptable level.

Based on the sampling scheme previously defined, 50000 different realizations have been calculated. The results are shown in the histogram and probability plot in Figure 4-11. The sample mean of the k_{eff} value is 0.08317, which is higher than the result of the average case (k_{eff} =0.08258). It takes about 45 minutes to calculate these 50000 cases. Although less accurate, the method based on analytical solution is about four orders of magnitudes faster than the Monte-Carlo method. In Section 4.3, sample size in the order of several hundred takes days on the Berkelium cluster. This new method allows much more samples to be generated.

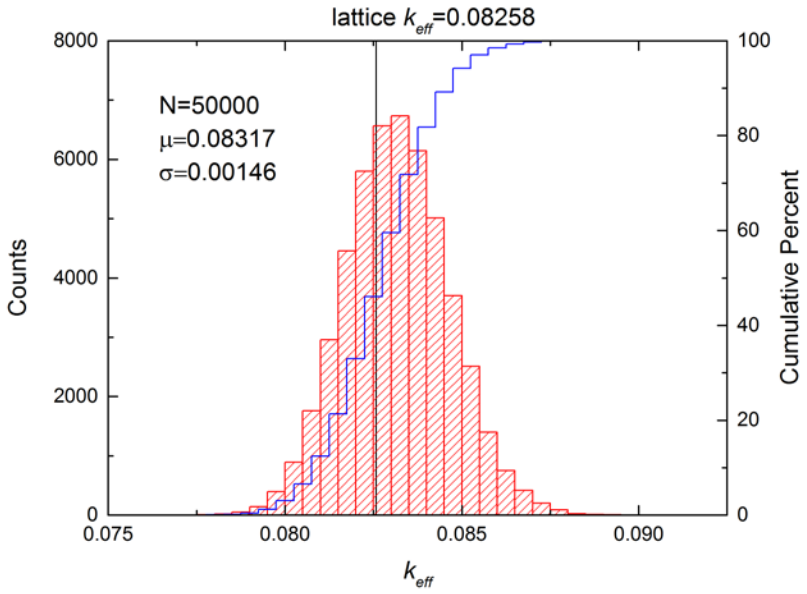

Figure 4-11: Histogram and cumulative probability of the sampled cases.

4.4.3 Discussions

Two methods were introduced in the previous literature survey section. The FGH method has been tested it in a simple numerical example. This method could be utilized in works. Before moving forward, several remarks regarding the existing methods need to be discussed.

The first thing to notice is the assumption limitation of the FGH method. The method requires some symmetric shape of fuel lumps. The fuel lumps may not be too close to each other. The sampled random system may not have too larger change in the spectrum. Generally speaking, the sampled cases should always be consistent with the conditions required by the FGH method so that the method could still be applicable.

Secondly, methods about calculating the ensemble averaged properties maybe the next step of methodology development. The L-P approach is one of those methods, which could also be derived analytically. There is also Monte-Carlo based methods[54] reported in literatures using the chord-length distribution in sampling the neutron collision events. If this ensemble averaged approach is applied, the framework of discussion the random geometry will be completely different. The expected values of k_{eff} could be directly calculated without the need of sampling. The potential limit of this approach is whether or not its assumptions can be justified in the context of uranium depositions in randomly fractured rocks. There is another possible way, to envelop the random geometry issue by considering a theoretical limit of criticality. Ref. [51] is one of these examples. Deriving the theoretical limit may seem very attractive. However, it may only be possible for very simple problem with lots of assumptions. Whether or not it can be practically useful remains an open question.

4.5 Summary

Preliminary works on uranium depositions in randomly fractured rocks have been presented in this chapter. The randomly fractured geometry could fundamentally influence the far-field criticality, because the system's k_{eff} value sensitively depends on the fracture aperture and the depositions at fracture intersections. No previous work has been made to study the effect of random geometry in the context of the long-term criticality safety in a geologic repository. The framework presented in this chapter consists of four steps: (1) Find proper mathematical or statistical description for randomness in geologic formations; (2) Sample randomly fractured system and develop equivalent neutronics model; (3) Solve the neutron transport problem for the sampled cases; and (4) Collect results from neutronics models and analyze the sampled results.

Different numerical schemes for the direct sampling of uranium depositions randomly fractured using MCNP have been developed and compared.

A general literature review of existing methods for neutron transport problems with random processes has been made. And the analytical FGH method has been derived and tested for a simple numerical example. This method will be utilized in our future works.

Chapter 5 Conclusions and Future Works

5.1 Summary of Results and Conclusions

To summarize the results and conclusions, for the near-field analysis, neutronics analysis was made for a system consisting of a canister containing fuel debris from Fukushima reactors and the surrounding buffer, in a water-saturated deep geological repository. The fuel debris has been modeled as a hexagonal lattice of spherical fuel particles. Based on the preliminary results and findings, a parametric study has been made to identify the optimized lattice parameters for criticality and to calculate the critical masses of damaged fuels to be contained a single canister. If this critical mass is used as the maximum canister mass loadings, roughly a thousand canisters are needed to contain the damaged fuels from the three damaged cores. For the LWR spent fuels, a parametric study has been performed to examine spent fuels with different designs and burnup histories. The numerical results indicate that, under the conditions assumed, for all UO_2 spent fuels and most of the MOX spent fuels, the single canister model will always subcritical.

The far-field study has been focusing on neutronic analysis to examine the criticality conditions for uranium depositions in geological formations resulting from geological disposal of damaged fuels from Fukushima Daiichi reactors. MCNP models are used to evaluate the neutron multiplication factor (k_{eff}) and critical mass for various combinations of host rock and geometries. The present study has revealed that the planar fracture geometry applied in the previous criticality safety assessment for geological disposal would not necessarily yield conservative results against the homogeneous uranium deposition. It has been found that various far-field critical configurations are conceivable for given conditions of materials and geological formations. Prior to knowing the site location, some important points for selecting a site for criticality safety can be suggested. These include: (1) iron existing in the host rock reduces the likelihood of criticality significantly; (2) low host rock porosity is preferred for criticality safety; (3) the conservatism could change when comparing heterogeneous geometries for different fracture apertures; and (4) the importance of the mass of the deposition increases when it is smaller.

As part of the improvement for the models developed in the far-field analysis, preliminary works on uranium depositions in randomly fractured rocks have been presented. The randomly fractured geometry could fundamentally influence the far-field criticality, because the system's k_{eff} value sensitively depends on the fracture aperture and the depositions at fracture intersections. No previous work has been made to study the effect of random geometry in the context of the long-term criticality safety in a geologic repository. Different numerical schemes have been developed and compared for the direct sampling of uranium depositions in randomly fractured rocks using MCNP. A general literature review of existing methods for neutron transport problems with random processes has been made. And the analytical FGH method has been derived and tested for a simple numerical example.

5.2 Recommendations for Future Works

Future works are recommended to improve the understanding of the research topic which is the long-term criticality safety for the disposal of spent nuclear fuel in geologic repository.

The criticality conditions for uranium depositions have been identified in Chapter 3. However, whether any of such critical configurations would occur in actual geological conditions remains unanswered. Mass transport analysis need to be performed to explore whether such a configuration obtained by neutronics analysis is likely to be occurred in geological formations. An overarching discussion is needed to conclude the far-field criticality study based on findings in the critical mass evaluations and nuclide migration models. Keeping track of the assumptions used in the different models consistently could be a challenging task.

In addition to the works presented in Chapter 4, future works are highly recommended to further study the uranium depositions in randomly fractured rocks. Both methodology development and applications of numerical methods are necessary.

Utilizing the far-field model developed in Chapter 3, parametric studies can be performed to with more rock types and broader parameter ranges, and to addresses the effects of fuel cycle conditions on the minimum critical masses of far-field depositions. In order to make meaningful analysis along this direction of studies, detailed information about geological formations, geohydrology and geochemistry is required, which can only be obtained after determining a disposal site. If a repository site is given, the possibility of criticality event to happen can be thoroughly investigated, and if necessary, engineering measures to eliminate such possibility can be considered.

Although criticality accidents should be prevented by the repository design, consequences of criticality events in a geological repository based on hypothetical configurations can be further discussed in future studies. Depending on the reactivity feedback mechanisms, the amount of radioactivity generated from the chain reactions and the dose released to the bio-sphere can be evaluated. The Oklo uranium deposition can be considered as a natural analog to test the models for consequence analysis.

References

[1] K. Nishihara, H. Iwamoto, and K. Suyama, “Estimation of Fuel Compositions in Fukushima-Daiichi Nuclear Power Plant,” JAEA-Data/Code 2012-018, 2012.

[2] J. Ahn, C. Carson, M. Jensen, K. Juraku, S. Nagasaki, and S. Tanaka, Eds., Reflections on the Fukushima Daiichi Nuclear Accident. Cham: Springer International Publishing, pp. 44-48, 2015.

[3] “H12: Project to Establish the Scientific and Technical Basis for HLW Disposal in Japan-Project Overview Report,” JNC, JNC-TN1410-2000-001, 2000.

[4] “Preliminary Assessment of Geological Disposal System for Spent Fuel in Japan-First Progress Report on Direct Disposal,” JAEA-Research 2015-016, 2015.

[5] “Screening Analysis of Criticality Features, Events, and Processes for License Application,” US DOE OCRWM, ANL-DS0-NU-000001 REV 00, 2008.

[6] A. J. Hicks and T. W. Rudge, “Revision of the General Criticality Safety Assessment,” Galson Science Ltd., 2007.

[7] R. M. Mason and P. N. Smith, “Modelling of Consequences of Hypothetical Criticality: Post-closure Criticality Consequence Analysis for HLW, Spent Fuel, Plutonium and HEU Disposal,” AMEC, RWM005140, 2015.

[8] “Three Mile Island Nuclear Station Unit II Defueling Completion Report,” GPU, 1990.

[9] W. J. Marshall and J. C. Wagner, “Consequences of Fuel Failure on Criticality Safety of Used Nuclear Fuel,” ORNL, ORNL/TM-2012/325, 2012.

[10] W. E. Kastenberg, P. F. Peterson, J. Ahn, J. Burch, G. Casher, P. L. Chambre, E. Greenspan, D. R. Olander, J. L. Vujic, B. Bessinger, N. G. W. Cook, F. M. Doyle, and L. B. Hilbert, “Considerations of Autocatalytic Criticality of Fissile Materials in Geologic Repositories,” *Nucl. Technol.*, vol. 115, no. 3, pp. 298–310, 1996.

[11] R. P. Rechard, L. C. Sanchez, and H. R. Trellue, “Consideration of Nuclear Criticality when Directly Disposing Highly Enriched Spent Nuclear Fuel in Unsaturated Tuff-1: Nuclear Criticality Constraints,” *Nucl. Technol.*, vol. 144, no. 2, pp. 201–221, 2003.

[12] R. B. Rechard, L. C. Sanchez, and H. R. Trellue, “Consideration of Nuclear Criticality when Directly Disposing Highly Enriched Spent Nuclear Fuel in Unsaturated Tuff-II: Geochemical Constraints,” *Nucl. Technol.*, vol. 144, no. 2, pp. 222–251, 2003.

[13] J. Ahn, “Criticality Safety Assessment for a Conceptual High-level-waste Repository in Water-saturated Geologic Media,” *Nucl. Technol.*, vol. 126, no. 3, pp. 303–318, 1999.

[14] E. Greenspan, J. Vujic, and J. Burch, “Neutronic Analysis of Critical Configurations in Geologic Repositories-I: Weapons-grade Plutonium,” *Nucl. Sci. Eng.*, vol. 127, no. 3, pp. 262–291, 1997.

[15] J. Vujic and E. Greenspan, “Neutronic Analysis of Critical Configurations in Geologic Repositories-II: Highly Enriched Uranium,” *Nucl. Sci. Eng.*, vol. 129, no. 1, pp. 1–14, 1998.

[16] R. Sanchez, W. Myers, D. Hayes, R. Kimpland, P. Jaegers, R. Paternoster, S. Rojas, R. Anderson, and W. Stratton, “Criticality Characteristics of Mixtures of Plutonium, Silicon Dioxide, Nevada Tuff, and Water,” *Nucl. Sci. Eng.*, vol. 129, no. 2, pp. 187–194, 1998.

[17] B. Kienzler, A. Loida, W. Maschek, and A. Rineiski, “Mobility and Criticality of Plutonium in a Repository,” *Nucl. Technol.*, vol. 143, no. 3, pp. 309–321, 2003.

[18] J. Ahn, “Transport of Weapons-grade Plutonium and Boron through Fractured Geologic Media,” *Nucl. Technol.*, vol. 117, no. 3, pp. 316–328, Mar. 1997.

[19] X. Liu, J. Ahn, and F. Hirano, “A Criticality Safety Study for the Disposal of Damaged Fuel Debris,” presented at the International High-Level Radioactive Waste Management Conference, Charleston, SC, USA, 2015.

[20] J. Ahn, X. Liu, and A. Salazar, “Summary Report for the FY2014 for JAEA-UCBNE Collaboration, Area 1: Criticality Safety for Geological disposal of Fukushima Damaged Fuels,” UCBNE-5147, 2015.

[21] X. Liu, A. Salazar, M. Atz, M. Fratoni, and J. Ahn, “Summary Report for the FY2014 for JAEA-UCBNE Collaboration, Area 1: Criticality Safety for Geological disposal of Fukushima Damaged Fuels,” UCBNE-5152, 2016.

[22] X. Liu, A. Salazar, M. Atz, M. Fratoni, and J. AHN, “Summary Report for the FY2015 for JAEA-UCBNE Collaboration Area 2: Preliminary Criticality Safety Assessment for Direct Disposal of Spent Nuclear Fuels,” UCBNE-5153, 2016.

[23] X. Liu, J. Ahn, and F. Hirano, “Conditions for Criticality by Uranium Deposition in Water-saturated Geological Formations,” *Journal of Nuclear Science and Technology*, vol. 52, no. 3, pp. 416–425, 2014.

[24] X-5 Monte Carlo Team, “MCNP - Version 5, Vol. I: Overview and Theory,” LA-UR-03-1987, 2003.

[25] M. M. R. Williams, “The Effect of Random Geometry on the Criticality of a Multiplying System,” *Annals of Nuclear Energy*, vol. 27, pp. 143–168, 2000.

[26] A. G. Croff, “Origen2: A Versatile Computer Code for Calculating the Nuclide Compositions and Characteristics of Nuclear Materials,” *Nuclear Technology*, vol. 62, no. 3, pp. 335–352, 1983.

[27] Mughabghab, “Thermal Neutron Capture Cross Sections Resonance Integrals and G-Factors,” IAEA, INDC (NDS)-440, 2003.

[28] McConn, R. J., Jr, Gesh, C. J., Pagh, R. T, Rucker, R. A., and Williams, R. G., III, “Compendium of Material Composition Data for Radiation Transport Modeling,” PIET-43741-TM-963, PNNL-15870, Rev1, 2011.

[29] H. Kikuchi and K. Tanai, “Basic Characteristic Test of Buffer/Backfill Materials under Horonobe Groundwater Condition,” JNC TN8430 2004-005, 2004.

[30] H. Steinhaus, *Mathematical Snapshots*, 3rd ed. edition. Mineola, N.Y: Dover Publications, 2011.

[31] H. Soneda, Y. Iwata, and M. Ebisuya, “BWR Core and Fuel Development for Highly-economical Power Generation,” *Hitachi Review*, vol. 58, no. 2, pp. 61-68, 2009.

[32] J. J. Duderstadt and L. J. Hamilton, *Nuclear Reactor Analysis*. New York: Wiley, 1976.

[33] K. Shibata, O. Iwamoto, T. Nakagawa, N. Iwamoto, A. Ichihara, S. Kunida, S. Chiba, K. Furutaka, N. Otuka, T. Ohasawa, T. Murata, H. Matsunobu, A. Zukeran, S. Kamada, and J. Katakura, “JENDL-4.0: A New Library for Nuclear Science and Engineering,” *Journal of Nuclear Science and Technology*, vol. 48, no. 1, pp. 1–30, 2011.

[34] J. LEPPÄNEN, “Serpent – a Continuous-energy Monte Carlo Reactor Physics Burnup Calculation Code, User’s Manual,” VTT Technical Research Centre of Finland, 2015.

[35] “Standard Comparison between Serpent 1.1.19 and MCNP5.”

[36] J. C. Wagner and C. E. Sanders, “Assessment of Reactivity Margins and Loading Curves for PWR Burnup-Credit Cask Designs,” NUREG/CR-6800, ORNL/TM-2002/6, 2003.

[37] B. Kienzler, P. Vejmelka, J. Roemer, D. Schild, and M. Jansson, “Actinide Migration in Fractures of Granite Host Rock: Laboratory and in Situ Investigations,” *Nucl. Technol.*, vol. 165, no. 2, pp. 223–240, 2009.

[38] “World Distribution of Uranium Deposits (UDEPO) with Uranium Deposit Classification,” IAEA-TECDOC-1629, 2009.

[39] F. Gauthierlafaye and F. Weber, “The Francevillian (Lower Proterozoic) Uranium Ore-Deposits of Gabon,” *Economic Geology*, vol. 84, no. 8, pp. 2267–2285, 1989.

[40] G. H. Aylward, T. J. V. Findlay, T. Findlay, and G. Aylward, *SI Chemical Data, 4th Edition*, 4 edition. Brisbane; Chichester: Wiley, 1999.

[41] F. Gauthier-Lafaye, P. Holliger, and P.-L. Blanc, “Natural Fission Reactors in the Franceville Basin, Gabon: a Review of the Conditions and Results of a ‘Critical Event’ in a Geologic System,” *Geochimica et Cosmochimica Acta*, vol. 60, no. 23, pp. 4831–4852, 1996.

[42] F. Gauthier-Lafaye and F. Weber, “Natural Nuclear Fission Reactors: Time Constraints for Occurrence, and Their Relation to Uranium and Manganese

Deposits and to the Evolution of the Atmosphere," *Precambrian Research*, vol. 120, no. 1–2, pp. 81–100, 2003.

[43] Angenheister G, Ed., *Numerical Data and Functional Relationships in Science and Technology: Group V Geophysics*, vol. Vol. 1A. Berlin: Springer, 1982.

[44] H. C. Paxton and N. L. Pruvost, "Critical Dimensions of Systems Containing ^{235}U, ^{239}Pu, and ^{233}U," Los Alamos National Laboratory, LA-10860-MS, 1987.

[45] J. Ahn and A. Suzuki, "Sensitivity Analysis for A High-Level Radioactive-Waste Repository with the Bounding Fracture-Transport Model," *Radioactive Waste Management and Environmental Restoration*, vol. 14, no. 4, pp. 257–273, 1990.

[46] M. M. R. Williams, *Random Processes in Nuclear Reactors*, 1st ed. Oxford, New York: Pergamon Press, 1974.

[47] C. Liang, W. Ji, and F. B. Brown, "Chord Length Sampling Method for Analyzing Stochastic Distribution of Fuel Particles in Continuous Energy Simulations," *Annals of Nuclear Energy*, vol. 53, pp. 140–146, Mar. 2013.

[48] M. M. R. Williams, "The Effect of Random Geometry on the Criticality of a Multiplying System II: Extension to Resonance Absorption," *Annals of Nuclear Energy*, vol. 27, no. 6, pp. 517–552, Apr. 2000.

[49] M. M. R. Williams, "The Effect of Random Geometry on the Criticality of a Multiplying System III: Three Dimensional Systems and Spherical Absorbers," *NSE*, vol. 141, no. 1, pp. 13–31, May 2002.

[50] M. M. R. Williams, "The Effect of Random Geometry on the Criticality of a Multiplying System IV: Transport Theory," *NSE*, vol. 143, no. 1, pp. 1–18, Jan. 2003.

[51] A. Z. Akcasu and M. M. R. Williams, "An Analytical Study of Particle Transport in Spatially Random Media in One Dimension: Mean and Variance Calculations," *NSE*, vol. 148, no. 3, pp. 403–413, 2004.

[52] J. S. Cassell and M. M. R. Williams, "An Approximate Method for Solving Radiation and Neutron Transport Problems in Spatially Stochastic Media," *Annals of Nuclear Energy*, vol. 35, no. 5, pp. 790–803, 2008.

[53] Q. Liu, H. Wu, and L. Cao, "Solution of the Multiplying Binary Stochastic Media Based on L–P equation in 1D Spherical Geometry," *Nuclear Engineering and Design*, vol. 240, no. 1, pp. 132–138, 2010.

[54] T. J. Donovan and Y. Danon, "Application of Monte Carlo Chord-Length Sampling Algorithms to Transport Through a Two-Dimensional Binary Stochastic Mixture," *NSE*, vol. 143, no. 3, pp. 226–239, 2003.

Appendix A Numerical Results for the Near-Field Criticality Study

A. 1 Parametric Study for the Damaged Fuels from Fukushima Unit2 and Unit 3 in Infinite HCP Lattice

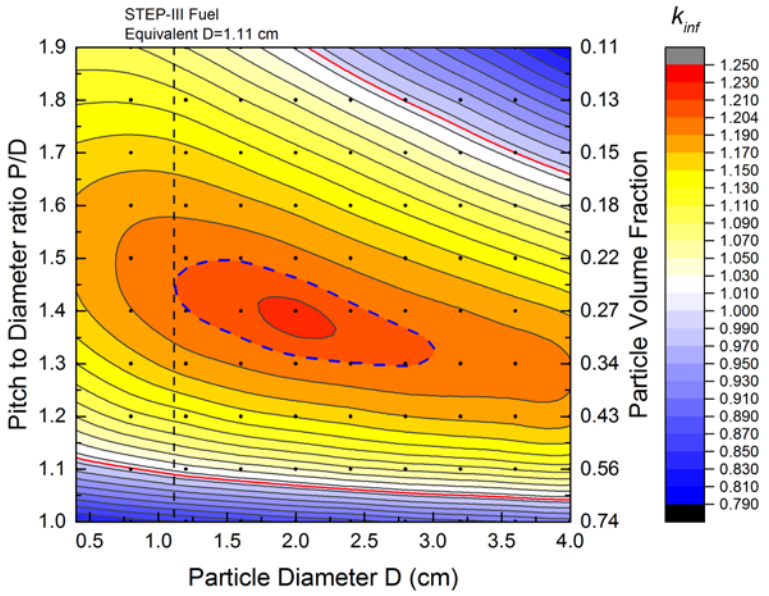

Figure A-1:K_{inf} contour plot for the damaged fuels from Fukushima Unit 2 in infinite HCP lattice, after 50 years decay.

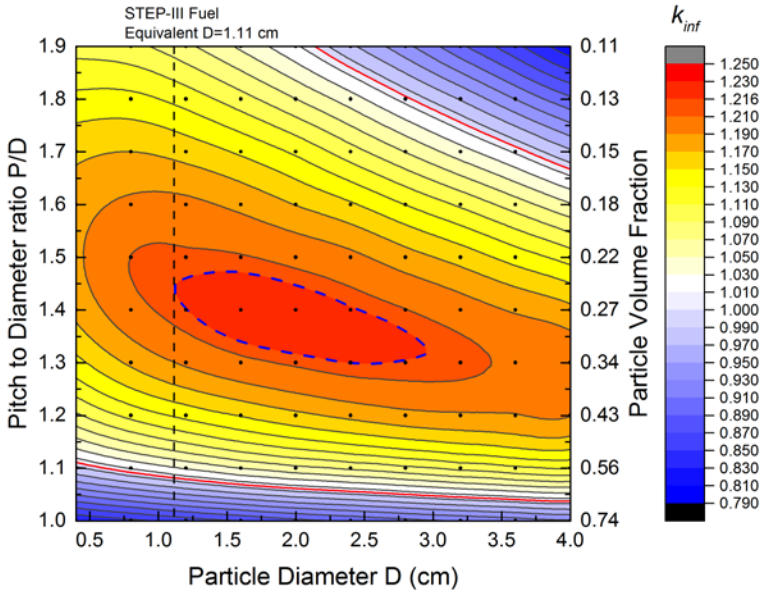

Figure A-2: K_{inf} contour plot for the damaged fuels from Fukushima Unit 2 in infinite HCP lattice, after 1050 years decay.

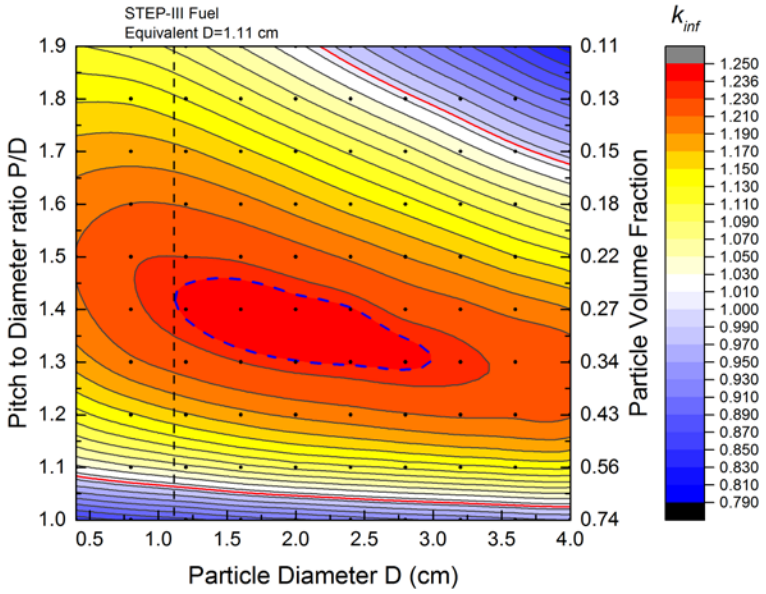

Figure A-3: K_{inf} contour plot for the damaged fuels from Fukushima Unit 2 in infinite HCP lattice, after 1050 years decay.

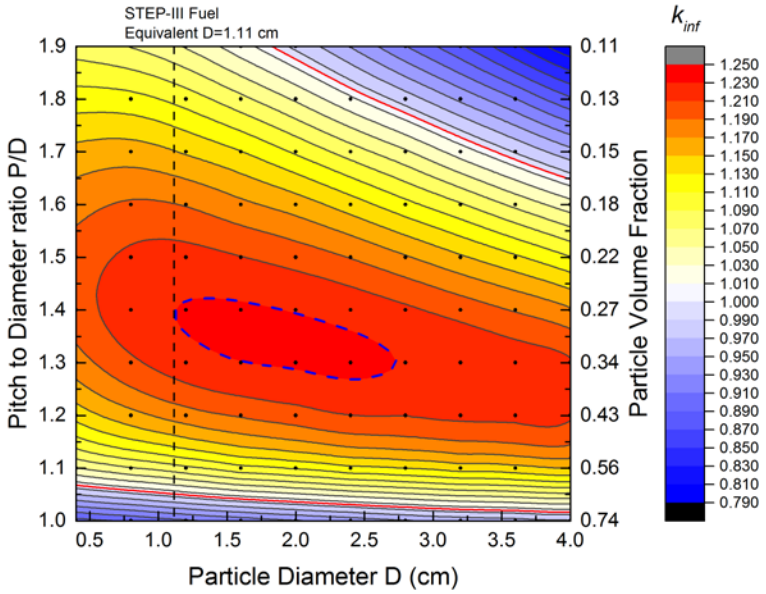

Figure A-4: K_{inf} contour plot for the damaged fuels from Fukushima Unit 2 in infinite HCP lattice, after 1050 years decay.

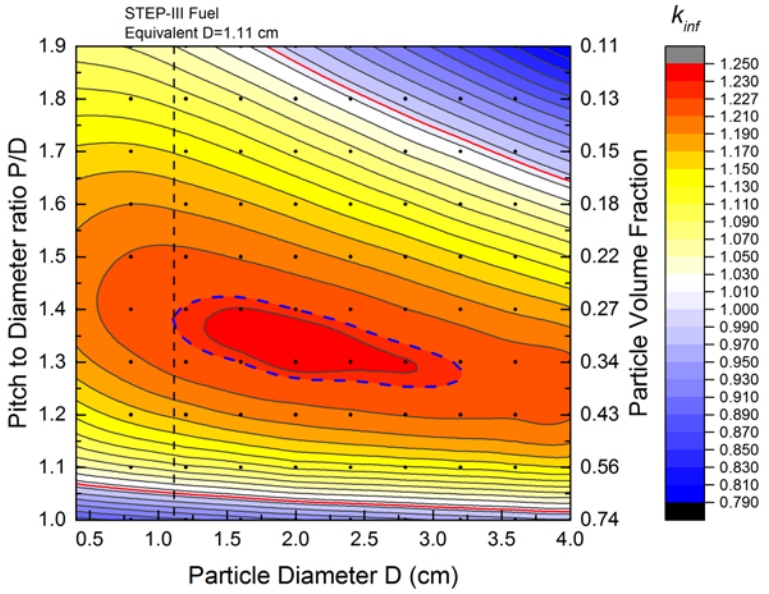

Figure A-5: K_{inf} contour plot for the damaged fuels from Fukushima Unit 2 in infinite HCP lattice, after 10050 years decay.

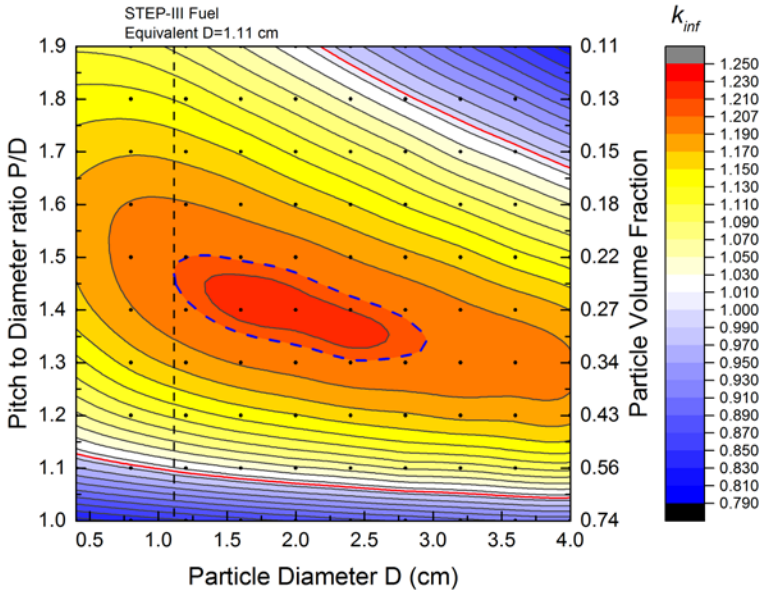

Figure A-6: K_{inf} contour plot for the damaged fuels from Fukushima Unit 3 in infinite HCP lattice, after 50 years decay.

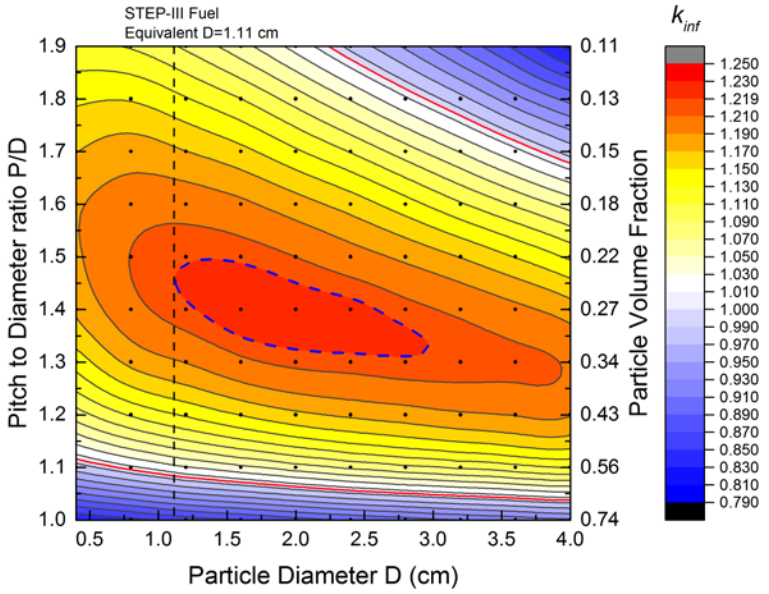

Figure A-7: K_{inf} contour plot for the damaged fuels from Fukushima Unit 3 in infinite HCP lattice, after 1050 years decay.

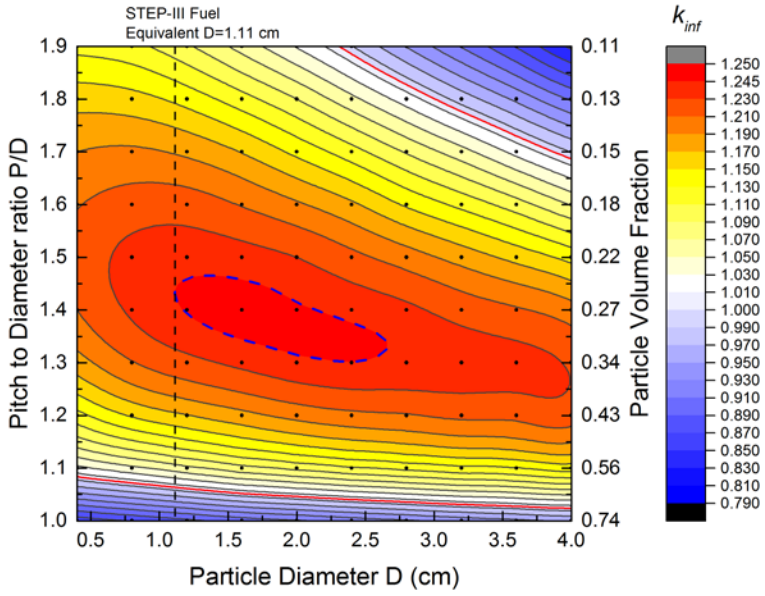

Figure A-8: K_{inf} contour plot for the damaged fuels from Fukushima Unit 3 in infinite HCP lattice, after 10050 years decay.

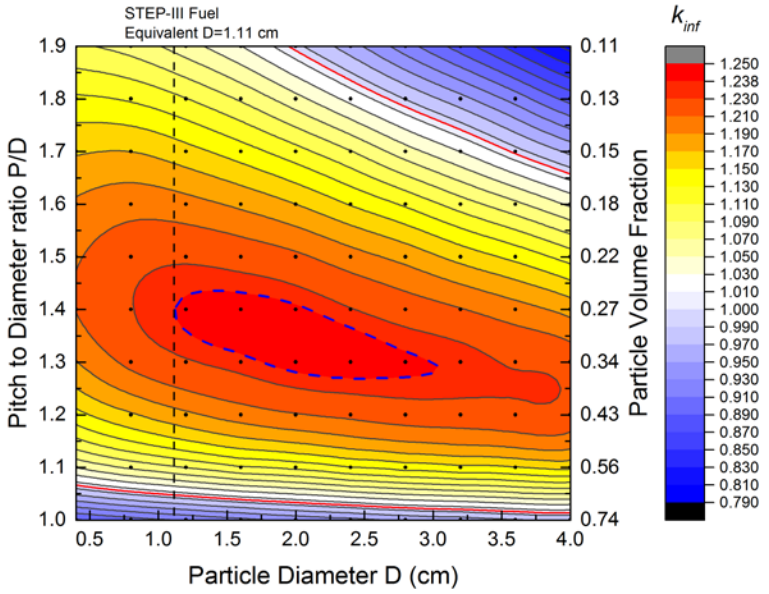

Figure A-9: K_{inf} contour plot for the damaged fuels from Fukushima Unit 3 in infinite HCP lattice, after 100050 years decay.

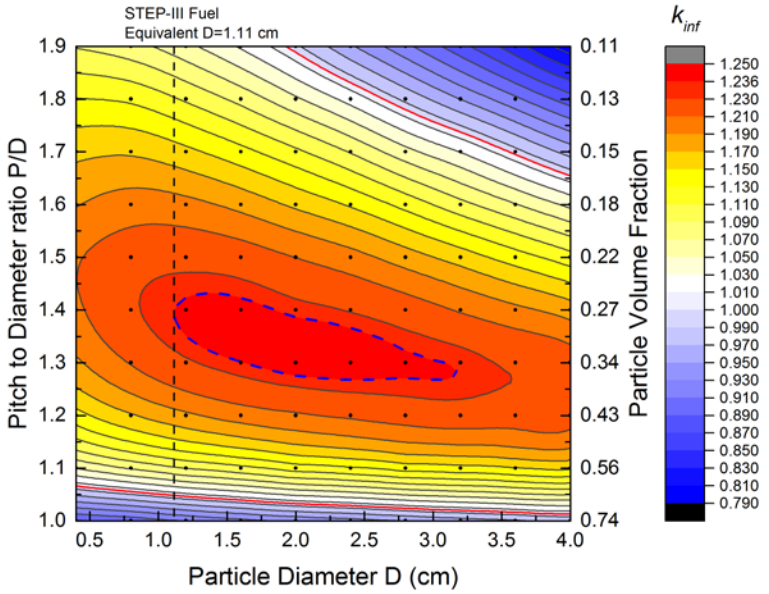

Figure A-10: K_{inf} contour plot for the damaged fuels from Fukushima Unit 3 in infinite HCP lattice, after 200050 years decay.

A. 2 Parametric Study for BWR and PWR Spent Fuels in Infinite HCP Lattice

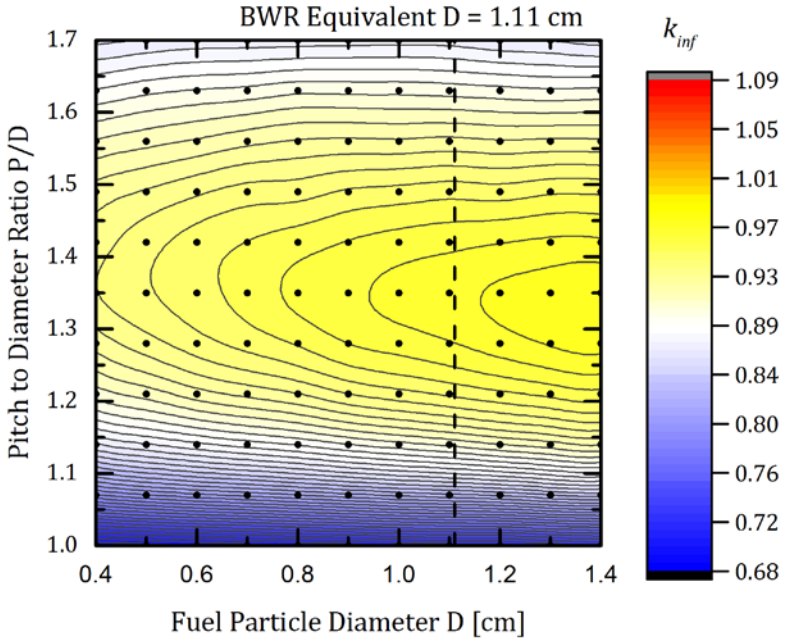

Figure A-11: K_{inf} contour plot for BWR UO_2 spent fuel in infinite HCP lattice, after 1050 years decay. The spent fuel has burnup of 20 GWd/t and initial enrichment of 2.0%.

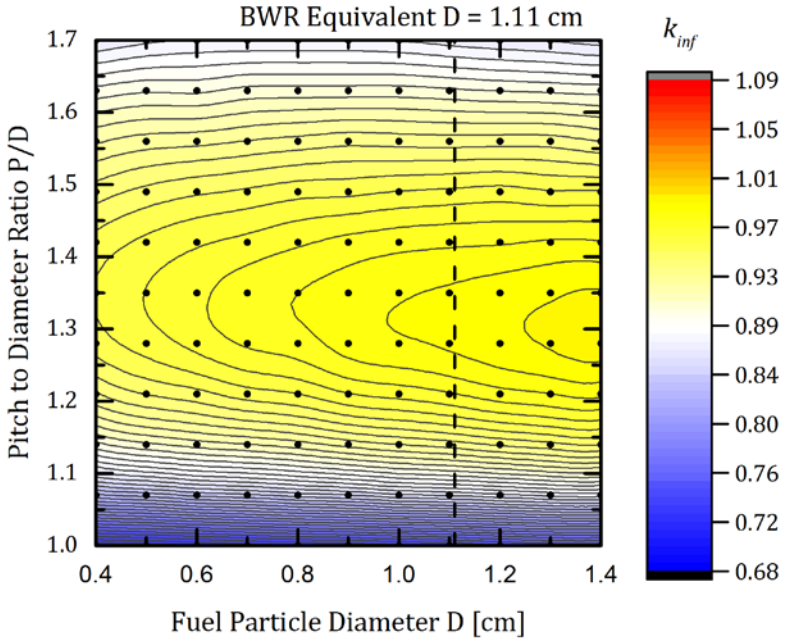

Figure A-12: K_{inf} contour plot for BWR UO_2 spent fuel in infinite HCP lattice, after 10050 years decay. The spent fuel has burnup of 20 GWd/t and initial enrichment of 2.0%.

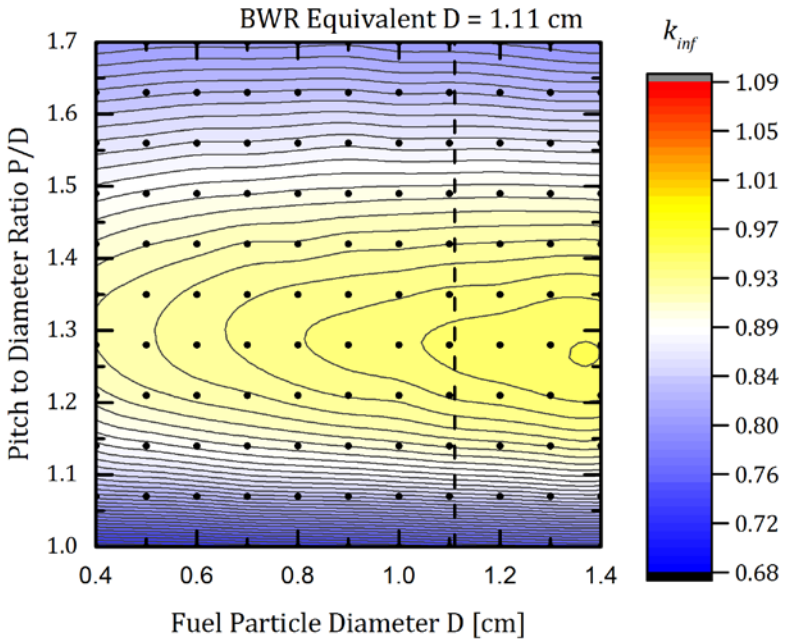

Figure A-13: K_{inf} contour plot for BWR UO_2 spent fuel in infinite HCP lattice, after 100050 years decay. The spent fuel has burnup of 20 GWd/t and initial enrichment of 2.0%.

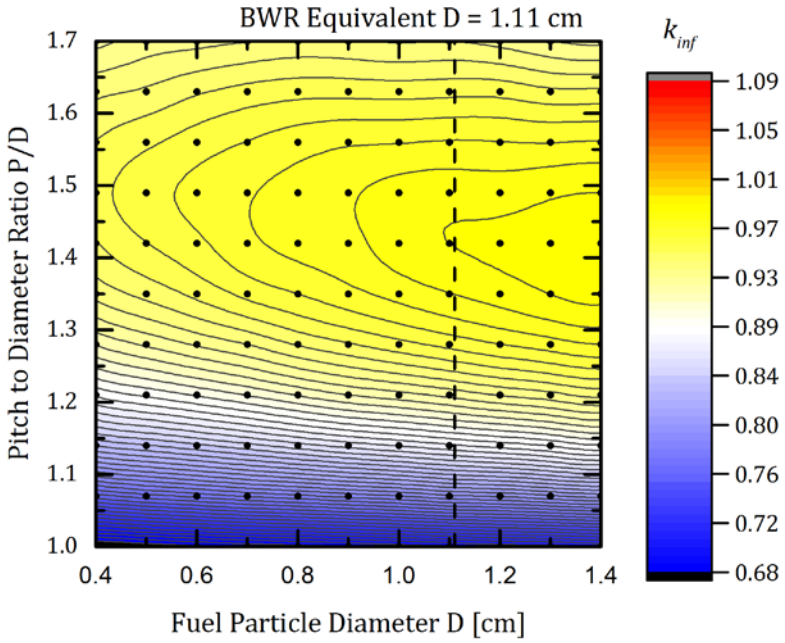

Figure A-14: K_{inf} contour plot for BWR UO_2 spent fuel in infinite HCP lattice, after 1050 years decay. The spent fuel has burnup of 60 GWd/t and initial enrichment of 6.0%.

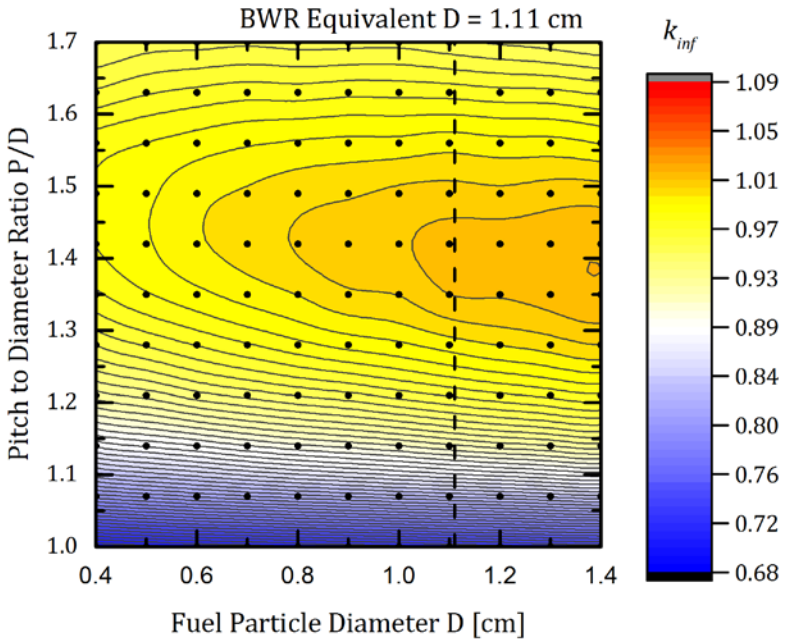

Figure A-15: K_{inf} contour plot for BWR UO_2 spent fuel in infinite HCP lattice, after 10050 years decay. The spent fuel has burnup of 60 GWd/t and initial enrichment of 6.0%.

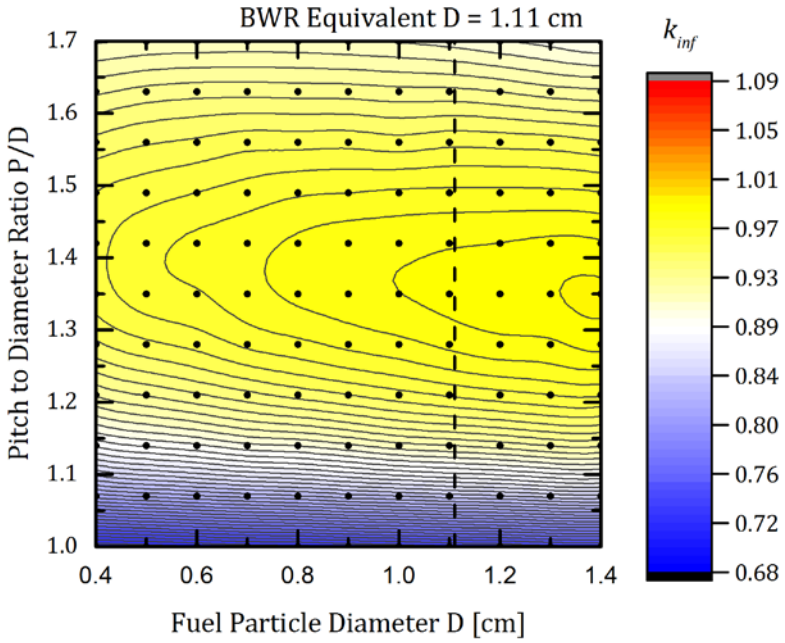

Figure A-16: K_{inf} contour plot for BWR UO_2 spent fuel in infinite HCP lattice, after 100050 years decay. The spent fuel has burnup of 60 GWd/t and initial enrichment of 6.0%.

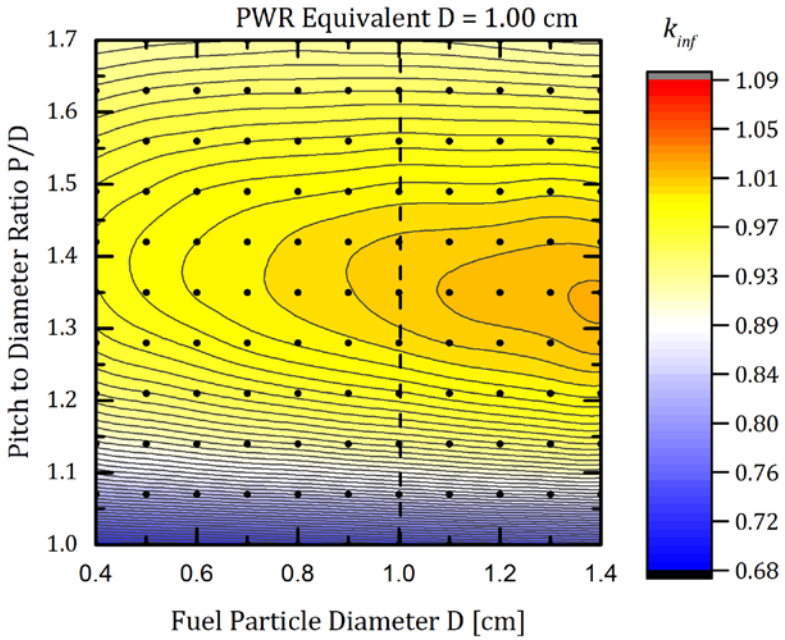

Figure A-17: K_{inf} contour plot for PWR UO_2 spent fuel in infinite HCP lattice, after 1050 years decay. The spent fuel has burnup of 20 GWd/t and initial enrichment of 2.0%.

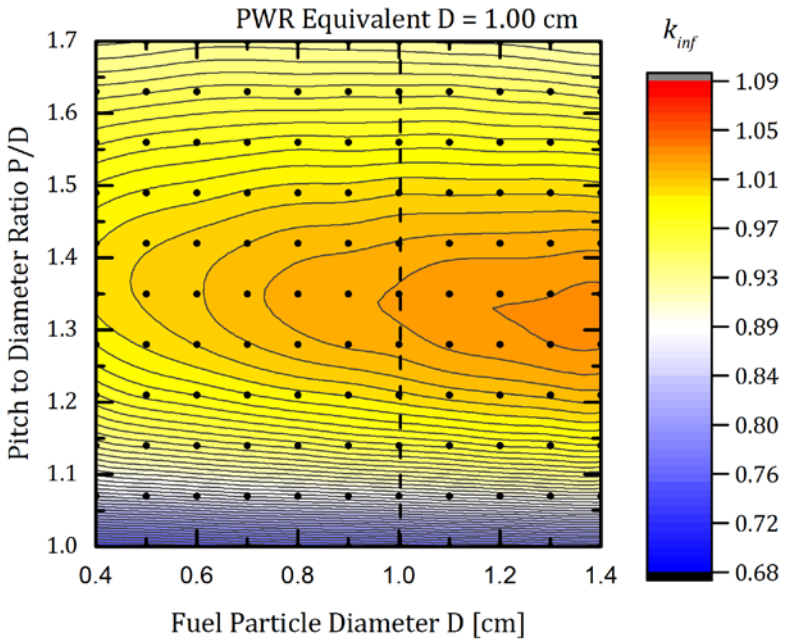

Figure A-18: K_{inf} contour plot for PWR UO_2 spent fuel in infinite HCP lattice, after 10050 years decay. The spent fuel has burnup of 20 GWd/t and initial enrichment of 2.0%.

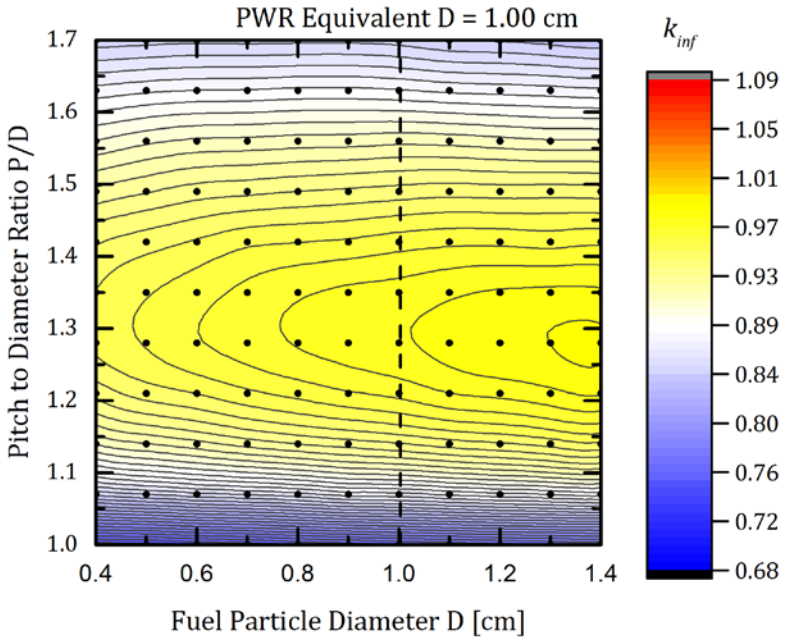

Figure A-19: K_{inf} contour plot for PWR UO_2 spent fuel in infinite HCP lattice, after 100050 years decay. The spent fuel has burnup of 20 GWd/t and initial enrichment of 2.0%.

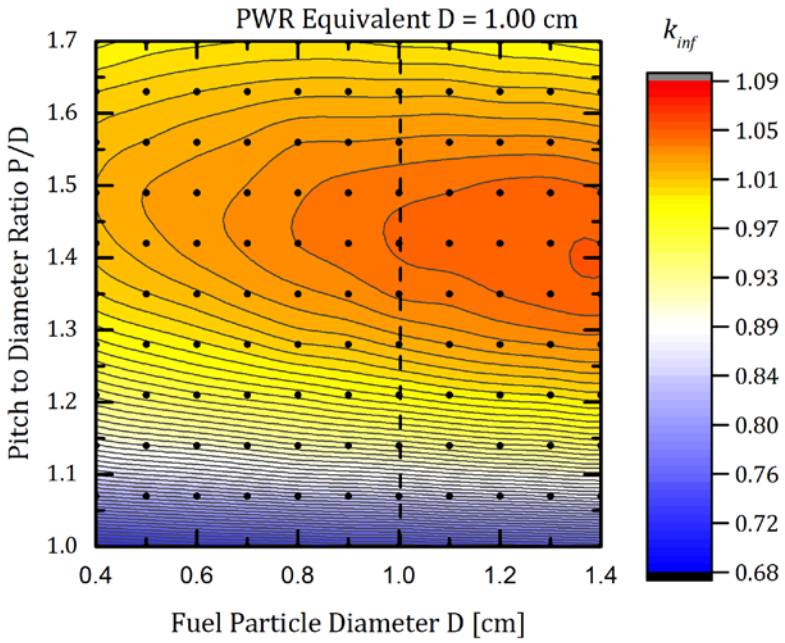

Figure A-20: K_{inf} contour plot for PWR UO_2 spent fuel in infinite HCP lattice, after 1050 years decay. The spent fuel has burnup of 40 GWd/t and initial enrichment of 4.0%.

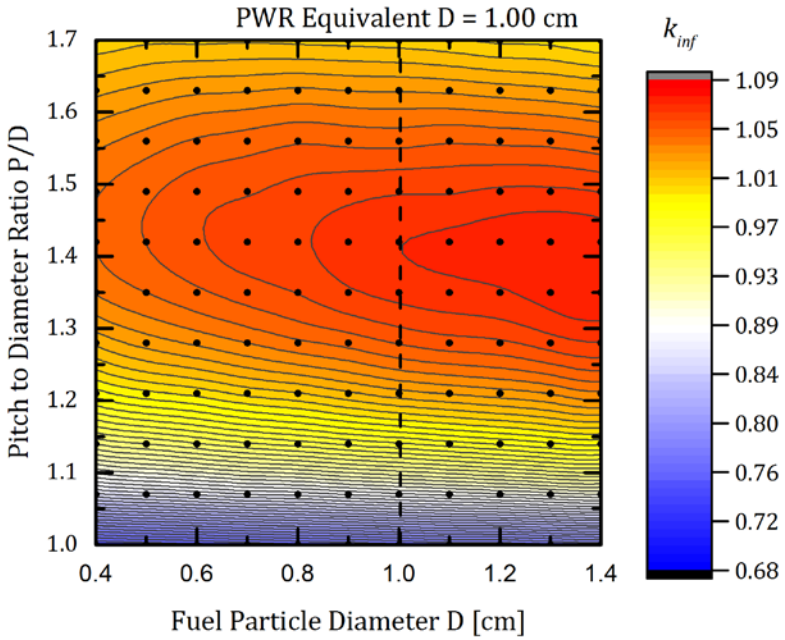

Figure A-21: K_{inf} contour plot for PWR UO2 spent fuel in infinite HCP lattice, after 10050 years decay. The spent fuel has burnup of 40 GWd/t and initial enrichment of 4.0%.

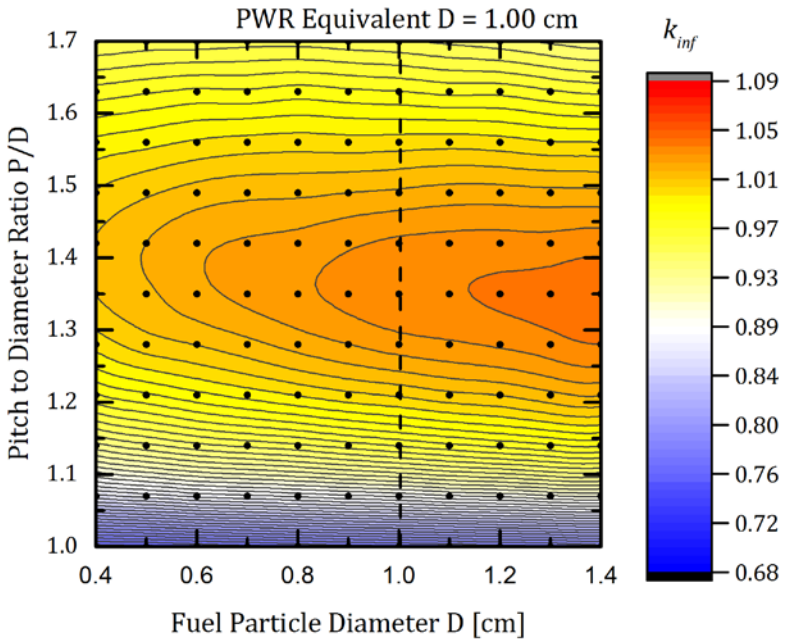

Figure A-22: K_{inf} contour plot for PWR UO_2 spent fuel in infinite HCP lattice, after 100050 years decay. The spent fuel has burnup of 40 GWd/t and initial enrichment of 4.0%.

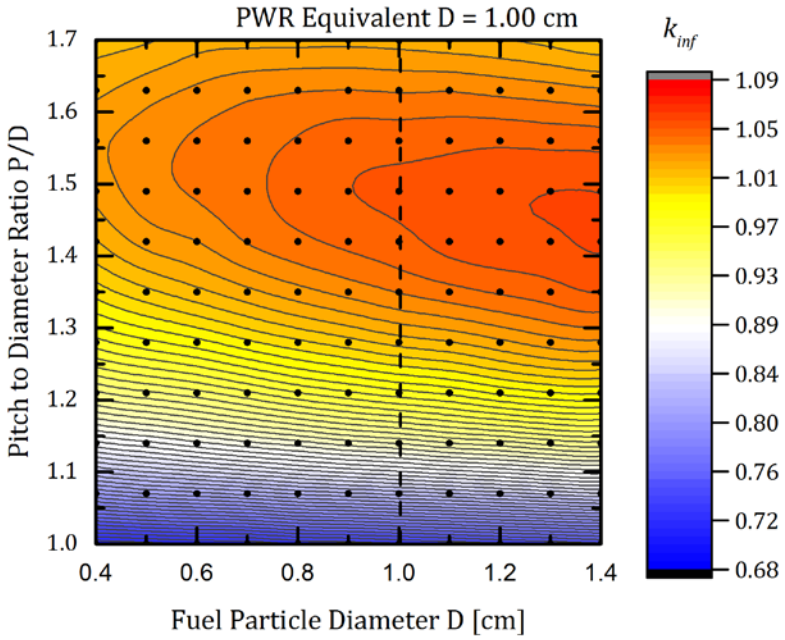

Figure A-23: K_{inf} contour plot for PWR UO_2 spent fuel in infinite HCP lattice, after 1050 years decay. The spent fuel has burnup of 40 GWd/t and initial enrichment of 4.0%.

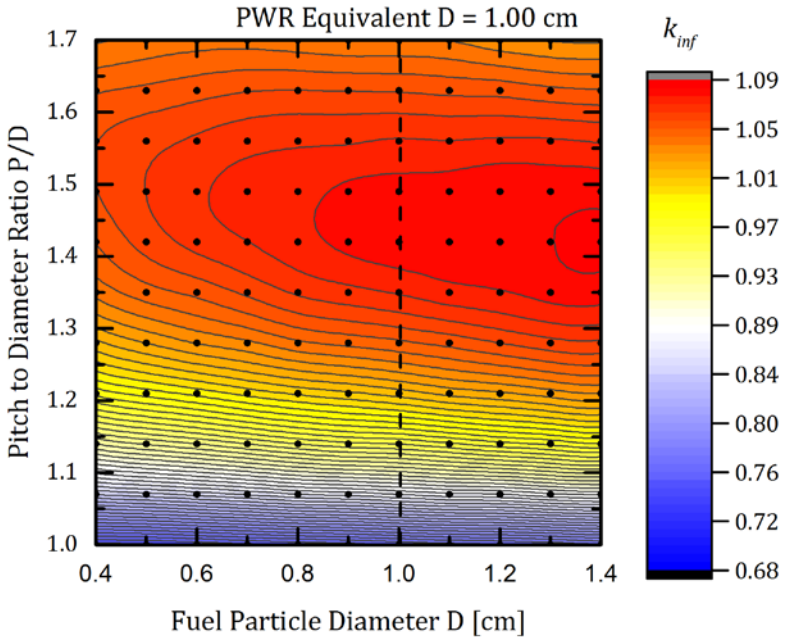

Figure A-24: K_{inf} contour plot for PWR UO_2 spent fuel in infinite HCP lattice, after 10050 years decay. The spent fuel has burnup of 60 GWd/t and initial enrichment of 6.0%.

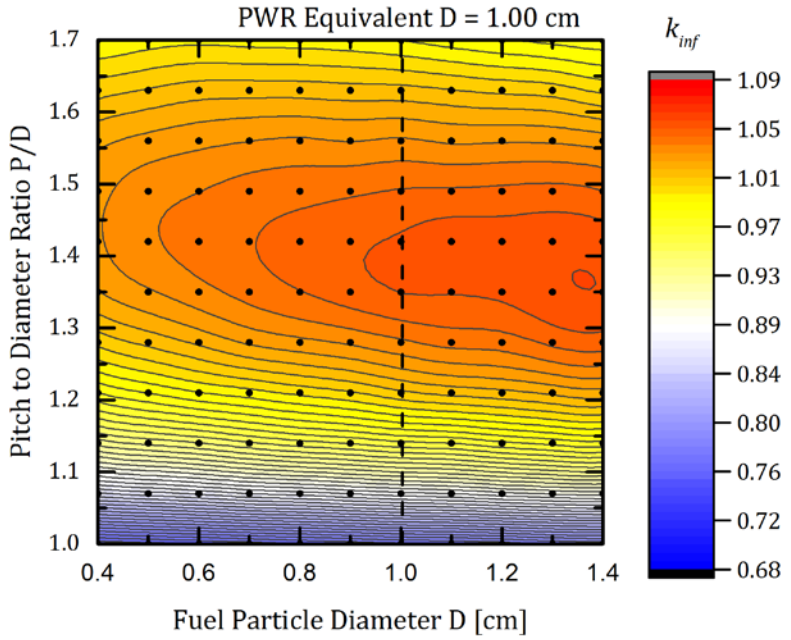

Figure A-25: K_{inf} contour plot for PWR UO_2 spent fuel in infinite HCP lattice, after 100050 years decay. The spent fuel has burnup of 60 GWd/t and initial enrichment of 6.0%.

A. 3 Numerical Results for Spent Fuels with Different Burnup and Initial Enrichments

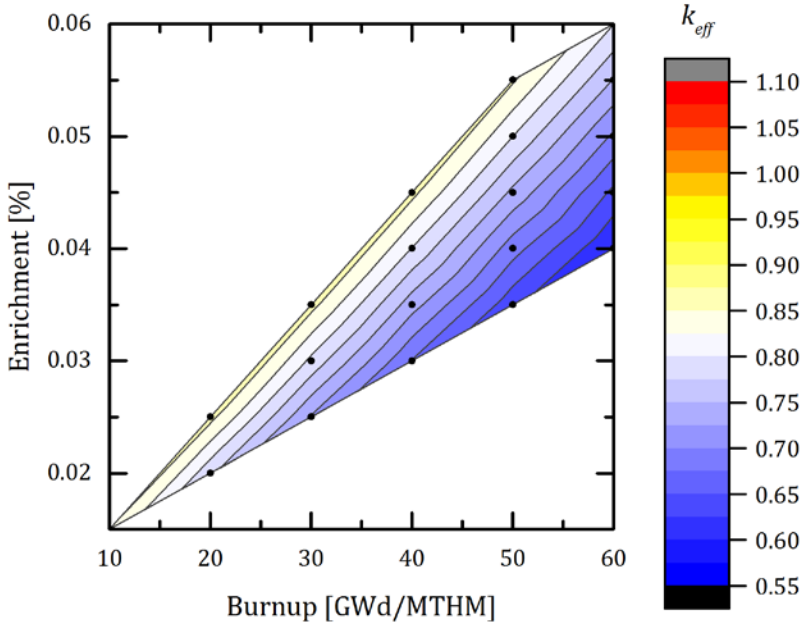

Figure A-26: K_{eff} contour for a spent fuel canister containing BWR UO2 spent fuel with different burnups and initial enrichments, after 1050 years decay.

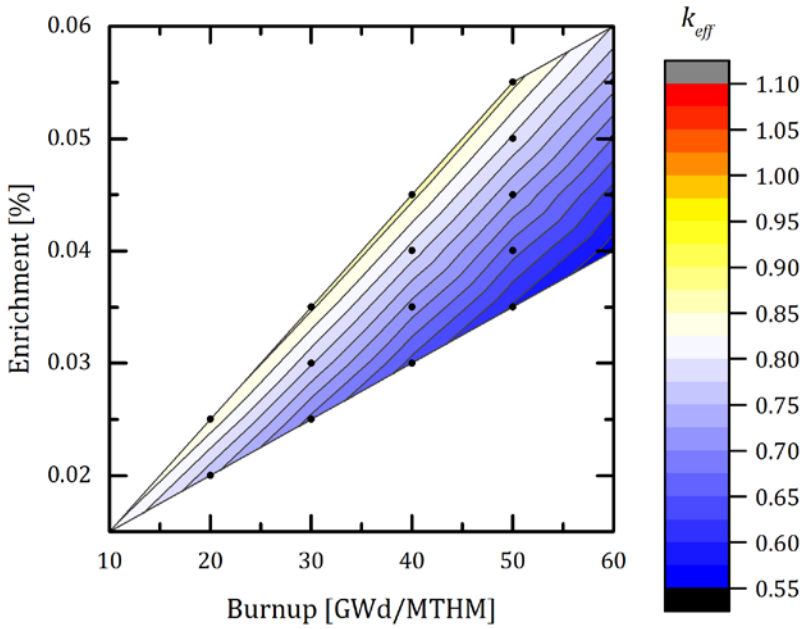

Figure A-27: K_{eff} contour for a spent fuel canister containing BWR UO2 spent fuel with different burnups and initial enrichments, after 100050 years decay.

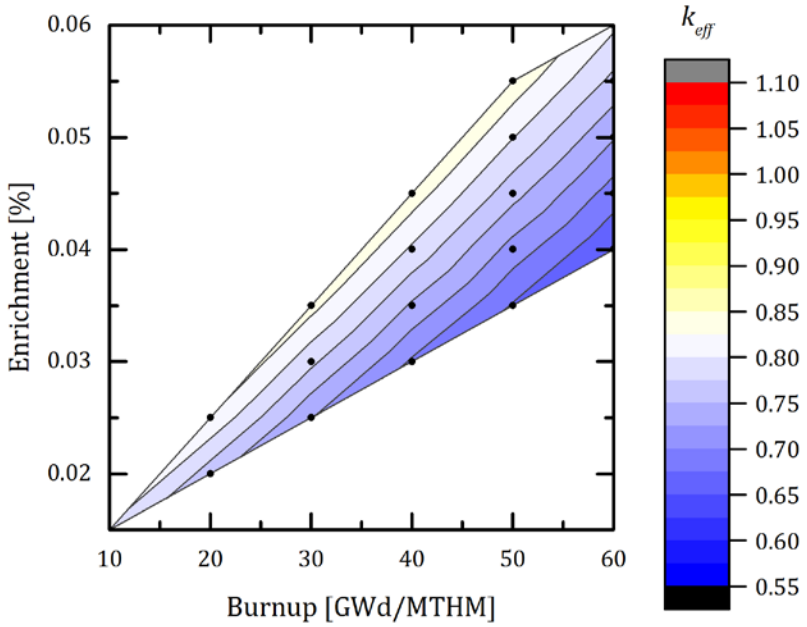

Figure A-28: K_{eff} contour for a spent fuel canister containing PWR UO2 spent fuel with different burnups and initial enrichments, after 1050 years decay.

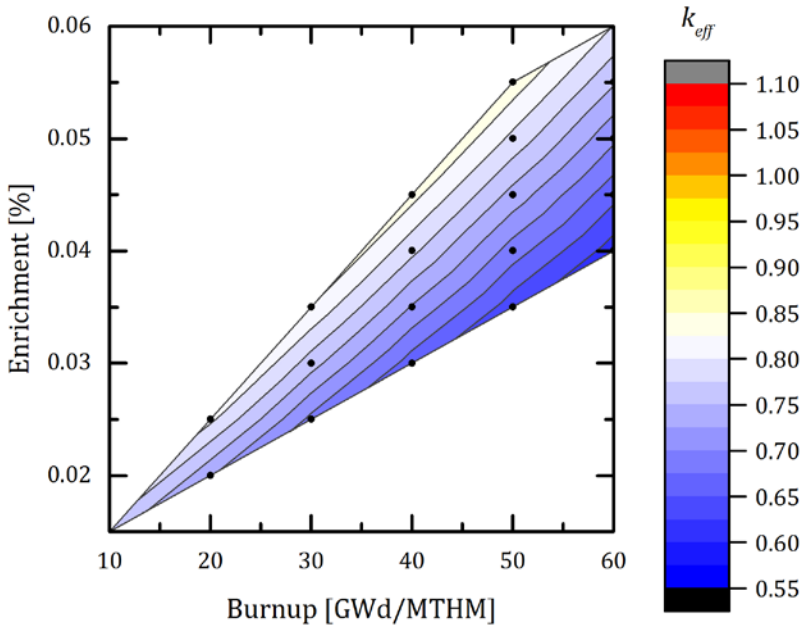

Figure A-29: K_{eff} contour for a spent fuel canister containing PWR UO2 spent fuel with different burnups and initial enrichments, after 100050 years decay.

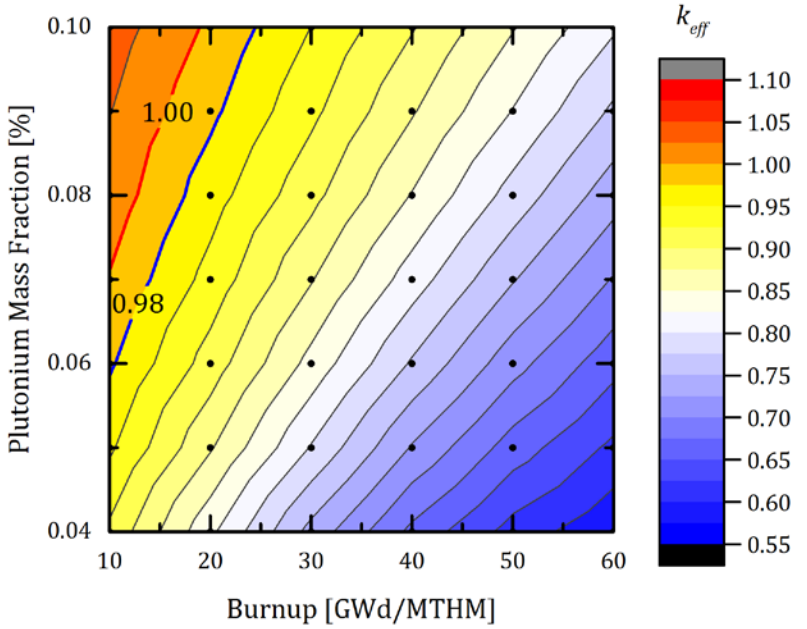

Figure A-30: K_{eff} contour for a spent fuel canister containing BWR MOX spent fuel with different burnups and plutonium mass fractions, after 1050 years decay.

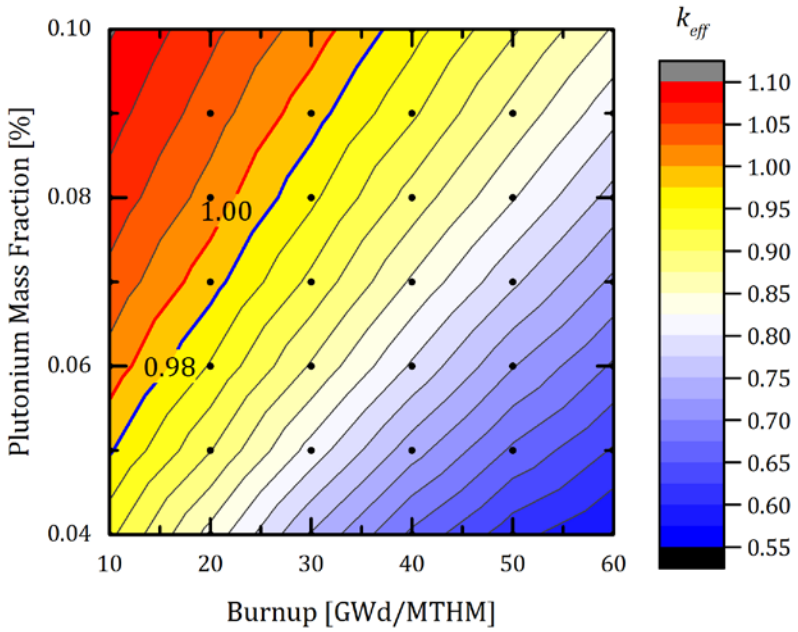

Figure A-31: K_{eff} contour for a spent fuel canister containing BWR MOX spent fuel with different burnups and plutonium mass fractions, after 100050 years decay.

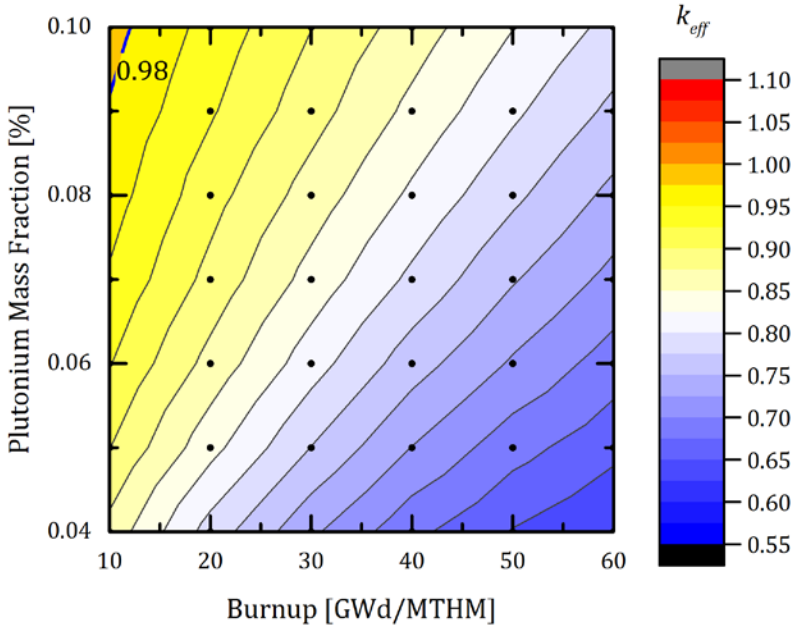

Figure A-32: K_{eff} contour for a spent fuel canister containing PWR MOX spent fuel with different burnups and plutonium mass fractions, after 1050 years decay.

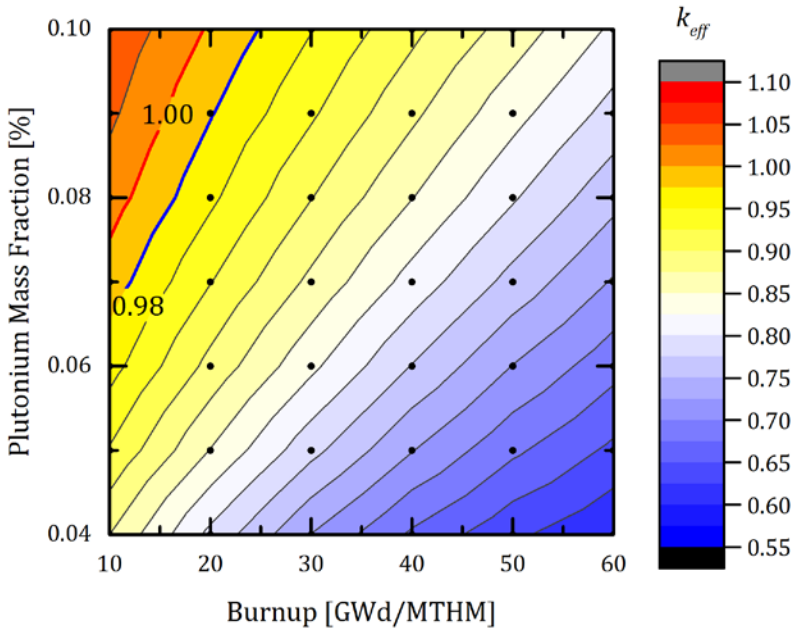

Figure A-33: K_{eff} contour for a spent fuel canister containing PWR MOX spent fuel with different burnups and plutonium mass fractions, after 100050 years decay.

Appendix B Derivation of the Feinberg-Galanin-Horning (F-G-H) Method

B. 1 Statement of the Problem and Governing Equations

Consider N different fuel lumps (say 1, 2 … N) at locations $\mathbf{r_1}$, $\mathbf{r_2}$ … $\mathbf{r_N}$ within space domain **V'**. The fuel lumps have uniform nuclide densities, but allows different geometries for different fuel lumps. The rest of **V'** is uniformly filled with moderator. And the entire domain **V'** is surrounded vacuum. The boundary condition of the problem can be given as zero flux at extrapolated distance into the reflector. The entire space domain including the extrapolated distance into the reflector is defined as **V**.

Neutron balance equation in one-group diffusion theory with neutron slowing-down can be written as,

$$-D_t\nabla^2\Phi_t(\boldsymbol{r})+\left(\Sigma_{at}+\Sigma_{af}(\boldsymbol{r})\right)\Phi_t(\boldsymbol{r})=\int_V d\boldsymbol{r}'\bar{\nu}\Sigma_f(\boldsymbol{r}')\Phi_t(\boldsymbol{r}')W(\boldsymbol{r}|\boldsymbol{r}')\quad,\tag{B-1}$$

with boundary condition $\Phi_t(\boldsymbol{r}_s)=0$, (B-2)

where $\boldsymbol{r}_s$ is on the surface of $\boldsymbol{V}$.

Terms in equation (B-1) are defined as followings:

$\Phi_t(\boldsymbol{r})$: Thermal flux

D_t: Diffusion coefficient for thermal neutron

Σ_{at}: Macroscopic absorption cross-section of the moderator

$\Sigma_{af}(\boldsymbol{r})$: Macroscopic absorption cross-section of the fuel (equals to zero if outside the fuel lumps)

$\bar{\nu}$: Averaged number of (fast) neutrons generated per fission

$\Sigma_f(\boldsymbol{r})$: Macroscopic fission cross-section of the fuel (equals to zero if outside the fuel lumps)

$W(\boldsymbol{r}|\boldsymbol{r}')$: Slowing down kernel, or the probability that a fast neutron generated at $d\boldsymbol{r}$ around $\boldsymbol{r}'$ slows down and become a thermal neutron in the volume $d\boldsymbol{r}$ around $\boldsymbol{r}$.

By defining thermal reproduction factor $\eta=\bar{\nu}\Sigma_f/\Sigma_{af}$ equation (B-1) can be further written as,

$$-D_t\nabla^2\Phi_t(\boldsymbol{r})+\left(\Sigma_{at}+\Sigma_{af}(\boldsymbol{r})\right)\Phi_t(\boldsymbol{r})=\int_V d\boldsymbol{r}'\eta\Sigma_{af}(\boldsymbol{r}')\Phi_t(\boldsymbol{r}')W(\boldsymbol{r}|\boldsymbol{r}')\ .\tag{B-3}$$

The general idea and key assumption in the F-G-H method is that, the thermal neutron flux in the vicinity of the fuel lumps have spherical (for 3D problems) or axial symmetry (for 2D problems), so that the individual fuel lumps can be treated as point or line sources and sinks. In F-G-H method, we define thermal constant γ for fuel lumps:

$$\gamma \equiv \frac{\text{total net current of thermal neutron into the lump}}{\text{thermal flux at the surface of the lump}} \,. \tag{B-4}$$

The physical meaning of γ is the number of neutron absorbed by the fuel lump per unit time per unit thermal flux at the surface of the fuel lump, which has the unit of surface area [cm^2]. Therefore equation (B-3) can be written as,

$$D_t \nabla^2 \Phi_t(\boldsymbol{r}) - \Sigma_{at} \Phi_t(\boldsymbol{r}) - \sum_{k=1}^{N} \gamma_k \delta(\boldsymbol{r} - \boldsymbol{r_k}) \Phi_t(\boldsymbol{r_k}) + \sum_{k=1}^{N} \eta_k \gamma_k \Phi_t(\boldsymbol{r_k}) W(\boldsymbol{r}|\boldsymbol{r_k}) = 0 \,. \tag{B-5}$$

Equation (B-5) can be solved by Green's function method. Consider Green's function for thermal flux $G_t(\boldsymbol{r}|\boldsymbol{r}_0)$,

$$D_t \nabla^2 G_t(\boldsymbol{r}|\boldsymbol{r}_0) - \Sigma_{at} G_t(\boldsymbol{r}|\boldsymbol{r}_0) + \delta(\boldsymbol{r} - \boldsymbol{r}_0) = 0 \,, \tag{B-6}$$

with boundary condition

$$G_t(\boldsymbol{r_s}|\boldsymbol{r}_0) = 0, \boldsymbol{r}_0 \in \boldsymbol{V} \,. \tag{B-7}$$

The solution of equation (B-5) can be written as,

$$\Phi_t(\boldsymbol{r}) = \int_V d\boldsymbol{r}_0 G_t(\boldsymbol{r}|\boldsymbol{r}_0) \left[\sum_{k=1}^{N} \eta_k \gamma_k \Phi_t(\boldsymbol{r_k}) W(\boldsymbol{r}_0|\boldsymbol{r_k}) - \sum_{k=1}^{N} \gamma_k \delta(\boldsymbol{r}_0 - \boldsymbol{r_k}) \Phi_t(\boldsymbol{r_k}) \right], \tag{B-8}$$

or

$$\Phi_t(\boldsymbol{r}) = \sum_{k=1}^{N} \gamma_k \Phi_t(\boldsymbol{r_k}) H(\boldsymbol{r}|\boldsymbol{r_k}) \,, \tag{B-9}$$

with

$$H(\boldsymbol{r}|\boldsymbol{r_k}) \equiv \int_V d\boldsymbol{r}_0 G_t(\boldsymbol{r}|\boldsymbol{r}_0) \left[\eta_k W(\boldsymbol{r}_0|\boldsymbol{r_k}) - \delta(\boldsymbol{r}_0 - \boldsymbol{r_k}) \right]. \tag{B-10}$$

Let $\boldsymbol{r} = \boldsymbol{r_i}$ in equation (B-8) and define $\Phi_t(\boldsymbol{r} = \boldsymbol{r_i}) \equiv \Phi_i$ *and* $H(\boldsymbol{r_i}|\boldsymbol{r_j}) = H_{ij}$, equation (B-8) can be written as,

$$\Phi_i = \sum_{j=1}^{N} \gamma_j \Phi_j H_{ij} \,. \tag{B-11}$$

Equation (B-11) is a set of linear equations; its determinant can be used to calculate the k_{eff}. The slowing-down kernel can be obtained by comparing the governing equations for one-group with slowing-down method and two-group method.

For one-group with slowing-down method, the governing equation is equation(B-5):

$$D_t \nabla^2 \Phi_t(\boldsymbol{r}) - \Sigma_{at} \Phi_t(\boldsymbol{r}) - \sum_{k=1}^{N} \gamma_k \delta(\boldsymbol{r} - \boldsymbol{r_k}) \Phi_t(\boldsymbol{r_k}) + \sum_{k=1}^{N} \eta_k \gamma_k \Phi_t(\boldsymbol{r_k}) W(\boldsymbol{r}|\boldsymbol{r_k}) = 0 \,.$$

For **two-group** method, the governing equations for thermal and fast neutrons are,

$$D_f \nabla^2 \Phi_f(\boldsymbol{r}) - \Sigma_r \Phi_f(\boldsymbol{r}) - \sum_{k=1}^{N} \eta_k \gamma_k \delta(\boldsymbol{r} - \boldsymbol{r_k}) \Phi_t(\boldsymbol{r_k}) = 0 \,, \tag{B-12}$$

$$D_t \nabla^2 \Phi_t(\boldsymbol{r}) - \Sigma_{at} \Phi_t(\boldsymbol{r}) + \Sigma_r \Phi_f(\boldsymbol{r}) = 0 \,, \tag{B-13}$$

where subscript f denotes the fast neutron and Σ_r is the removal cross-section from fast group to thermal group. We can define the Green's function for the fast flux $G_f(\boldsymbol{r}|\boldsymbol{r}_0)$,

$$D_f \nabla^2 G_f(\boldsymbol{r}|\boldsymbol{r}_0) - \Sigma_r G_f(\boldsymbol{r}|\boldsymbol{r}_0) + \delta(\boldsymbol{r}-\boldsymbol{r}_0) = 0, \tag{B-14}$$

with boundary condition

$$G_f(\boldsymbol{r}_s|\boldsymbol{r}_0) = 0, \boldsymbol{r}_0 \in \boldsymbol{V}. \tag{B-15}$$

The solution of equation (B-12) can be written as,

$$\Phi_f(\boldsymbol{r}) = \sum_{k=1}^{N} \eta_k \gamma_k G_f(\boldsymbol{r}|\boldsymbol{r}_k) \Phi_t(\boldsymbol{r}_k). \tag{B-16}$$

By substitutes the above $\Phi_f(\boldsymbol{r})$ in equation (B-13) and compare with equation(B-5), we have the slowing-down kernel given by two-group theory:

$$W(\boldsymbol{r}|\boldsymbol{r}') = \Sigma_r G_f(\boldsymbol{r}|\boldsymbol{r}'). \tag{B-17}$$

B. 2 Analytical Solutions

Define the problem domain $\boldsymbol{V} = \{-a \le x \le a; -b \le y \le b; -c \le z \le c\}$. First, we need to solve the Green's functions for thermal and fast neutrons. Because equation (B-6) and equation (B-14) have same mathematics form, only the full solution for equation(B-6) has been shown.

Define $\kappa_t = \sqrt{\frac{\Sigma_{at}}{D_t}}$, equation (B-6) can be written as

$$\nabla^2 G_t(\boldsymbol{r}|\boldsymbol{r}_0) - \kappa_t^2 G_t(\boldsymbol{r}|\boldsymbol{r}_0) + \frac{1}{D_t}\delta(\boldsymbol{r}-\boldsymbol{r}_0) = 0. \tag{B-18}$$

Consider a set of orthonormal Eigen functions, for Helmholtz equations with Eigenvalue B_n^2 that satisfy boundary condition(B-2):

$$\nabla^2 \psi_n(\boldsymbol{r}) + B_n^2 \psi_n(\boldsymbol{r}) = 0 \ . \tag{B-19}$$

If we write explicitly,

$$\psi_n(\boldsymbol{r}) = \psi_{pqr}(x,y,z) = \frac{1}{\sqrt{abc}} Cos(\alpha_p x) Cos(\beta_q y) Cos(\gamma_r z), \tag{B-20}$$

with Eigen value $B_n^2 = \alpha_p^2 + \beta_q^2 + \gamma_r^2$,

where,

$$\alpha_p = \frac{\left(\frac{1}{2}+p\right)\pi}{a}, \beta_q = \frac{\left(\frac{1}{2}+q\right)\pi}{b}, \gamma_r = \frac{\left(\frac{1}{2}+r\right)\pi}{c}, p = 0,1,2\ldots; q = 0,1,2\ldots; r = 0,1,2,\ldots$$

.

Let $G_t(\boldsymbol{r}|\boldsymbol{r}_0) = \sum_n \psi_n(\boldsymbol{r}) C_n(\boldsymbol{r}_0)$, equation (B-18) can be written as,

$$\sum_n \psi_n(\boldsymbol{r})(B_n^2+\kappa_t^2)C_n(\boldsymbol{r}_0)=\frac{1}{D_t}\delta(\boldsymbol{r}-\boldsymbol{r}_0). \tag{B-21}$$

Let equation (B-21) times $\psi_m(\boldsymbol{r})$ and integrates over **V**, by orthonormal property $\int_V d\boldsymbol{r}\psi_m(\boldsymbol{r})\psi_n(\boldsymbol{r})=\delta_{m,n}$.

Therefore,
$$C_n(\boldsymbol{r}_0)=\frac{1}{D_t}\frac{\psi_n(\boldsymbol{r}_0)}{B_n^2+\kappa_t^2}, \tag{B-22}$$

and
$$G_t(\boldsymbol{r}|\boldsymbol{r}_0)=\frac{1}{D_t}\sum_n\frac{\psi_n(\boldsymbol{r})\psi_n(\boldsymbol{r}_0)}{B_n^2+\kappa_t^2}. \tag{B-23}$$

Similarly, the Green's function for fast flux can be solved as,
$$G_f(\boldsymbol{r}|\boldsymbol{r}_0)=\frac{1}{D_f}\sum_n\frac{\psi_n(\boldsymbol{r})\psi_n(\boldsymbol{r}_0)}{B_n^2+\kappa_f^2}, \tag{B-24}$$

where $\kappa_f=\sqrt{\frac{\Sigma_r}{D_f}}$.

By equation(B-17), we have
$$W(\boldsymbol{r}|\boldsymbol{r}')=\kappa_f^2\sum_n\frac{\psi_n(\boldsymbol{r})\psi_n(\boldsymbol{r}')}{B_n^2+\kappa_f^2}. \tag{B-25}$$

Substitute terms in equation (B-10) by equations (B-23) and(B-25),

$$\begin{aligned}H(\boldsymbol{r}|\boldsymbol{r}_k)&\equiv\int_V d\boldsymbol{r}_0 G_t(\boldsymbol{r}|\boldsymbol{r}_0)\left[\sum_{k=1}^N\eta_k W(\boldsymbol{r}_0|\boldsymbol{r}_k)-\delta(\boldsymbol{r}_0-\boldsymbol{r}_k)\right]\\&=\int_V d\boldsymbol{r}_0\frac{1}{D_t}\sum_n\frac{\psi_n(\boldsymbol{r})\psi_n(\boldsymbol{r}_0)}{B_n^2+\kappa_t^2}\left[\eta_k\kappa_f^2\sum_m\left(\frac{\psi_m(\boldsymbol{r}_0)\psi_m(\boldsymbol{r}_k)}{B_m^2+\kappa_f^2}\right)-\delta(\boldsymbol{r}_0-\boldsymbol{r}_k)\right]. \qquad \text{(B-26)}\\&=\frac{\eta_k\kappa_f^2}{D_t}\sum_n\left(\frac{\psi_n(\boldsymbol{r})\psi_n(\boldsymbol{r}_k)}{(B_n^2+\kappa_t^2)(B_n^2+\kappa_f^2)}\right)-\frac{1}{D_t}\sum_n\frac{\psi_n(\boldsymbol{r})\psi_n(\boldsymbol{r}_k)}{B_n^2+\kappa_t^2}\end{aligned}$$

Consider the Eigenvalue problem, equation(B-5) can be written as,

$$\begin{aligned}&D_t\nabla^2\Phi_t(\boldsymbol{r})-\Sigma_{at}\Phi_t(\boldsymbol{r})-\sum_{k=1}^N\gamma_k\delta(\boldsymbol{r}-\boldsymbol{r}_k)\Phi_t(\boldsymbol{r}_k)\\&+\sum_{k=1}^N\frac{1}{k_{eff}}\eta_k\gamma_k\Phi_t(\boldsymbol{r}_k)W(\boldsymbol{r}|\boldsymbol{r}_k)=0\end{aligned}. \tag{B-27}$$

And equation (B-26) can be written as,

$$H\left(\boldsymbol{r}|\boldsymbol{r_k}\right)=\frac{\eta_k\kappa_f^2}{D_t}\frac{1}{k_{eff}}\sum_n\left(\frac{\psi_n\left(\boldsymbol{r}\right)\psi_n\left(\boldsymbol{r_k}\right)}{\left(B_n^2+\kappa_t^2\right)(B_n^2+\kappa_f^2)}\right)-\frac{1}{D_t}\sum_n\frac{\psi_n\left(\boldsymbol{r}\right)\psi_n\left(\boldsymbol{r_k}\right)}{B_n^2+\kappa_t^2}. \qquad \text{(B-28)}$$

Let $A_{ij}=\gamma_j\frac{\eta_k\kappa_f^2}{D_t}\sum_n\left(\frac{\psi_n\left(\boldsymbol{r_i}\right)\psi_n\left(\boldsymbol{r_j}\right)}{\left(B_n^2+\kappa_t^2\right)(B_n^2+\kappa_f^2)}\right)$; $B_{ij}=\gamma_j\frac{1}{D_t}\sum_n\frac{\psi_n(\boldsymbol{r_i})\psi_n\left(\boldsymbol{r_j}\right)}{B_n^2+\kappa_t^2}$ equation (B-11) become,

$$\Phi_i=\frac{1}{k_{eff}}\sum_{j=1}^{N}A_{ij}\Phi_j-\sum_{j=1}^{N}B_{ij}\Phi_j, \qquad \text{(B-29)}$$

or

$$\left(I+B\right)\Phi=\frac{1}{k_{eff}}A\Phi. \qquad \text{(B-30)}$$

Equation (B-30) is the standard form of the criticality eigenvalue problem, where $\left(I+B\right)$ is the destruction operator and A is the production operator. By definition, k_{eff} is the largest of equation(B-30).